LBL--28625

DE91 001790

Electron Crystallography of PhoE Porin, an Outer Membrane, Channel-Forming Protein from *E. Coli*

Peter J. Walian

Ph.D. Dissertation

November, 1989

Department of Biophysics
University of California

and

Cell and Molecular Biology Division
Lawrence Berkeley Laboratory
1 Cyclotron Road
Berkeley, CA 94720

This work was supported by the Office of Health and Environmental Research, U.S. Department of Energy under contract no. DE-AC03-76SF00098 and by National Institutes of Health Program Project Grant GM36884.

TABLE OF CONTENTS

SECTION I

SECTION II

SECTION III

SECTION IV

Acknowledgements

This dissertation is dedicated to my wife, Josette, for her patience, her understanding and her great sense of humor.

I am extremely grateful to Professor Robert Glaeser for introducing me to the field of electron crystallography and fostering my interest in the study of membrane proteins, and to Dr. Bing Jap for his generosity in allowing me to participate in his exciting research efforts. I also wish to thank Professors Glaeser, Hiroshi Nikaido and Harold Lecar for their critical reading of this manuscript and for the many hours of stimulating discussion.

Special thanks are due to Drs. Richard Henderson and Tom Ceska for their invaluable technical advice and suite of software without which this thesis would not have been possible. Dr. Kenneth Downing's and Rick Burkard's expertise and assistance in a broad range of subjects combined to make my experiences on the microscope and numerous computers successful ones.

Finally, I would like to thank my mother and father for all they have done and to give thanks to God for creating the fascinating world in which we live and for providing the opportunities to probe its wonders.

Introduction

At present the photosynthetic reaction centers of Rhodobacter viridis and sphaeroides are the only membrane proteins for which the structures have been determined to atomic resolution (Deisenhofer et.al. 1984; Deisenhofer et. al. 1985; Allen et. al. 1987 ; Allen et. al. 1987). The atomic structure of the Rhodobacter sphaeroides reaction center was determined with the aid of the phase information derived from the solution of the viridis structure. Solving the viridis structure, for which the Nobel prize in chemistry for 1988 was awarded, was accomplished with the use of X-ray crystallographic techniques on three-dimensional crystals composed of protein-detergent complexes. Other membrane proteins, such as OmpF porin and bacteriorhodopsin (bR), have been crystallized for X-ray study. Unfortunately, progress on determining the atomic structures of these proteins has suffered due to a lack of high resolution order in crystals of the native proteins (eg bR) or due to difficulties in obtaining well ordered crystals of protein heavy atom derivatives (eg OmpF porin) (R.M. Garavito; B.K. Jap personal communication).

As the "hard" knowledge base of the atomic structure of membrane proteins currently exits, it is solely comprised of the results of the X-ray studies on Rhodobacter photosynthetic reaction centers. The range of membrane protein function is vast, and includes roles in energy transduction; passive, facilitated and active transport; and transmembrane signalling. The structural schemes for organizing peptides into functional membrane "machines" will undoubtedly be as wide ranging. Presently, "rules" or algorithms for predicting whether peptides will assume a certain local conformation, helical versus beta-sheet for example, in an environment of some assumed polarity are overwhelmingly based on studies of soluble proteins. Obviously, if the ability to predict or assess the structure and function of membrane proteins is to improve, structural data from many membrane proteins will be needed.

Electron crystallography, an alternative

Another approach to studying the structure of membrane proteins is the use of electron crystallography. Due to the strength of the scattering interaction between the specimen and the electron beam, electron crystallography is ideally suited for the observation of monolayer crystals. Monolayer (one unit cell thick) crystals as small as 1-10 micrometers in diameter have provided high resolution structural information for a number of membrane proteins (Henderson et. al. 1986; Henderson et. al. 1988 ; Kuhlbrandt and Downing 1989; Jap B.K. 1989). Protocols to form crystals of this type typically require protein quantities of the order of 1 milligram, whereas protocols designed to generate three-dimensional crystals suitable for X-ray studies may require a thousand fold more protein. Thus, electron crystallography could be a distinct advantage when working with low-yield membrane protein systems. Besides allowing one to work with smaller quantities of protein, lipid bilayers offer an ideal chemical and physical environment for studying membrane proteins. An additional advantage of the use of electron crystallography for membrane protein structure determination is that the creation of heavy atom derivatives is not required to determine structure factor phases; phase information is obtained directly from electron micrograph images.

Why study PhoE porin?

Dr. Bing Jap has crystallized PhoE pore-forming protein (porin) from the outer membrane of Escherichia coli (E. coli) into monolayer crystals. The findings of this thesis research and those of Jap (1988,1989) have determined these crystals to be highly ordered, yielding structural information to a resolution of better than 2.8 angstroms. PhoE porin shares strong homologies with the major outer membrane porins of E. coli and Salmonella typhimurium (S. typhimurium), OmpF and OmpC. These similarities include not only general low resolution stuctural features and function, but a high degree of correlation (better than 60 percent) in amino acid sequence. The porins as a class of proteins have been studied intensively and a wealth of information addressing their biochemical and electrophysiological properties exists. Spectroscopic studies have found these proteins to be rich in beta-sheet structure. Indications are that PhoE porins as well as the general family of porins make for an ideal experimental system with which to study the structure and functional properties of "simple" transmembrane channels.

All of these notions reinforce our opinion that the time is right for attempting to determine the high resolution three-dimensional structure of PhoE porin. My task in this thesis has been to collect and process the electron diffraction patterns necessary to generate a complete three-dimensional set of high resolution structure factor amplitudes of PhoE porin. Fourier processing of these amplitudes when combined with the corresponding phase data is expected to yield the three-dimensional stucture of PhoE porin at better than 3.5 angstroms resolution.

Section I

BACKGROUND

1.1 The outer-membranes of gram-negative bacteria

The outer membranes of gram-negative bacteria serve as the "front line" of traffic management for solutes entering and leaving the host cell. They are protein-impregnated lipid bilayers in which the component lipids are partitioned in an asymmetric manner. In wild type organisms, the lipid component of this membrane's outer (extracellular) leaflet is exclusively lipopolysacchride while the inner (periplasmic) leaflet of this bilayer is composed of more conventional lipids such as phosphatidylethanolamine and phosphatidylglycerol, commonly found in plasma membranes. The head groups of these lipopolysacchrides have a strong affinity for divalent cations like Ca++ for example, and given sufficient concentrations of these ions, the outer-membrane can form quite a formidable permeability barrier via this head group/salt bridge network (Nikaido and Vaara 1985). It is the addition of pore-forming proteins (porins), that gives the outer-membrane its useful permeability, albeit in a regulated fashion. The porins, of which PhoE porin is but one, represent a significant fraction of the total outer-membrane protein. Two other proteins, murein lipoprotein and Omp A (in the specific examples of E. coli and S. typhimurium) comprise the remainder of the major outer-membrane proteins. A general architecture of the outer membrane shared among the spectrum of gram-negative bacteria is depicted in figure 1.

OmpA is believed to exist in monomeric form in the outer-membrane, and it has a molecular weight of approximately 35 kD. Although it does not seem to self-aggregate in significant numbers in the membrane (Ueki et. al. 1970), it is frequently isolated as a complex with murein lipoprotein (Palva 1979). OmpA appears to have a significant portion of its mass located in the periplasm (Chen et. al. 1980). From permeability and transport studies of wild type and mutant OmpA producing bacteria, OmpA appears to be of importance in maintaining normal rates of transport through the outer-membrane but not as a specific channel-former itself (Manning et. al. 1977 ; Nikaido et. al. 1977). The most probable function of this protein appears to be in ensuring the structural stability of the outer membrane (Manning and Achtman 1979). Spectroscopic studies indicate that these proteins have a high beta-sheet content (Nakamura and Mizushima 1976).

Figure 1. Structural overview of the outer membrane and associated structures. The lipid bilayer of the outer membrane is of asymmetric design. The outer leaflet of the bilayer is composed exclusively of lipopolysaccharide while the inner leaflet is composed of phospholipids. The outer membrane is studded with many proteins of which the porins comprise the major fraction. OmpA and murein lipoprotein are there in lower numbers and help to "anchor" the outer membrane to the peptidoglycan.

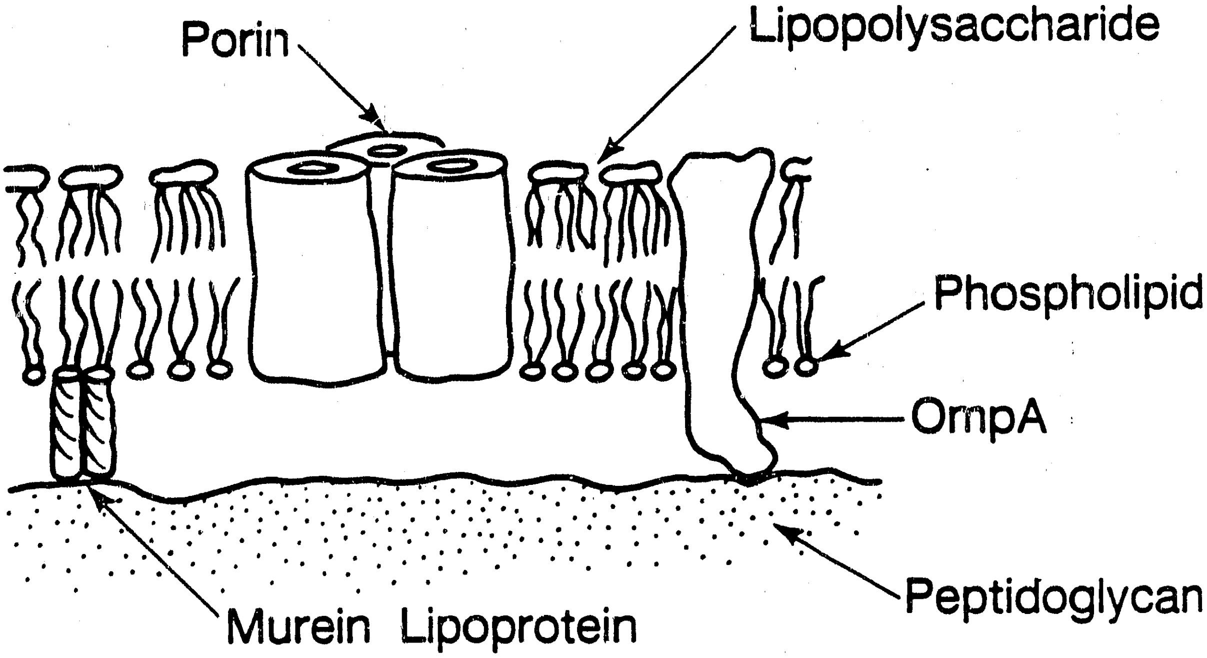
Porin
Lipopolysaccharide
Phospholipid
OmpA
Peptidoglycan
Murein Lipoprotein

XBL 897-5129

Another important constituent of the outer membrane is murein lipoprotein. This lipoprotein has an apparant molecular weight of about 7 kD. Its structure appears to be that of an alpha-helical protein covalently attached to fatty acid chains, allowing this hydrophobic tail to partition into the inner leaflet of the bilayer while exposing the protein domain to the periplasm (Braun et. al. 1976). Although most of the lipoprotein isolated from the outer-membrane is available in a "free" state, a sizable amount (about one-third) is found to be covalently bound to the peptidoglycan of the periplasm (Inouye et. al. 1972). Again, as in the case of OmpA, these proteins appear to have a role in maintaining the structural stability of the outer membrane.

An outer membrane's permeability can be adjusted to accomodate changes in enviromental conditions by altering the number and type of its porin population. Instead of relying on one specific pore type, the outer membrane is host to a spectrum of porins, with each type adding its own permeability/selectivity characteristics to the membrane's net permeabilty profile. The porins achieve this variety of permeability through a combination of pore size, distribution of charged and polar amino acids, and in some cases substrate specific binding sites. When a challenge such as phosphate starvation is presented to bacteria such as E. coli and Pseudomonas aeruginosa (P. aeruginosa), both respond by elevating their outer-membrane population of an anion preferential porin. Even though identical environmental challenges were applied to the bacteria, the two respond with different "solutions". E. coli would elevate the percentage of its general purpose anion selective porin, PhoE. PhoE porin has as its basic functional unit a trimer of pores or channels (Jap 1989). P. aeruginosa would increase its outer-membrane population of protein P. This is a phosphate specific porin with monomers as their basic functional unit (Hancock and Benz 1986) . Although there are no specific rules on how a porin must be designed to meet the particular needs of a host bacterium, common design themes have been found. These will be reviewed in the following subsections, with specific emphasis on the porins of E. coli.

1.2 Porins of Escherichia coli

The porins of gram-negative bacteria can be catagorized as being cation selective, anion selective and/or solute specific. In addition to providing transport routes through the outer membrane, the porins also serve as phage receptor sites (Datta et. al. 1977). Although a great variety of porins exist among gram-negative bacteria, many share common physical properties and structural characteristics. It is these generalized properties that make these porins ideal model systems for studying and characterizing ion transport through channels. For my thesis research I have chosen to study PhoE porin, an anion selective porin isolated from the outer membrane of Escherichia coli. Before discussing further details specific to PhoE, I would like to survey the porins of primary influence in Escherichia coli.

The major porins of Escherichia coli are considered to be OmpC and OmpF. The letters "omp" in their designated names is an abbreviation for "outer membrane protein". Both of these porins are general purpose cation selective but not to the point of excluding anions. Anions can diffuse through these pores at significantly reduced rates as compared to cations. No specific solute selectivity has been found in these porins. Although both OmpF and OmpC are found in the outer membrane of wild type strains under normal conditions, OmpF is found in higher quantities than OmpC. Under conditions of osmotic stress this relationship is reversed with OmpC being expressed in higher numbers (Nikaido and Vaara 1985). PhoE porin, an anion selective porin, is under normal conditions expressed in low numbers. Under conditions of phosphate starvation, hence the source of the "pho" part of its name, its expression into the outer membrane is greatly increased, elevating phosphate uptake. This porin, while preferential to anions, is also non-exclusive for anion diffusion and will accommodate the transport of cations, although not as efficiently as OmpF and OmpC. Also present in reasonably large concentrations is LamB porin, the "lam" segment of its name referring to its ability to act as a receptor for lambda phage. This porin is an example of a substrate specific channel. In the case of LamB porin the specific substrate is maltose (Hazelbauer 1975; Szmelcman and Hofnung 1975; Luckey and Nikaido 1980).

1.3 Physical and Chemical Properties

1.3.1 Pore Exclusion Limits and Rates of Permeability

Various techniques have been applied in the characterization of the transport properties of E. coli porins. Some of the first experiments utilized porins reconstituted into liposomes to study the diffusion of solutes through the pores. One criterion useful in comparing the functional charcteristics of different porins is the exclusion limit of the porin channels. Experiments conducted with porin-impregnated liposomes can test for the ability of a solute to pass through the vesicle bilayers. These tests were perfomed using radiolabeled solutes, surveying a range of molecular weights, encapsulated in the vesicles during the process of liposome formation. In addition to the solutes being evaluated, trapped inside the vesicles were also larger porin-impermeable substances labeled with a different radioisotope. These vesicles were then transferred to a sizing column. The column migration of solutes able to pass through the porin pores would be much slower than that of the liposomes themselves, allowing for a comparative analysis of the radioisotope ratio contained in the liposomes after elution. For the major E. coli and S. typhimurium porins OmpF and OmpC, the upper molecular weight of solutes able to pass through the pores fell into a range of 500 to 700 daltons.(Nakae 1976a;

Decad and Nikaido 1976; Nakae 1976b). Porin pore limiting diameters were then estimated from the calculated Stokes radii of solutes falling in the range of a porin's exclusion limit. Based on experiments with the porins of Escherichia coli and Salmonella typhimurium , maximum pore diameters in the range of 11 to 12 angstroms have been predicted.

Although the liposome efflux/diffusion assays described above were useful in determining the molecular weight upper limits of solutes able to diffuse through porin pores, they did not have the ability to resolve time dependent characteristics of the pores, such as the solute dependent permeabilty rates. To study these parameters liposome swelling assays were performed. (Luckey and Nikaido 1980; Nikaido and Rosenberg 1981; Nikaido and Rosenberg 1983) In these experiments porin impregnated liposomes are reconstituted so as to entrap large impermeable molecules such as dextran. These vesicles are then transferred to an isotonic solution of the solute whose porin permeability is to be assayed. Solutes able to diffuse through the pores of the porins incorporated into the liposome bilayers increase the total solute concentation inside the liposomes. An osmotic gradient is established which in turn promotes the influx of water causing the liposomes to swell. This swelling can be monitored by measurement of the liposome containing solution's ability to scatter light. Relative solute permeability rates are then derived directly from the liposome swelling rate data of the specific solutes assayed. Due to experimental difficulties in separating the effects of the coupled movements of different buffer ions from those of charged test solutes, the liposome swelling assay is most reliably applied in permeability studies of uncharged solutes (Nikaido and Vaara 1985). For solute-nonspecific porins it has been shown that the values for the logarithm of the relative solute permeabilities decrease linearly with an increase in solute molecular weight (Nikaido and Rosenberg 1981). Estimates of pore size based on these measurements of relative permeability were calculated using equations describing a physical model developed by Renkin (1954). Pore diameters of 10.8 and 10.6 angstroms for E. coli OmpC and PhoE respectively, 11.6 angstroms for E. coli OmpF (Nikaido and Rosenberg 1983) and 20 angstroms for protein F of P. aeruginosa (Yoshimura et. al. 1983) have been proposed based on this general approach. For a comparison of pore sizes based on this and other experimental techniques see Table 1 in section 1.3.2.1.

Experiments on porin pore permeability have also been made on intact bacteria. The method employed here has been to monitor the rate of hydrolysis of solutes in the medium into which the bacteria have been placed. Beta-lactam antibiotics have been solutes evaluated with this experimental protocol. Hydrolysis of these antibiotics experimental protocol. Hydrolysis of these antibiotics takes place in the periplasm where the beta-lactam enzymes exist. Outer membrane permeation and enzymatic breakdown of the solute in question can be modeled as two independent processes, uptake governed by simple diffusion as decribed by Fick's first law and substrate hydrolysis by Michaelis-Menten kinetics (Zimmerman and Rosselet 1977 ; Sawai et. al. 1977). Laboratory measured solute hydrolysis rates can therefore be decomposed into separate rate contributions from each step, yielding an estimate of porin pore permeability. The finding that porin deficient mutants suffer up to a 100-fold reduction in beta-lactam permeation emphasizes the existence of an in vivo role for porin in outer membrane permeability.

1.3.2 Porin Channel Conductance and Gating

Another approach to studying permeability properties of porin is the use of black lipid bilayer systems. These experiments use a vessel, made of a hydrophobic material such as teflon or polycarbonate plastic, which is partitioned into two chambers by a barrier or membrane which is also hydrophobic in nature. This barrier has a small centrally located hole usually a few hundred micrometers in diameter. It is across this small hole that lipid bilayers are established and the proteins of interest, in this case porins, inserted. Buffer medium fills each chamber bathing the bilayer from both sides providing a conductance path between electrodes placed in each chamber. Through the use of these electrodes, potential differences can be applied across the lipid bilayer and conductance measured. Several methods for generating porin containing black lipid membranes have been described (Benz et. al. 1978; Young et. al. 1983 ; Cohen et. al. 1982 ; Schindler and Rosenbusch 1978; Schindler and Rosenbusch 1981).

In the many BLM experiments performed on porins one of the key issues examined was whether porin channels are voltage gated. The results of these investigations are varied with not all researchers reporting evidence of channel gating. Investigators who reported no evidence of porin channel voltage dependent gating indicated that their experimental data effectively contained only conductance increases reflecting porin insertions into the bilayers. Decreases in conductance, although observed were cited as a rare occurence and as such dismissed as the result of porin inactivation in response to applied potentials approaching the breakdown limit of the membrane (Benz 1985 ; Hancock 1987). Other investigators have demonstrated that not only can conductance increases be regularly observed, but voltage dependent gating of the porin channels can be as well (Schindler and Rosenbusch 1978,1981; Mauro et. al. 1988; Dargent et. al. 1986; Xu et. al. 1986). In these experiments one can also find ample evidence to support the conclusion that conductance decreases are quantized in fractions of the porin single unit open state conductance. For example, an open state conductance of 1.7-2 nS per PhoE porin trimer has been reported (Benz et. al. 1985; Dargent et. al. 1986) while step-wise conductance decrements of about 0.6 nS were also reported by Dargent et. al. For PhoE this information therefore describes a porin trimer in which each monomer channel has a conductance of one-third the total conductance of the trimer in its fully "open" state.

The apparent inability of certain researchers to detect porin channel closings on a regular and reliable basis appears to be due to the experimental procedures employed.

Typical in the protocols of the many researchers who have reported observations of channel closures, detergent solubilized porin is added to one of the two BLM vesicle chambers after the formation of a BLM. After application of an initial membrane potential to accelerate incorporation of porin into the bilayer, the polarity of the applied potential is reversed and the unitary closing response recorded. Benz and collaborators report that they would add solubilized porin to their apparatus' chambers before or after formation of a BLM (Benz et. al. 1985). They would then apply a membrane potential and observe, almost exclusively, conductance increases regardless of the polarity of the membrane potential. Similar behavior has also been observed by researchers who have observed channel closings. This behavior could be observed when, if upon breakage of a BLM after the addition of porin, a new membrane was "painted" on and the experiment continued; if porin was added to the BLM chamber prior to establishment of a bilayer; if porin was originally added to the chambers on both sides of the membrane; if the vessel was not cleaned fastidiously between experiments or if a concentration of solubilized porin higher than what was needed to generate a minimum number of incorporation events was used (V. Vacata and H. Lecar, personal communication).

These observations appear to indicate that in a given experiment the bulk of detergent solubilzed porins added to one chamber of a test vessel are, under the influence of an applied "insertion" voltage, directionally inserted into the BLM bilayer. One explanation for this would be that detergent solubilized porins bear a consistent asymmetric distribution of charge causing them to respond as dipoles under the influence of an applied electric field. If one were to place such solubilized porin on both sides of a BLM bilayer then regardless of the polarity of the applied membrane potential one would detect conductance increases. Considering that insertion events occur very rapidly with respect to typical times reported for channel closings, it is very understandable that even for experimental recordings many minutes in duration it would be very difficult to detect channel closings on a background of rapid conductance increases.

It has been argued that the reported voltage-dependent gating of E. coli porins are simply porin inactivations due to protein breakdown. The recordings for the porins OmpF, OmpC and PhoE repeatedly show conductance decreases in steps of approximately one-third the peak (open trimer) conductance. It is highly doubtful that a random process such as protein denaturation would occur in such a consistent and orderly fashion. Another hallmark of voltage gating is the presence of reversibility in the process. Indications of reversibility in the closing of the porin channels is evident in many of the recordings of porin channel closings. In these recordings one can usually find states of the porin where the conductance is temporarily oscillating between conductance decrease steps strongly indicating reversibility in the gating process (Schindler and Rosenbusch 1978,1981; Dargent et. al. 1986; Mauro et. al. 1988) (see Figure 2).

Figure 2. Idealized representation of a typical unitary response for porins in a Black Lipid Membrane experiment. This cartoon captures the essential features seen in tracings of porin voltage dependent gating (Mauro et. al. 1988; Dargent et. al. 1986; Engel et. al. 1985). The unitary response begins with an initial rise in conductance due to the potential applied across the porin in its open state. Following this initial rise the conductance decreases in step-wise fashion in increments of one-third the peak (open state) conductance. The time intervals between conductance step decreases is typically on the order of hundreds of milliseconds and is not constant. Also frequently seen are transient or incomplete step decreases in the form of spike-like conductance decreases.

XBL 899-5212

1.3.2.1 Pore Size Determination From BLM Data

The importance of these differing observations and conclusions is evident not only in the evaluation of the existence of a reversible voltage dependent channel closing mechanism for porins incorporated into black lipid membranes, but also in the estimates of channel pore sizes based on the BLM derived conductances. Many porins have been found to display conductances which relate linearly to the specific conductance of the BLM bathing medium, reflecting the behavior one would expect from a simple, ohmic, water-filled pore. If one makes the assumption that the porin channels can be reasonably modeled as uniform cylinders, then one can use the following relation which scales the measured single unit conductance to the specific conductance in a linear fashion based on the geometry of the cylinder-like pore:

$$\frac{\Lambda}{\sigma} = \frac{\pi R^2}{L}$$

Equation 1

where Λ and σ are the single unit and specific conductance respectively. L is the length and R is the radius of the cylindrical pore.

Estimates of the pore diameters made for three E. coli porins, OmpF, OmpC and PhoE, based on measured conductances (Benz et. al. 1985) and equation 1 along with pore size estimates based on liposome studies are listed in Table 1. For the BLM based estimates the authors assumed a value of 60 A for the length of the cylindrical pore.

TABLE 1

PORE DIAMETER ESTIMATES (ANGSTROMS)
(LISTED UNDER RESPECTIVE DATA SOURCE)

	LIPOSOME EXPS.		BLM EXPS.
E.coli PORIN	EXCLUSION LIMITS a	PERMEABILITY RATES b	BASED ON CONDUCTANCE INCREASES c
OmpF	11.3	11.6	11.5
OmpC	11.3	10.8	10.2
PhoE	11.3	10.6	11.2

a) NAKAE 1976a

b) NIKAIDO AND ROSENBERG 1983

c) BENZ et. al. 1985

1.3.3 Reassessment of Pore Size Estimates

There exists a misnomer in the porin BLM literature. Various researchers have been referring to BLM measured porin trimer conductances as single channel conductances. These should be referred to as single unit or trimer conductances. The porin trimers of PhoE have been shown to consist of three independent water-filled channels (Jap 1989). BLM studies of PhoE have shown channel closings, manifested as conductance decreases, in three steps of one-third the peak trimer conductance per step (Dargent et.al. 1986). Indeed similar observations have been made for the major E. coli porins OmpF and OmpC (Engel et. al. 1985; Xu et. al. 1987). The issue was clouded upon publication of electron crystallography studies done on negatively stained double bilayer crystals of OmpF porin (Engel et. al. 1985). The authors concluded that these porin trimers consisted of three channels which merged midway through the protein and emerged as a single channel on the protein's opposite end. It is possible that the combination of working with stacked bilayers at a reconstruction resolution lower than that realized in the study of PhoE (Jap 1989) led to an interpretation of a structure very different from that indicated for PhoE. The existence of such a radical difference in structure and design between the major porins of E. coli and PhoE is difficult to reconcile in light of the strong homology in amino acid sequence between all three proteins. Even more convincing of the requirement for extensive structural similarity between these proteins is the fact that monomers of all three porins can interchange with one another to form all possible permutations of mixed monomer porin heterotrimers (Gehring and Nikaido 1989). So then, there are many arguments in favor of strong structural similarities between the porins OmpF, OmpC and PhoE and subsequently for a common mechanism of voltage dependent gating.

Channel pore diameter estimates determined from conductances measured in BLM experiments should therefore be based on one-third the value of the reported "single channel" (porin trimer open state) conductances. When such an analysis is performed one obtains the results listed in Table two. These new values include ones based on the cylindrical pore length used in the literature, 60 A, and another set derived using a length of 45 A which more closely fits the results from electron crystallography of negatively stained specimens (Jap 1989). What one immediately notices is that these revised estimates of the pore diameters do not compare well with the values derived from liposome swelling and efflux/exclusion experiments. Although these new estimates are based on the appropriate conductances, they must still be considered as underestimations of the porin pore diameters (H. Lecar, personal communication). Sources of potential error in estimating pore diameters from conductance measurements are porin structural deviations from the assumed cylindrical pore geometry, estimation of the pore's length and the assumption that the experimental system's bulk conductance applies to the channel interior, especially for solutes that approach the exclusion limit. The accuracy of the estimates could be significantly improved by compensating for the contributions of other effects not included in the standard methodology such as contributions to channel conductance associated with solute access to the pore mouths (Hille, 1984), the energetics of transferring a molecule from a medium of one dielectric constant to that of another (Born energy) and solute/channel interactions.

TABLE 2

MODIFIED BLM-BASED PORIN PORE DIAMETER (A)

(based on single step conductance decreases a))

	Assumed Channel Length	
	60 A	45 A
OmpF	6.6 (5-7)	5.7
OmpC	5.9 (5-6)	5.1
PhoE	6.5 (5-7)	5.6

a) The numbers given represent the average value obtained upon consideration of results reported for a variety of different diffusing ions and concentrations used (Benz et. al. 1985). The numbers in the parentheses reflect the range of conductances measured across the variety of salts used.

The pore diameters predicted from liposome swelling experiments were determined by best fitting the Renkin equation (Renkin 1954) to the porin permeabilty rates measured for various solutes (Nikaido and Rosenberg, 1981; Nikaido and Rosenberg, 1983). As seen in column two of Table one, the estimates obtained from experiments with OmpF, OmpC and PhoE porins lie in a range of 10 - 12 A. As is the case for BLM based estimates, deviation of the true channel geometry from that of a constant diameter cylinder could affect the accuracy of pore diameters predicted. Additionally, the use of a Stokes radius as an estimate for the radius of a test solute needed to apply the Renkin equation could cause an overestimation of the channel's pore size. Error in pore size predictions can also arise from inaccuracy in the value of the membrane thickness used to caluclate permeabilty coefficients from the Renkin equation results.

In an assessment of exclusion limit based estimates of E. coli and S. typhimurium porin pore diameters, it is important to note that these values are derived from the Stokes radius of the excluded solute, in this case raffinose (Nakae 1976a,b). It is possible, however, that the exclusion limit of a hydrophilic pore's constricting region is determined by the diameter of the dehydrated form of the largest molecule able to diffuse through the porin in question. Diffusion through a porin channel of a hydrophilic molecule close in size to the pore's exclusion limit, would be realized if the solute in question could exchange hydrogen bonds initially made with the hydrating shell of water for those that could be made between dehydrated solute and the chemical groups lining the "wall" of the channel constriction. Ideally, this test solute would be spherical in shape allowing for a direct assessment of pore diameter. Unfortunately, few of the many solutes assayed even come close to displaying this geometry. Therefore, in interpreting the results and conclusions of these exclusion limit investigations one needs to take into account the sterics involved in solute diffusion through the porin pores.

Raffinose, a linear trimer containing three hexose units, is essentially cylindrical in shape with a diameter very similar to that of glucose. The major porins of E. coli are not, in fact, impermeable to raffinose (Decad and Nikaido 1976) but there is a dramatic difference in porin permeability of raffinose compared to glucose. Although the narrowest dimension of glucose and raffinose are comparable, thermal motions along the length of raffinose would cause it to sweep out a larger volume of space, effectively presenting a wider diameter solute to the porin pore. The net effect of this impediment would be the requirement that molecules of raffinose would literally have to "worm" their way through the channels. In liposome swelling studies it was demonstrated that although solutes may have similar molecular weights, they may have significantly different rates of porin permeability (Nikaido et al. 1983). This is an indication that for solutes of similar molecular weight, yet dissimilar porin permeabilities, slower permeating ones must be geometrically closer to the pore's exclusion limit than ones permeating more rapidly. Nikaido and co-workers (Nikaido et al. 1983) noted a halving in relative rates of porin permeability going from L-arabinose (a pentose) to D-glucose (a hexose). Disaccharides evaluated in the same series of experiments demonstrated even greater reductions in permeability while having the same effective cross-sectional diameter as glucose. Hydrated glucose has an approximate diameter of 8.5 A. It's relative permeability indicates that it is very close in size to the steric limit of the channel constriction. Experiments with zwitterionic cephalosporins, having an approximate minimum diameter of about 7 A, demonstrated that they can pass through porin pores with relative ease. It was also noted that very hydrophobic cephalosporins, again with an approximate minimum diameter of 7 A, did not diffuse through the pores (H. Nikaido, personnal communication; Nikaido et. al. 1983; Nikaido and Rosenberg 1983). In water, hydrophobic molecules like these are believed to be surrounded by a "cage" of ordered water molecules. In a porin pore the removal of this water, for hydrogen bond exchange with atoms of the channel walls, would be an energetically unfavorable process. For molecules sterically unable to pass through the pore without "shedding" associated water this would present a formidable permeability barrier. It appears therefore, that the minimum diameter of the water "caged" version of these hydrophobic cephalosporins exceeds the dimensions of the pore's constriction region.

To summarize, the pore diameters estimated from the conductance contibutions of single channels are, on average, significantly lower than those diameters predicted from permeability rate and exclusion limit data. With an assumed channel length of 60 A, the largest pore diameter predicted from the appropriate BLM data was 6.6 A for OmpF porin. Even this value is less than the approximate 7 A minimum diameter of zwitterionic cephalosporins shown to be able to diffuse rather easily through porin channels, including OmpF. Pore diameter estimates derived from permeability rate studies of OmpF, OmpC and PhoE fall into a range of 10 - 12 A. The current exclusion limit data appears to be more appropriate for indicating an upper and lower bound for pore diameter estimates rather than one particular value. An estimated range suggested by experiments with cephalosporins is a lower bound of 7 A and an upper bound described as the minimum diameter of a water "caged" hydrophobic cephalosporin.

1.3.4 Porin Voltage Gating in Intact Cells

A controversy of a different kind also exists as a result of the BLM measurements on porin conductance, it concerns whether the property of voltage regulated conductance is solely an in vitro phenomenon. Bilayers used in the BLM experiments differ significantly from those of bacterial outer membranes with respect to lipid composition and distribution. These differences in turn might affect the physical and structural properties of the bilayer including the porins within it. An additional concern is the magnitude of the applied membrane potential required to achieve stepwise conductance decreases. Channel closings in PhoE trimers were found to begin at about 80 mV (Dargent et.al. 1986) while OmpF required as low as 50 or as high as 140 mV to achieve similar results depending on the experimental preparations used (Schindler and Rosenbusch 1978 1981; Xu et.al. 1986).

To address the question whether voltage-dependent conductance decreases of the outer membrane play an in vivo role, Nikaido and co-workers (Sen et. al. 1988) investigated whether Donnan potentials could modulate porin permeability in intact E. coli bacteria. By varying the concentrations of electrolytes in the bacterial suspension medium, the magnitude of the Donnan potential could be manipulated. The range of ionic strength conditions surveyed allowed for the assessment of membrane permeability over a range of Donnan potentials from 5 to 100 mV. It was found that under the conditions tested, the permeability of the porins OmpF and OmpC was not measurably altered. Although this result makes quite a strong case against voltage-dependent gating of porins in intact cells, one could still press the point that experiments with intact cells using even higher Donnan potentials (100- 200 mV, far above physiologically relevant levels) might be required before one could detect an alteration in permeability.

1.3.5 Chemical Modification of Porins

The use of chemical modification experiments on porins has provided insight into the elements governing a porin channel's selectivity. In the case of OmpF porin, amidation of the protein demonstrated that its selectivity for cations over anions is due to negatively charged amino acids distributed along the protein's surface as well as inside its pore (Benz et. al. 1984). Acetylation of the positively charged amino acids in PhoE renders the porin cation selective in sharp contrast to its native preference for anions (Darveau et. al. 1984). Both of these experiments, while modifying porin selectivity did not significantly modify the porin's single channel conductances. When solvent accessible lysines of OmpF, OmpC and PhoE were chemically modified by the attachment of large (8.6 Å diameter by 3.6 Å width) trinitrophenyl groups, all three porins developed a high selectivity for cations over anions. Although all three porins were modified by this treatment, only PhoE suffered a significant drop in conductance implying that the chemically modified lysines of PhoE were in closer proximity to the pore constriction than in OmpF and OmpC (Hancock et. al. 1986).

1.3.6 Analysis of Genetically Altered Porin

Experiments have been performed on PhoE porin in which the primary sequence has been altered from that of native PhoE. Genetically altered porin expressed in mutant strains was assayed for its ability to bind bacteriophage TC45 which is known to bind PhoE in its native form. Cells expressing PhoE but resistant to phage TC45 binding were selected for and the gene encoding the porin was sequenced and analyzed. Arginine 158 of the native gene was found to have mutated to a histidine, rendering the mutant cell phage resistant and therefore identifying this particular residue as present at the cell's outer surface (Korteland et. al. 1985). Alterations of amino acids lying at the porin's extracellular surface have also been identified with the aid of monoclonal antibodies (Van der Ley et. al. 1985 ;

Van der Ley et. al. 1986). PhoE expressing mutants which failed to bind antibodies, raised against native PhoE trimers, survived an antibody-dependent complement reaction to which they were subjected. Surviving cells were cloned and their PhoE nucleotide sequences analyzed. From the range of surviving cells were noted three frequently substituted amino acids, arginine 201, glycine 238 and glycine 275. Although these mutations prevented antibody from binding, all of these cells were still susceptible to phage TC45. Monoclonal antibody studies have also been used to develop a model to suggest that both the amino and carboxy termini of PhoE porin are located on the protein's periplasmic face (Van der Ley et. al. 1986).

In a different series of experiments, hybrids were constructed from contiguous segments of OmpC and PhoE porin genes (Tommassen et. al. 1985 ; Van der Ley et. al. 1987). Chimeric proteins expressed from these hybridized genes were found to be able to bind the appropriate phages and monoclonal antibodies. More interestingly, chimeric porins in which an amino terminus section of PhoE was exchanged for its OmpC counterpart were shown to be effectively cation selective. Specifically, the anion selectivity of PhoE porin appears to be determined by amino acids localized to positions 1-11, 75-110 and 111-141 of the porin's primary sequence.

From these and other observations, Tommassen has developed a model for the secondary structure of PhoE porin (Tommassen 1988). He has proposed that a PhoE porin monomer is assembled in a manner such that 8 distinct hydrophilic regions are positioned at the cell's extracellular surface. Because structural data to date has indicated that porin's secondary structure is almost exclusively beta-sheet, he has further proposed that these 8 regions represent 8 beta-turns and are the connecting regions for 16 transmembrane beta-strands.

The findings of many of the above experiments will be of particular importance to our group when we have obtained a high resolution density map of PhoE. The spatial assignment of specific amino acids to hydrophilic surface segments or to regions of the pore interior will serve as helpful boundary conditions in the process of fitting the peptide sequence to the density map.

1.4 Structural Properties

1.4.1 Primary Structure Analysis

The amino acid sequences of the E. coli porins OmpF, OmpC and PhoE have been deduced from their nucleotide sequences (Inokuchi et. al. 1982 ; Mizuno et. al. 1983 ; Overbeeke et. al. 1983). The amino acid sequences of all three of these porins are highly homologous. OmpF, OmpC and PhoE for example, have greater than 60% amino acid sequence homology (Overbeeke et. al. 1983). The amino acid sequences of these proteins also contain a large number of negatively and positively charged residues. When the charges of the amino acids in each of the porins is added up, one finds that each of the three porins contains a net negative charge. Fourteen negative charges in OmpC, eleven in OmpF and nine in PhoE. Based on the results of numerous chemical modification experiments, it is believed that the majority of these charges, positive and negative, are not solvent accessible but rather are involved in the protein-protein association of the monomeric units comprising the porin trimers (Benz 1985) . It appears then, that some subset of those remaining amino acids, not involved in the maintenance of the trimer structure, is what gives the various porin pores their ion selectivity, negative charges assisting OmpF and OmpC in establishing its cation selectivity and positive charges helping to provide the anion selectivity measured in PhoE.

The amino acid sequences of E. coli porins OmpF and LamB were analyzed for their hydrophobicity (Vogel and Jahnig 1986). They were found to have extraordinarily low total hydrophobicities when compared to proteins located in the inner membrane or even the periplasm of E. coli. The primary sequence of OmpF was further assessed for the occurrence of amphipathic stretches of amino acids compatible with the cases of alpha-helical or beta-strand transmembrane conformations. Based on this analysis OmpF was shown to have the potential for two amphipathic alpha-helices and 12 amphipathic beta-strands. We have performed a similar analysis on the primary sequence of PhoE, the results of which are given in Figures 3 through 5. From these plots we see that PhoE has, by the same standards applied to OmpF in Vogel and Jahnig's paper, no potential amphipathic alpha-helices and 12 amphipathic beta-strands. Applying a more liberal hydrophobicity threshold one can easily obtain more than 20 candidate amphipathic beta-strands.

Figure 3. Hydrophobicity analysis of PhoE amino acid sequence using the hydropathy scale of Kyte and Doolittle (1982) as described in Vogel and Jahnig (1986). Figure 3 shows the hydrophobicity profile considering a simple seven amino acid averaging window. Such a profile is useful in detecting peptide segments which may be sufficiently long and hydrophobic to traverse the lipid bilayer without exposure to an aqueous environment. In the initial stages of analysis an averaging window of seven amino acids is typically used. A window of this length is wide enough to average out spurious changes in hydrophobicity, yet short enough to provide good resolution of hydrophobicity trends. In addition to the graph of window averaged hydrophobicity plotted in figure 3 are two horizontal lines. The upper line is placed at a value of 1.6 on the hydrophobicity index scale and is used as an indicator as to whether a given hydrophobicity curve peak is hydrophobic enough to be associated with a transmembrane segment of protein. The value of 1.6 was derived by Kyte and Doolittle (1982) on the basis of their study of the bacteriorhodopsin amino acid sequence. The lower line is set to reflect the average hydrophobicity of the entire sequence. If in such a plot evidence of long hydrophobic sections of amino acids is found, the sequence can be reassessed using averaging windows of 10 or 20 amino acids in length to indicate potential locations of beta-strands or alpha-helices respectively. In the case of PhoE there are two such long,

hydrophobic segments.

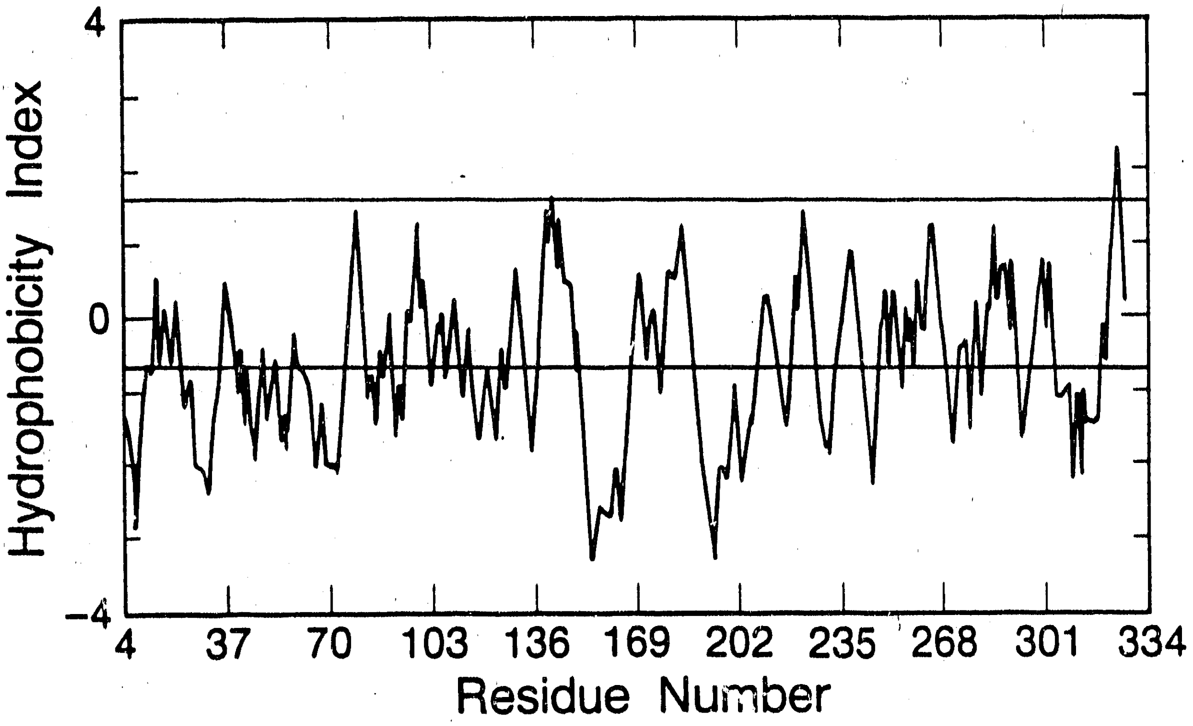
Hydrophobicity Index
4
0
−4
4
37
70
103
136
169
202
235
268
301
334
Residue Number

XBL 897-5168

Figure 4. Hydrophobicity analysis of the PhoE amino acid sequence to show the possible location of amphipathic alpha-helicies, which represent one of the likely structural motifs for the formation of an aqueous, transmembrane channel. The graph was produced using an algorithm described in Vogel and Jahnig (1986). In this analysis hydrophobicities of amino acids falling within an averaging window are weighted so as to detect the occurence of hydrophobic residues with a period of 3.6 residues in the segment in question. The width of the window is chosen to predict the possible sequence locations of the hydrophobic faces of alpha-helices 20 residues long. The horizontal lines seen in the plot are as described in figure 3. When a residue is associated with a hydrophobicity average which is greater than or equal to the level of the upper line and is immediately neighbored by residues whose associated hydrophobicity averages are much less than the upper line level, it is an indication that the amino acid in question is a good candidate for being located midway in a segment of amphipathic alpha-helix. In the case of PhoE there are no segments capable of forming amphipathic helices.

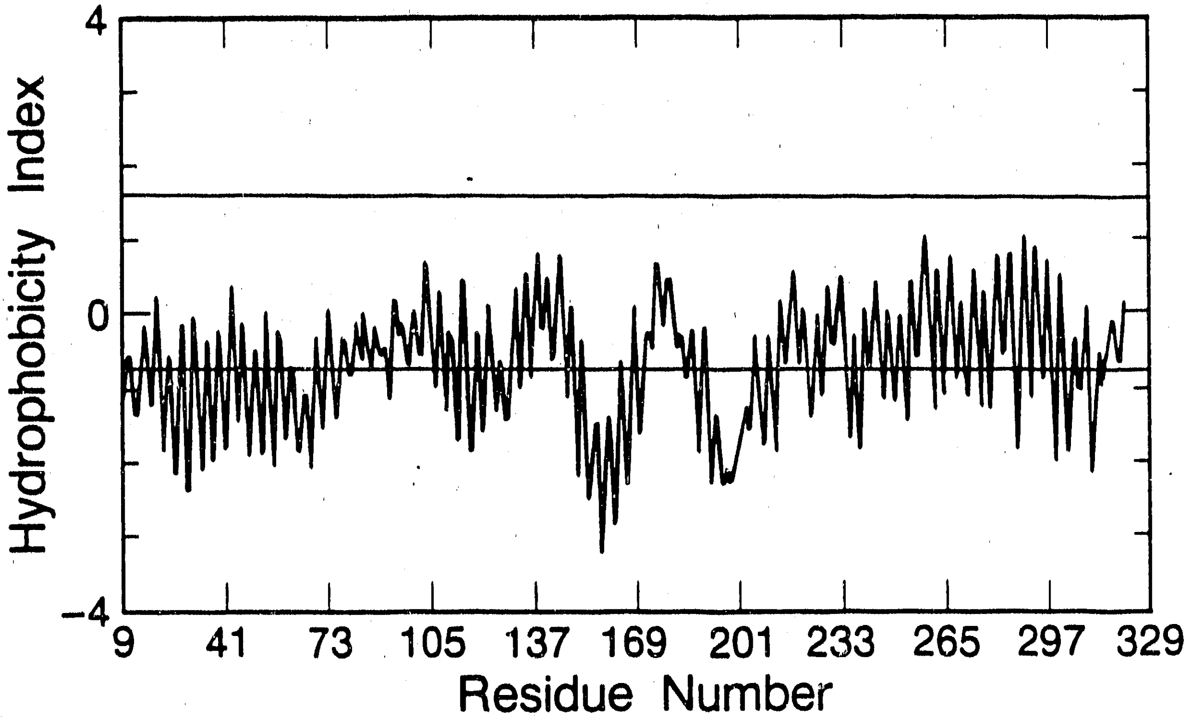
Hydrophobicity Index
4
0
−4
9
41
73
105
137
169
201
233
265
297
329
Residue Number

XBL 897-5169

Figure 5. Hydrophobicity analysis of the PhoE amino acid sequence to show the possible location of amphipathic beta-strands. The graph was produced using an algorithm described in Vogel and Jahnig (1986). In this analysis hydrophobicities of amino acids falling within an averaging window are summed so as to detect the occurence of hydrophobic residues with a period of 2 residues in the segment in question. The width of the window is chosen to predict the possible sequence locations of the hydrophobic faces of beta-sheet strands 10 residues long. The horizontal lines seen in the plot are as described in figure 3. When a residue is associated with a hydrophobicity average which is greater than or equal to the level of the upper line and is immediately neighbored by residues whose associated hydrophobicity averages are much less than the upper line level, it is an indication that the amino acid in question is a good candidate for being located midway in a segment of amphipathic beta-sheet. Several segments of potential amphipathic beta-sheet are identified in PhoE in this way.

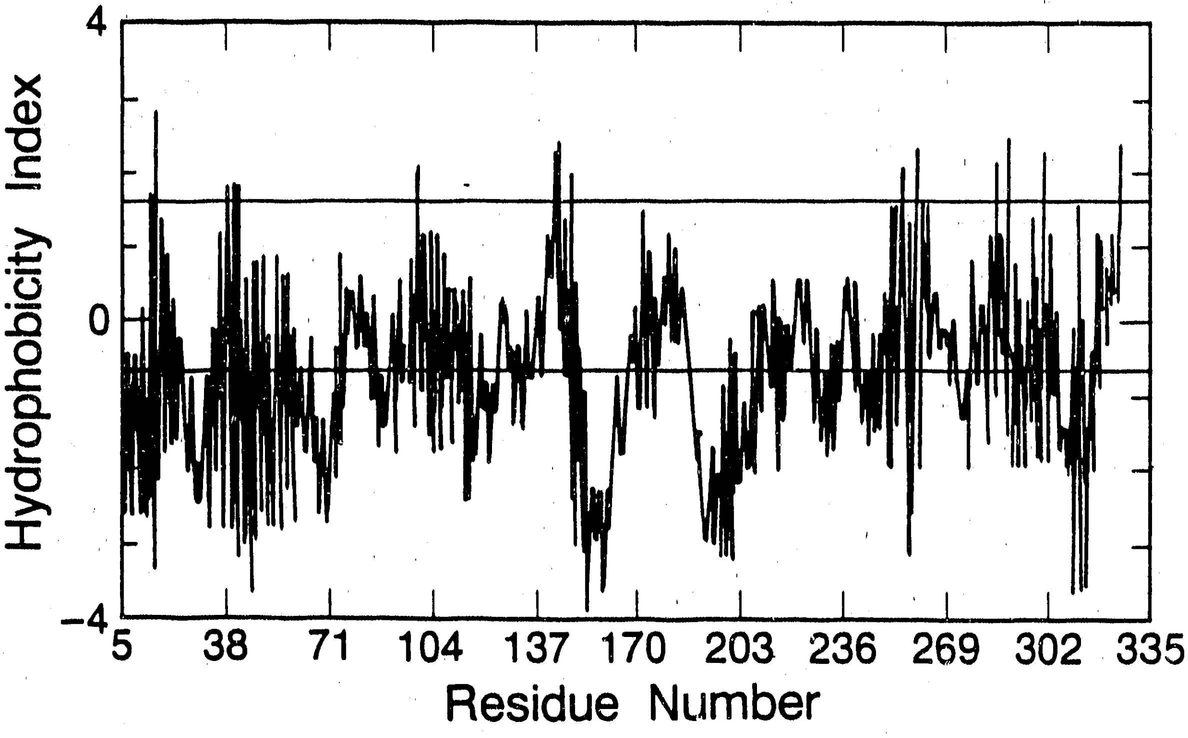

Hydrophobicity Index
4
0
−4
5
38
71
104
137
170
203
236
269
302
335
Residue Number

XBL 897-5170

The amino acid sequence of OmpF porin has also been analyzed with the Chou-Fasman secondary structure prediction algorithm (Vogel and Jahnig 1986). Although the results predicted the possibility of a significant fraction of alpha-helix, the predominant structure predicted was beta-strand. It is interesting to note that the predicted segments of beta-strand are almost uniformly distributed throughout the entire sequence. We have again performed a similar analysis on PhoE and the results are given in Figure 6.

Based on structural information obtained to date, it is believed that a significant portion of E. coli porin protein can be reasonably approximated as a cylinder of beta-sheet. With values for the cylinder geometry one can estimate the number of amino acids needed to generate such a beta-sheet cylinder. The circumference of the vestibule mouth of PhoE porin has been estimated to be about 100A (Jap 1989). If one determines the maximum sized polygon able to fit within this circumference and keeping the length of its faces equal to the interstrand spacing in beta-sheet (4.8A), an estimate of 21 beta-strands per beta-sheet cylinder is obtained. X-ray diffraction studies indicate that these beta-strands are between 10 and 12 amino acids long (Kleffel et. al. 1985), barely long enough to traverse the hydrophobic core of a typical bilayer. The approximate number of amino acids neccessary to complete

Figure 6. Secondary structure prediction of PhoE porin based on its primary sequence and the algorithm of Chou and Fasman (Chou and Fasman 1978). Letter indications as as follows: a) amino acid sequence number; b) amino acid sequence (single letter abbreviation); c) indication of charged amino acids; d) predicted alpha-helix; e) predicted beta-sheet; f) predicted turns; g) best estimate for sequence regions where both alpha-helix and beta-sheet predicted (A for alpha-helix, B for beta-sheet).

```
         10        20        30        40        50        60        70        80     a
AEIYNKDGNKLDVYGKVKAMHYMSDNASKDGDQSYIRFGFKGETQINDQLTGYGRWEAEFAGNKAESDTAQQKTRLAFAG     b
 -   +-  + -   + +  .   -   +- -    +   + -    -      + - -    + - -    + +          c
<---->      <--------->            <------------->     <------------------------     d
          SSSSSSS  SSSS         SSSSSSSS   SSSSSSSSSS               SSSSSSSSSS       e
     TTTT               T   TTTTT        T     T         T   TT   T    T             f

            BBBBB  AAAA            BBBBB   BBBBBBB                  AAAAAAAAAA       g



         90       100       110       120       130       140       150       160
LKYKDLGSFDYGRNLGALYDVEAWTDMFPEFGGDSSAQTDNFMTKRASGLATYRNTDFFGVIDGLNLTLQYQGKNENRDV
 + +-    -  +      - -   -   -   -     -    ++       +  -     -          + - +-
----->          <---------->         <-------->         <-----> <-------->   <--
              SSSSSSSSSSSSSSSSS      SSSSSSS     SSSSSSSSSSSSSSSSSSSSSSS
            T                   TTT    T    T         TT                TTTTTT

                AAAAAAAAAAAA         BBBBBBB            BBBBBBB BBBBBBBB



       170       180       190       200       210       220       230       240
KKQNGDGFGTSLTYDFGGSDFAISGAYTNSDRTNEQNLQSRGTGKRAEAWATGLKYDANNIYLATFYSETRKMTPITGGF
++   -        -    -          -+  -     +   ++ -      + -           - ++
-->                 <---->                  <--------->     <---->             <
       SSSSSSSSS                   SSSS          SSSSSSS    SSSSSSSSSSSSSSSSSSSS
 TTTTT   T       TT     T   TTT   TT   TT   T      T                T        T

                                                 AAAAAA     BBBBBB             B



       250       260       270       280       290       300       310       320
ANKTQNFEAVAQYQFDFGLRPSLGYVLSKGKDIEGIGDEDLVNYIDVGATYYFNKNMSAFVDYKINQLDSDNKLNINNDD
  +    -       -   +        + +- -   ---     -        +      - +    - - +     --
------------------>      <--------------->            <------------->         <-
   SSSS  SSSSSSSSSS   SSSSS             SSSSSSSSSSSSSSSSSSSSSSSSSSSS
 T  T               T       TTT      TT               T              TTT     TT

   BBBB  BBBBBBBBBB      BB             BB            BBBBBBBBBBBBBB



       330
IVAVGMTYQF

----->
SSSSSSSSSS


BBBBBB
```

XBL 899-5207

this structure, assuming the beta-sheet strands are parallel to the cylinder axis, is the product of 21 beta-strands and a maximum of 12 amino acids per beta-strand. This product, 252 amino acids, would account for over 75% of the total amino acids available, yet leave enough amino acids left over to account for the required beta-turns.

1.4.2 Secondary Structure Analysis

The porins of E. coli have been the subject of many spectroscopic measurements. Circular dichroism (Rosenbusch 1974 ; Nakamura and Mizushima 1976), infrared spectroscopy (Nakamura et. al. 1974 ; Rosenbusch 1974) and Raman spectroscopy (Vogel and Jahnig 1986) measurements all indicate these porins to be predominately of beta-sheet conformation with no alpha-helix structure. The gross orientation of the beta-sheet structure backbone has been inferred from X-ray (Garavito et. al. 1983) and electron microscopy (Jap 1988) and infrared spectroscopy (Garavito et. al. 1982) studies to be oriented normally to the plane of the membrane. Subsequent infrared analysis has determined that these beta-sheets are of the anti-parallel type (Kleffel et. al. 1985). Most recently, infrared linear dichroism studies have indicated that although the beta-sheets themselves are oriented essentially perpendicular to the membrane plane, the strands making up the sheets have an average tilt of about 45 degrees from the membrane plane (Nabedryk et. al. 1988).

1.4.3 Tertiary Structure Analysis

Functional porins of E. coli are extracted from membrane preparations as trimeric units (Steven et. al. 1977; Dorset et. al. 1983). The monomers making up the trimer units are very strongly associated, as evidenced by the fact that they cannot be separated from one another unless they are denatured (Nikaido and Vaara 1985). The major porins of E. coli, OmpF and OmpC, as well as PhoE all have monomeric molecular weights of approximately 37kDa.

1.4.3.1 Electron Microscopy of Negatively Stained Specimens

OmpF porin has been crystallized into two-dimensional arrays suitable for electron crystallographic study. Initial studies of those crystals embedded in negative stain revealed clusters of three holes or indentations where the stain could collect, believed to correspond to the porin unit trimer (Dorset et. al. 1983). Subsequent tilt series analysis of the crystal type, again in negative stain, yielded a three-dimensional reconstruction of the OmpF channels to about 25A resolution (Dorset et. al. 1984 ; Engel et. al. 1985). From this data one can clearly see stain-filled channels penetrating the membrane. The authors' interpretation of the three-dimensional density map was that in each trimer three independent channels beginning at one end of the porin would merge into a single channel midway through the membrane prior to exiting the protein.

An untilted projection reconstuction of OmpC two-dimensional crystals in negative stain was accomplished by Chang et. al. (Chang et. al. 1985). The reconstruction clearly showed three stain-filled pores.

PhoE porin has also been crystallized into two-dimensional arrays. A three-dimensional reconstruction of the specimen in negative stain was obtained to a resolution of approximately 20A (Jap 1986; Jap 1989). As with OmpF, the three-dimensional map shows that PhoE porin consists of trimers of stain-filled channels as the basic unit. Unlike OmpF, the channels in PhoE, although gradually converging towards one another as they traversed the membrane, did not merge but remained as three separate channels. Each stain-filled pore is about 22A in diameter and about 35A long. The map shows that these are not stain-filled along the full length of the membrane but stop short, indicating that one end of each pore is small enough to exclude stain. The net picture described by these findings is a trimer of pores, where each pore begins with a vestibule like domain at one end of the protein (with a diameter of about 22A) extending through the membrane for approximately 35A, whereafter it continues via a much smaller pore (inaccessible to the stain molecule uranyl acetate) until exiting the membrane.

1.4.3.2 Electron Microscopy of Unstained Frozen-hydrated Specimens

The projected structure of unstained, frozen-hydrated OmpC porin was determined to a resolution of 13.5A via electron microscopy (Chang et. al. 1985). This projection reconstuction showed the general molecular outline of the protein encircling the pores of the unit trimer, but the resolution was not sufficient to discern the protein's secondary structure features. Of further interest was the finding of a relatively low density region at the center of the trimer, too low a density to be that of protein but too high to be that of a water filled pore. It was suggested by the authors that this area was most likely occupied by lipid, with enough room to accomodate three lipid A molecules on each side of the bilayer.

1.4.3.3 Electron Microscopy of Sugar Embedded Specimens

A high resolution projection reconstruction of glucose embedded OmpF porin has been generated (Sass et. al. 1989). This projection, which has a resolution of approximately 5 A, was generated through a combination of electron crystallography and image correlation averaging techniques. The most prominent structures in the reconstruction are the three "rings" of high density arranged equilaterally to form the unit trimer. The authors suggest that these "rings" outlining each of the monomers are composed of beta-sheet oriented perpendicular to the plane of the membrane. They also called attention to a region of very low density in the center of the trimer, but offered no suggestion as to its source.

PhoE porin embedded in glucose has also been the subject of a projection reconstruction study (Jap 1989). As in the case with OmpF, here too the projection map shows three high density elliptical "rings" associated to form a unit trimer. Like the authors of the OmpF study, Jap also likens the high density "rings" to an end-on view of a cylindrical beta-sheet oriented perpendicular to the membrane. The elliptical "rings" believed to be a projection of the walls of the pore vestibules measure 38A and 28A along the major and minor axes respectively. This map shows one additional similarity to the OmpF reconstruction of Sass et. al., that is the low density region at the center of the trimer. In his paper Jap suggests that this low density area might be filled with glycolipid which could play a role in maintaining the trimer's structure as well as shape the electric potential around the "mouths" of the pores.

Section I B.

Structure analysis by electron microscopy

Electron microscopy has been used to reconstruct the three-dimnensional structure of a number of membrane proteins to varying degrees of resolution. The most notable success to date has been in the studies of bacteriorhodopsin which have resulted in the determination of its three-dimensional structure to 6.5 A (Unwin and Henderson 1975; Henderson and Unwin 1975; Leifer and Henderson 1983; Tsygannik and Baldwin 1987) and in projection to a resolution of 2.8 A (Henderson et. al. 1986 ; Henderson et. al. 1988)

Electron crystallography is fundamentally like any other crystallographic reconstruction technique in that it requires the determination of Fourier structure factors. A significant difference between electron crystallography and X-ray crystallography lies in the strength of interaction between specimen and source quanta. Electrons are scattered on average about a million times more strongly from a specimen's constituent atoms as are X-ray photons. The degree of electron/specimen interaction is such that electron crystallography is ideally suited for studies of micrometer sized monolayer crystals, wheras X-ray studies require "large" three-dimensional crystals for the generation of measurable diffraction.

Another important difference arises from the methods used in gathering and processing the structural data. Researchers conducting X-ray studies obtain intensities (and subsequently structure factor amplitudes) directly from diffraction patterns but must resort to additional heavy-atom labeling methods to obtain structure factor phases. Using the techniques of electron crystallography one can obtain intensities/amplitudes directly from electron diffraction patterns and phases directly from image micrographs.

The fourier transform of three-dimensional crystals of the type used in X-ray crystallographic studies yields a three-dimensional lattice of diffraction spots (see Figure 7).

The three-dimensional lattice of diffraction spots can be modeled as arising from the intersection of three sets of parallel planes, one set of parallel planes for each principal axis in the crystal, and with interplanar spacings equal to the reciprocal of the real space unit cell dimension for each respective principal axis (Cantor and Schimmel 1980). The diffraction geometry resulting from studies of two-dimensional or monolayer

Figure 7. Diffraction intensity lattice derived from a three-dimensional crystal. The phenomenon of wave diffraction by a three-dimensional crystalline object can be described mathematically as the Fourier transform of that object.

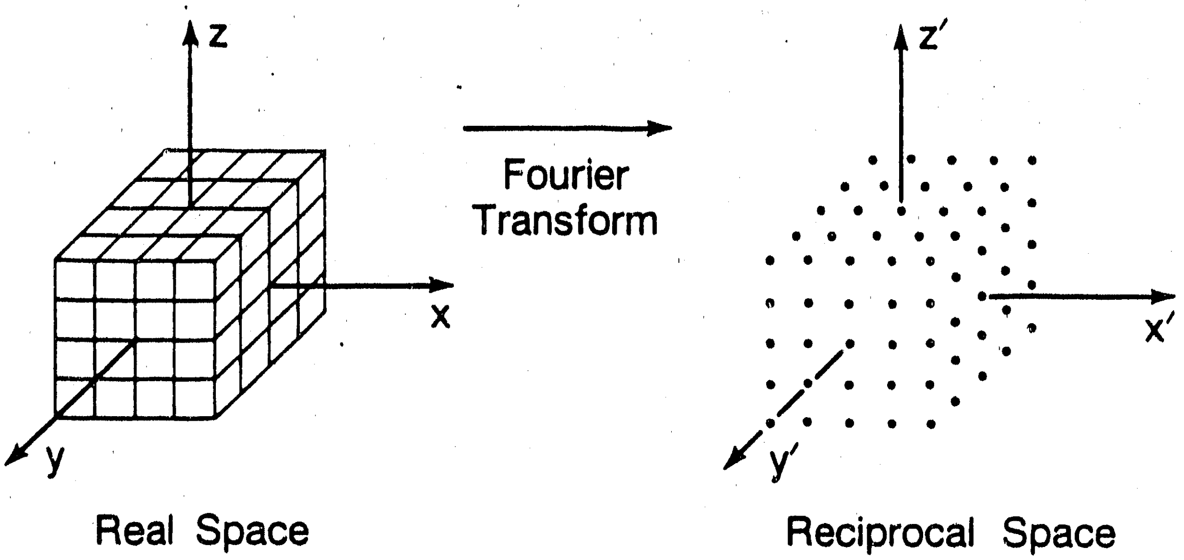

XBL 897-5138

crystals can be described as the result of two intersecting arrays of parallel planes yielding a lattice of structure factor lines which are parallel to the direction in which the crystal is one unit cell thick. (see Figure 8).

Intensity data is no longer a series of discrete values along the third axis but a continuum of values. These lines of structure factor data must therefore be sampled at some minimum spacing which is the reciprocal of at least twice the membrane thickness so that a reliable fascimile of the original data can be reconstructed by interpolation. Diffraction "spot" patterns are, in a simple geometric analogy, the result of the intersection of the specimen plane, or central section, and the continuous lattice rods/lines. (see Figure 9)

Sampling along the length of the lattice rods is accomplished by tilting the specimen through a range of angles with respect to the incident electron beam. Due to mechanical and other practical considerations, the range of specimen tilt usually covered is about +/- 60 degrees from horizontal, (see figure 10a) meaning that not all the available structural information of an object's Fourier transform will be sampled. When swept over the full range of azimuth these unsampled areas describe a missing volume of data which is often referred to as the "hollow cone". (see figure 10b)

Figure 8. Diffraction intensity lattice derived from a two-dimensional crystal. The phenomenon of wave diffraction by a two-dimensional crystalline array can be described mathematically as the Fourier transform of that object.

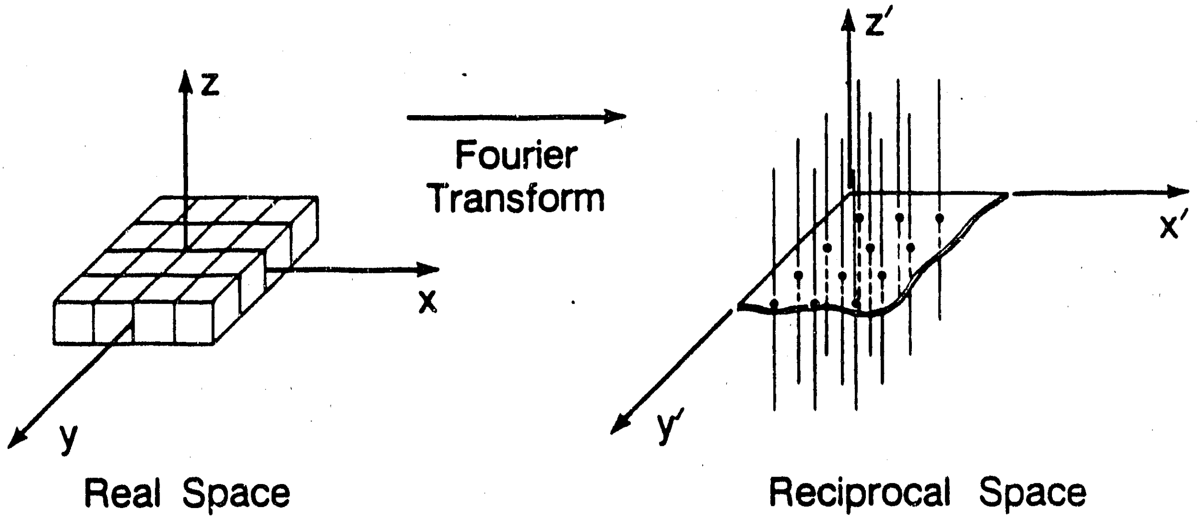

XBL 897-5139

Figure 9. Central section geometry. A diffraction pattern arises from the intersection of the sampling central section and the reciprocal lattice rod intensities.

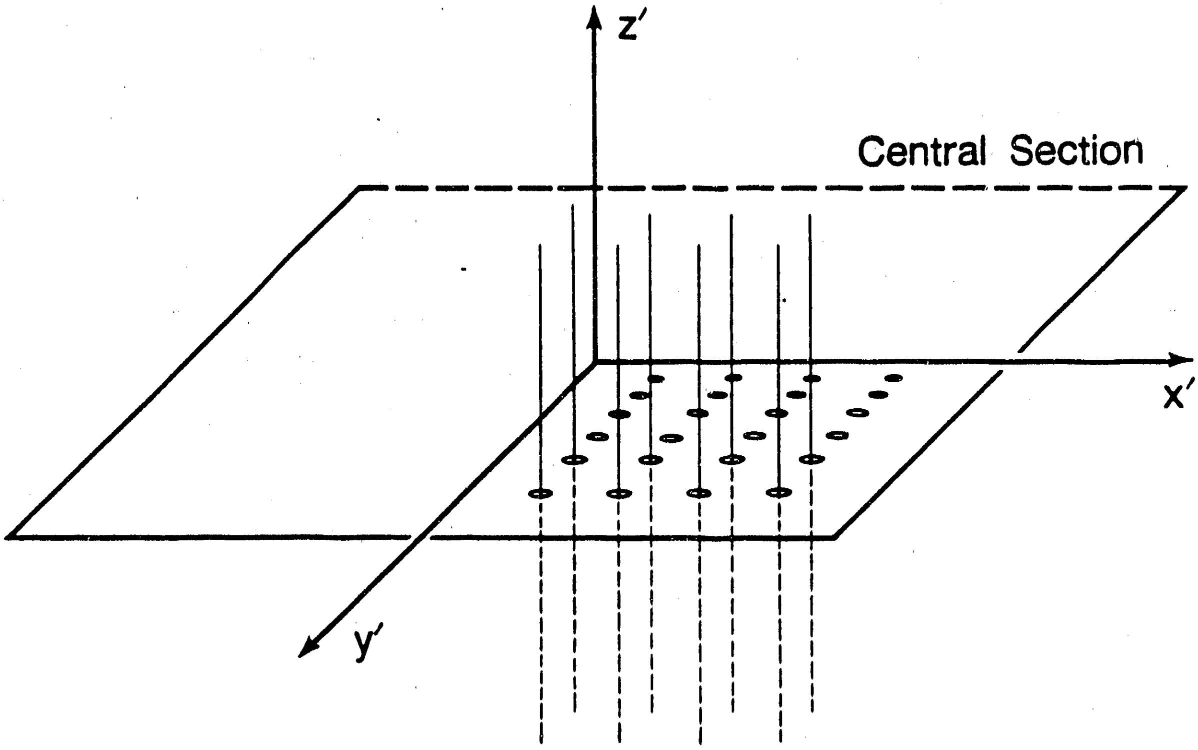

Diffraction pattern resulting from the intersection of the sampling central section and the reciprocal lattice rods.

XBL 897-5140

Figure 10. Central section sampling of reciprocal space. a) Sampling of reciprocal space is technically limited to roughly 60 degrees above and below the h,k,0 plane. b) When such a figure is rotated about the z* axis an hourglass-like region of reciprocal space remains unsampled. This unsampled zone is commonly refered to as the "hollow-cone" of missing data.

a)

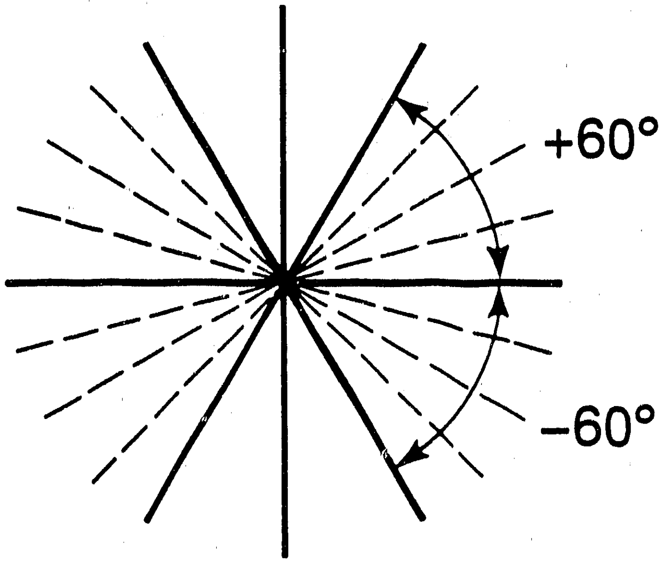

Central section sampling of reciprocal space

b)

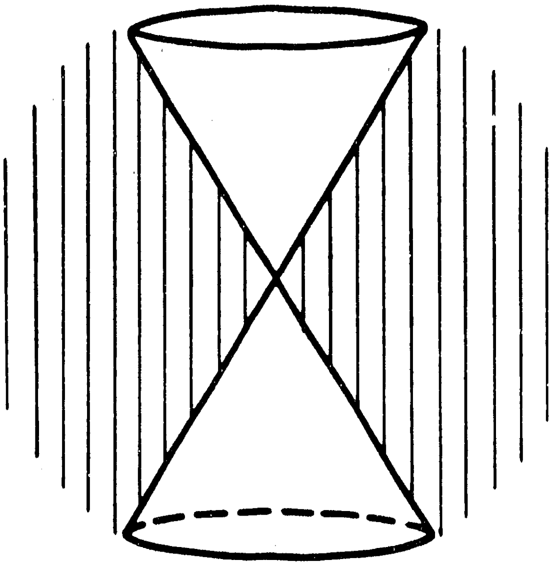

Hollow cone of unsampled reciprocal space

XBL 897-5131

It has been demonstrated, by numerical simulations, that the "hollow cone" of missing structure factor data does not deteriorate the interpretability of a 3-D density map if the the volume of reciprocal space which is sampled extends to a resolution of at least 3.5A (Glaeser et. al. 1988).

Phase data is gathered using the same general approach as described for sampling the intensity lattice rods. In this case the lattice rods represent the continuous phase values obtained from the Fourier transform of an image of a two-dimensional crystal. It is an important consequence of weak phase object theory that the crystallographic phase information is manifested as the relative origins of the sinusoidal intensity modulations (i.e. Fourier components) of the image.

The final step is to create a hybrid structure factor data set. The curves that have been fitted to data, sampled along the specimen lattice rods, can now themselves be sampled at some constant interval. Intensities are converted to amplitudes. Geometrically corresponding amplitude and phase values are then grouped into structure factor vectors. An inverse Fourier transform can be performed on this data set to generate the specimen's real space density map.

Section I C

Objectives of the thesis

This research has one major goal, that is to generate a set of three-dimensional structure factor amplitudes for use in the structure determination of the PhoE porin of E. coli. The data should cover specimen tilt in the range of at least +/- 60 degrees and extend out to a resolution of at least 3.5 angstroms. It should also be in a form suitable for hybridization with corresponding structure factor phases. To achieve the above, an initial objective to create sufficiently well preserved and flat specimens was also put forth.

Section II

Experimental Methods

2.1 Specimen protocols

2.1.1 Isolation and Purification

The procedure used by Dr. Bing Jap for the isolation and purification of PhoE porin is a modified version of the protocol described by Nikaido and Rosenberg (1983) and is briefly outlined below. A PhoE porin overproducing E. coli strain (K-12 JF694), with deletion mutations for OmpF and OmpC porin, is harvested after a 24 hour growth period. The bacteria are washed in 50 mM TRIS buffer containing protease inhibitors, DNAse and RNAse. To break open the bacteria, the cell suspension is run through a French press several times. Unbroken whole bacteria are removed from the preparation by centrifugation at 3,000 rpm for 10 minutes and removal of the resulting pellet. The supernatant is then centrifuged at 45,000 rpm for 30 minutes. The pellet formed in this step, containing bacterial membranes, is then resuspended in a "washing" solution of 2% sodium dodecyl sulfate (SDS) in a 10 mM TRIS based buffer adjusted to pH 7.5. This suspension is incubated at 32 degrees celsius for 30 minutes. It is at this stage that the outer membrane/peptidoglycan complex will begin to be separated from the inner membrane, which will be dissolved by SDS. Following the appropriate incubation period, spin this suspension at 45,000 rpm for 30 minutes keeping the temperature in the centrifuge above 15 degrees celsius to prevent the SDS from coming out of solution. Separate the pellet from the supernatant and resuspend the outer-membrane containing pellet in 10 mM TRIS buffer containing 2% SDS. Centrifuge this suspension again at 45,000 rpm for 30 minutes. Resolubilze the resulting pellet in an SDS sizing column running buffer (50 mM TRIS, 1% SDS, 0.4M NaCl, 3mM NaN3, 5mM EDTA). Incubate this suspension for two hours at 37 degrees celsius, followed by a final centrifugation at 30,000 rpm for 30 minutes. The resulting supernatant will contain solubilzed PhoE porin. This porin solution is then run through a molecular sizing column (15mm diameter, 1.2 m length) of Sephacryl S-200 (180 ml per column). The column is adjusted for a flow rate of 3 ml per hour while the fraction collector is set to collect 2 ml fractions. The porin is expected to elute after approximately 60 ml have run through the column. Collected fractions are assayed spectrophotometrically (280 nm UV absorption) as well as with SDS polyacrylamide gel electrophoresis, and the fractions containing the porin are passed through the column a second time. Purified PhoE porin is then prepared for crystallization or stored for future use.

2.1.2 Crystallization

Crystallization of PhoE porin into two-dimensional arrays involves the reconstitution of purified protein into lipid bilayers. This is accomplished by dialysis of a mixture of detergent solubilized protein and lipid (dimyristoyl phosphatidylcholine) in a ratio of 1:4 lipid to protein. The lipid/protein mixture is dialyzed against a 10mM TRIS buffer (0.1 M NaCl, 3mM NaN_3, pH 7.5) to which SDS has been added to a concentration of 0.4% w/w. Every four hours half the volume of the dialysis reservoir is replaced with new buffer which does not contain SDS. This procedure is maintained until crystals have begun to form, typically 2-3 days. Upon completion of the reconstitution process crystals are removed and washed twice in a 5 mM TRIS buffer to remove the high salt introduced in earlier steps. Washed crystals are subsequently treated with phospholipase A to remove excess lipid and increase the percentage of highly ordered two-dimensional crystals.

2.1.3 Specimen/Grid preparation

"Classical" electron crystallographic microscope grid preparation according to the bacteriorhodopsin paradigm makes use of "aged" hydrophobic carbon coated electron microscope grids. A few microliters of specimen (typically a 1 mg/ml suspension of monolayer crystals, in this example purple membranes) is placed on these grids along with a small volume of a one percent glucose solution and blotted dry (Baldwin and Henderson 1984). The glucose is added as a specimen preserver presumably replacing water and maintaining water-like contacts with the crystals and support film, embedding the specimen in a hydrated-like state. This technique, considering the extremely low volatility of glucose with respect to water, is ideally suited to maintaining the structural integrity of the protein in the high vacuum environment of the electron microscope.

In our experiments with PhoE porin, we have found that crystals of these proteins are most effectively studied on hydrophilic carbon coated electron microscope grids. Initially these types of grids were obtained on a trial and error basis, using carbon films "floated" onto electron microscope grids and tested for their hydrophilicity at various times after production. The carbon films are made by vacuum evaporating carbon onto sheets of freshly cleaved mica. The carbon film is removed from the mica when the carbon film/mica "open faced sandwich" is slowly pushed edge-on into a water containing vessel at some shallow angle to the horizontal. As the carbon film separates from the mica it is left to float on the surface of the water above a small piece of filter paper, covered with electron microscope grids placed in the vessel earlier. Prior to being placed in the vessel, the grids were rinsed in chloroform in an effort to remove any residues from their manufacturing process. The vessel is then slowly drained of water, eventually bringing the carbon film to rest on the filter paper and grids. The paper can then be removed with the carbon coated grids still attached and placed in a petri dish lined on the bottom with filter paper to facilitate drying.

The type of success obtained with conventionally made grids sampled over time for their hydrophilicity would vary over a range of extremes. There would be times when too much or too little specimen would remain on the grid, when too much or too little sugar would be present. Variations in grid hydrophilicity were even apparent on a local level. Neighboring windows of the same grid would often have sharply contrasting levels and forms of sugar coverage, specimen population and even specimen morphology. In an attempt to have greater control over the carbon film hydrophilicity and to achieve uniformity of results, we decided to glow-discharge our carbon coated microscope grids. Glow-discharging the grids in a low water vapor pressure environment for two minutes gave us negatively charged grids on a consistent basis.

In the course of our research we evaluated three different embedment sugars: aurothioglucose, glucose and trehalose. For reasons that are discussed in detail in the Results section, the sugar of choice turned out to be trehalose. We applied volumes of a 1.2 % w/w solution of trehalose in a ratio of 2 to one part of a 1mg/ml suspension of PhoE crystals on glow-discharged grids. The specimen/trehalose bead is left on the grid for about five minutes after which it is blotted away.

2.2 Collection of diffraction patterns

The experimental data for this thesis research was collected on a modified JEOL 100B top-entry electron microscope. Modifications include a liquid nitrogen cooled stage (Hayward and Glaeser 1980), and a "low dose kit". Specimens were examined under low dose conditions (less than 1 electron per square Angstrom per minute) in a defocused diffraction mode to maximize crystal contrast. When a promising patch was found, the stage was adjusted to place the center of the patch on the microscope's optical center. The shutter was then closed and the microscope was switched to a higher dose diffraction mode, such that the patch would receive a total dose of 1-3 electrons per square angstrom over an exposure time of 5-10 seconds. The shutter was then opened and the film exposed. Under these conditions processable diffraction patterns, over a range of 0 to 60 degrees specimen tilt, were obtained with about a one in five exposure success rate.

2.3 Processing of diffraction patterns

2.3.1 Scanning and indexing

Selected diffraction pattern films were scanned on a Perkin-Elmer PDS microdensitometer. The scanning aperture used was 12.5 micrometers square and was rastered in 13 micrometer steps in the x and y directions. This scanning raster was more than sufficient to properly sample even the smallest diffraction spots. The size of the scanned arrays ranged from 2400 to 2800 pixels a side. These arrays were subsequently averaged down by a factor of four in x and y to yield 600x600 or 700x700 pixel arrays, which resulted in significant savings in computer storage and processing time.

The digitized patterns were then displayed on an AED 767 computer graphics monitor where they could be indexed using interactive software. Much of this display software was provided through the courtesy of the Medical Research Council (MRC) Laboratory of Molecular Biology, Cambridge, England. In selecting the diffraction patterns to be used for creating the initial lattice rod curves, several criteria were used in determining what specimen tilt angles were best suited for starting things off. For untilted specimens, we kept film plates whose diffraction patterns exhibited good mirror symmetry in the fashion expected for p21212 space group crystals. The Shaw and Hills algorithm (Shaw and Hills 1981) is used to determine the tilt angle and azimuthal or tilt axis orientation of each plate. The angles are calculated based on the geometric relationship of reciprocal space lattice vector components of the tilted pattern compared to those of the untilted patterns. A tilt angle and axis determined via this algorithm, and the results of a comparison of diffraction spot intensities lying along a pattern's tilt axis with corresponding spots from untilted reference patterns are strong indicators of crystal orientation in a tilted diffraction pattern. With these "tools" indexing of even highly tilted diffraction patterns could be done with confidence. A short-coming of note, the Shaw and Hills algorithm is only accurate for assessing diffraction patterns tilted by at least 20 degrees. Therefore we collected tilted data from patterns tilted by 30 degrees or more.

2.3.2 Radial background subtraction

Once the pattern has been properly indexed it can be further processed to correct for the effects of inelastically scattered electrons. Prior to this correction the diffraction spot intensities were "riding" on a radially varying background (see Figure 11a).

Average intensities are calculated along concentric "rings" moving radially out from the center of the pattern. The standard deviation about each radial average is also determined. The diffraction patterns are then revisited and those pixels whose intensity values are less than 3 standard deviations from the current "ring" average are used to create a new set of radial "ring" averages (see Figure 11b). The diffraction patterns are revisited once more and this time these radial background averages are subtracted from the approprite pattern pixels resulting in a removal of the effects of inelastically scattered electrons (see Figure 11c)

Figure 11. Treatment of radial background due to inelastic scattering of electrons. a) Electron diffraction intensities with superimposed radial background. b) Average radial background component. c) Resulting intensity distribution after removal of average radial background.

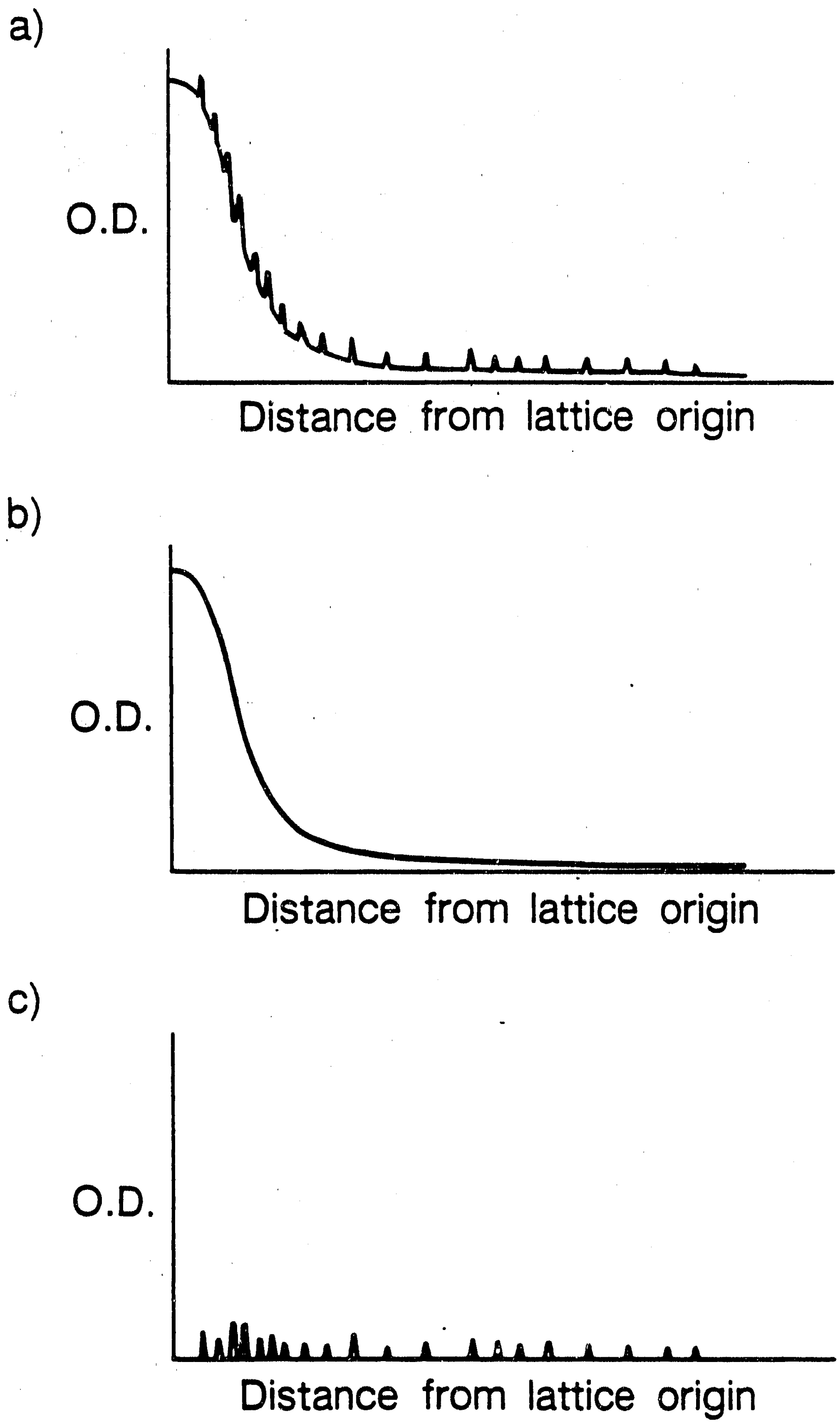
a)
O.D.
Distance from lattice origin
b)
O.D.
Distance from lattice origin
c)
O.D.
Distance from lattice origin

XBL 897-5130

2.3.3 Spot integration

The next phase of diffraction processing is the calculation of the total integrated intensity for each diffraction spot in the pattern. When indexing the patterns, as described earlier, one determines the pattern center and the x and y components of the lattice unit vectors. These parameters are input into the diffraction pattern processing software and are used to predict the coordinates of each spot in the array. In the algorithm used to determine these positions, adjustments are made for the compensation of Ewald sphere curvature and microscope distortions such as pincushion, barrel and spiral. The user of this software must also specify the size (in pixels) of the spot integration boxes to be placed around the predicted spot centers. Pixels falling within these boxes are converted from optical density to electron exposure. Following this they are corrected for the radial background noise described earlier as well as for any drifts in the pattern's "baseline" optical density. A final correction is made to these pixels to compensate for local background deviations. In this treatment, one specifies the size and orientation of background sampling boxes to be placed in the areas surrounding the diffraction spots in the pattern to be analyzed. For each spot in the pattern a local background value is calculated and subtracted from each pixel in the corresponding diffraction spot box.

The background corrected pixels within each diffraction spot box are added up and a total intensity determined for that spot. A center of gravity of that spot is also determined and compared with the position predicted by the user-provided lattice parameters. An array of differences (errors) from predicted to actual spot centers are stored and used to refine the lattice parameters utilizing a least squares minimization algorithm. The program can be set to continue to refine the lattice parameters for a user defined number of cycles or until convergence criteria are met.

Once the lattice has been "best fit" the diffraction spot integrated intensities can be organized for output. First each diffraction spot is reviewed to determine if the individual pixels comprising it all fall within a minimum and maximum intensity range. If not, that diffraction spot is omitted from the final output. The spots remaining are then sorted into Friedel related (h,k;-h,-k) pairs to determine the averages and differences of the Friedel related spot intensities. Unpaired spots are rejected at this time. The remaining test is a two parameter check of the relatedness of the Friedel pair intensities. If the difference in intensity between the spot pairs is less than some multiple (user defined) of their average and if that difference is less than another user defined constant, the pair average intensity is considered reliable for output. All of the spot intensity analysis is done in an effort to minimize the number of false diffraction spot reports due to such factors as film imperfections, scratches and foreign material falling on the plate during densitometry. The qualifying data is then written to disk in a format suitable to be combined with other processed diffraction patterns into a three dimensional data set.

2.3.4 Merging and fitting of diffraction intensities

With the use of the previously described "software" the user will now have a collection of files, each containing the H,K indices , Friedel pair averages and differences of a particular diffraction pattern. For each plate or pattern processed, the user will also have determined a tilt axis and tilt angle. With this data the goal is to sort and organize the lot of diffraction spot intensities into a three dimensional data set comprised of reconstructed lattice rods. This is accomplished by determining the three dimensional vector $(h,k,z*)$ for each spot based on the set of two dimensional vectors (h,k), and the appropriate tilt angles and tilt axes. Once properly oriented, the spots can be scaled or normalized to an untilted reference set of diffraction intensities.

The sets of intensity measurements organized into lattice rods are now in a position to be fitted by a smooth curve. Each group of points comprising a single lattice rod is fitted to a series of damped sinc functions of the form

$$I(z^*) = \sum_{i=-n}^{n} A_i \left[\frac{\sin 2\pi d(z^* - i/2d)}{2\pi d\,(z^* - i/2d)} \right] e^{-1/2\,B\cdot\,(z^* - i/2d)^2}$$

Equation 2

where the coefficients (Ai) of each term are determined so as to produce the smallest mean squared difference between the data and the smooth curve. A membrane thickness of 50 A was supplied for d and a value of 100 was used for the damping factor B. Once the first generation of curves are generated , the patterns used to initially create the composite lattice rods can be remerged to the new curves. This provides the opportunity for curve refinement. In addition to the aforementioned normalization scaling, the diffraction spot intensities can now be adjusted for temperature factor components parallel and perpendicular to the plane of the membrane. The tilt axis and angle of each plate/pattern included in the reciprocal lattice reconstruction can also be redetermined so as to provide a best fit to the curves. This scenario of merging and curve fitting can be repeated as more plates are incorporated into the data base as well as for minimizing the R factors of those plates already in it. The final curves are then sampled at a fine interval (typically the reciprocal of 5 times the membrane thickness), and these values are combined with similarly sampled phase data to generate a hybrid three-dimensional structure factor data set.

Section III

RESULTS

3.1 Microscope Calibration

An important element in the effective processing of electron diffraction patterns is the compensation or correction for microscope distortions of recorded diffraction patterns. These distortions fall into two categories, those with a resolution cubed dependency such as pincushion, barrel and spiral distortions, and those independent of resolution such as ellipticity of magnification.

Although their apparent visual effects are different, the various forms of resolution cubed dependent distortions can all be described in terms of radial and azimuthal or angular components. The contribution to distortions of diffraction patterns recorded on our microscope from these factors was determined by comparing predicted diffraction spot centers with those measured. For this purpose we used patterns collected from untilted two-dimensional crystals of bacteriorhodopsin. Differences between the predicted and actual spot centers were broken into radial and azimuthal components. Radial and azimuthal differences were then separately plotted versus resolution for analysis. (see figures 12 and 13)

Figure 12. Error in the prediction of the location of diffraction spot centers of gravity; radial component. Graphs such as these are useful in determining if resolution-cubed dependent distortions have been introduced into the diffraction patterns by the microscope.

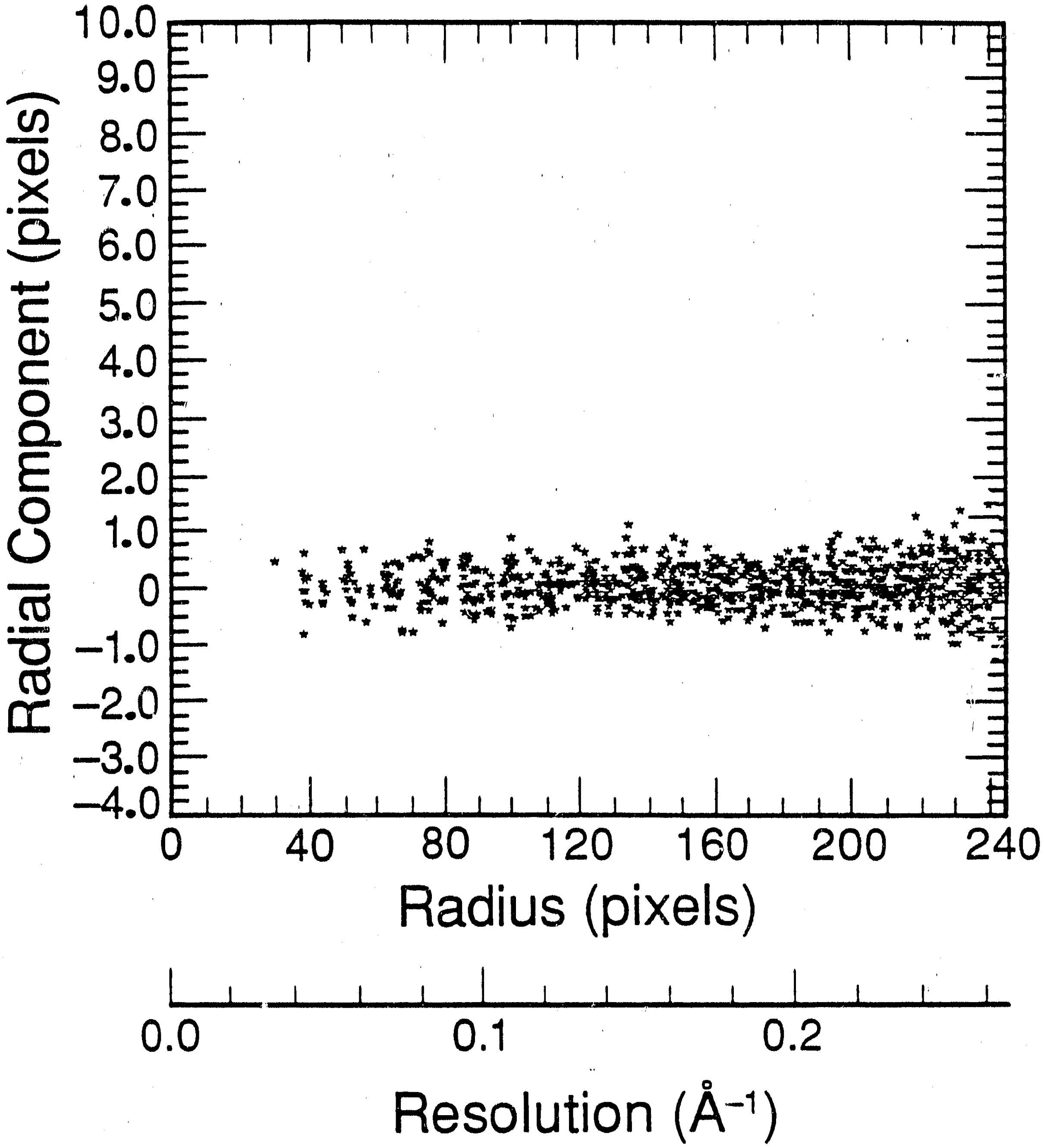
Radial Component (pixels)
10.0
9.0
8.0
7.0
6.0
5.0
4.0
3.0
2.0
1.0
0
−1.0
−2.0
−3.0
−4.0
0
40
80
120
160
200
240
Radius (pixels)
0.0
0.1
0.2
Resolution (Å^{-1})

XBL 899-5213

Figure 13. Error in the prediction of the location of diffraction spot centers of gravity; azimuthal component.

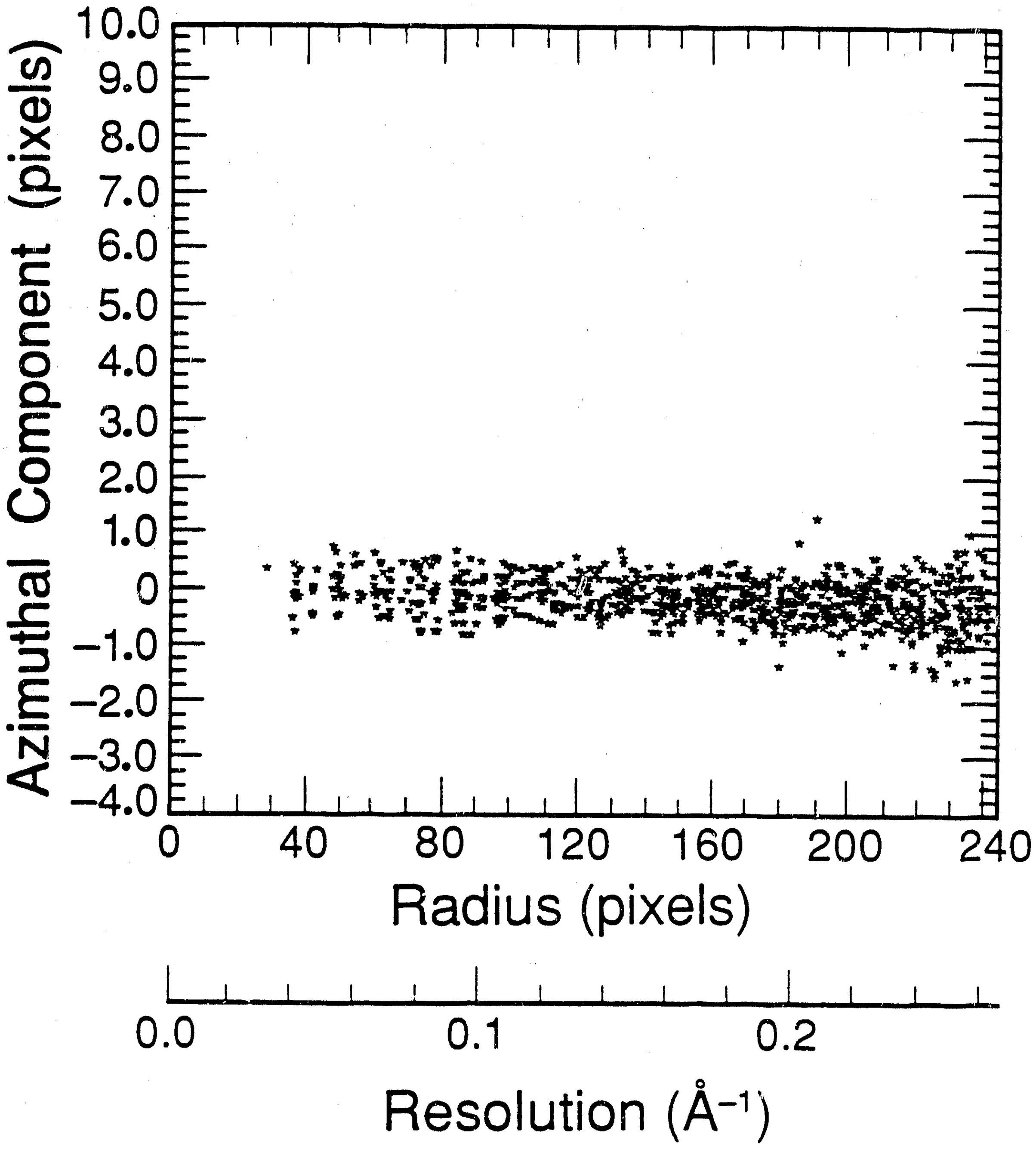
Azimuthal Component (pixels)
10.0
9.0
8.0
7.0
6.0
5.0
4.0
3.0
2.0
1.0
0
−1.0
−2.0
−3.0
−4.0
0
40
80
120
160
200
240
Radius (pixels)
0.0
0.1
0.2
Resolution (Å⁻¹)

XBL 899-5214

From plots such as these it was concluded that, in our microscope under specific diffraction mode conditions, resolution cubed dependent distortions were insignificant. Therefore, software adjustment parameters for these distortions were set to zero.

Distortions in electron diffraction patterns arising from microscope ellipticity of magnification affect the calculation of tilt angles and axes. As mentioned in section I B, the tilt angle and axis of a tilted pattern are determined from the geometric relationship between unit vectors of the tilted and an untilted reference lattice. It is apparent then, that any distortions to the true lengths of the unit vectors of a tilted diffraction pattern, due to a microscope's ellipticity of magnification, will cause errors in the calculated tilt angle and axis. For the proper calculation of tilt angle and axis then, we need to restore the lattice unit vectors to their proper lengths. A method for correcting these distortions is again provided in the diffraction pattern processing software. The user is required to provide the angle that the minor axis of the magnification ellipse makes with the horizontal and the ratio of the minor to major axis lengths. Dr. Kenneth Downing has determined these parameters, based on measurements of powder pattern diffraction of gold coated carbon films, to be 22.4 degrees for the minor axis angle and 0.9822 for the minor to major axis ratio.

3.2 Collected Data

The 2-D crystals of PhoE porin were surveyed and diffraction patterns recorded at fixed tilt angles of 0, 30, 45, and 60 degrees. When care was taken to ensure minimal bending of the electron microscope grid, subsequently confirmed tilt angles came to within +/- 5 degrees of the holder's fixed angle.

As described earlier in the Methods section, over the course of refining the specimen embedment protocol, we tested and evaluated three different sugars, aurothicglucose (ATG), glucose and trehalose. ATG was the first embedment sugar we tried. Figures 14 through 16 are representative diffraction patterns of 0, 30 and 60 degree tilted specimens respectively. Two undesirable conditions are apparent in these patterns. Resolution is limited; the untilted pattern contains reflections out to approximately 7 A, the 30 degree pattern has reflections out to about 10 A, and the 60 degree pattern yields detectable spots to a resolution of only 15 A. The second unfavorable condition, related to the cause of the first, is the broadening of diffraction spots with increasing resolution. We were unsuccessful in our attempts to

Figure 14. Electron diffraction pattern from two-dimensional crystals of PhoE porin embedded in autothioglucose (ATG) recorded at a specimen tilt angle of 0 degree.

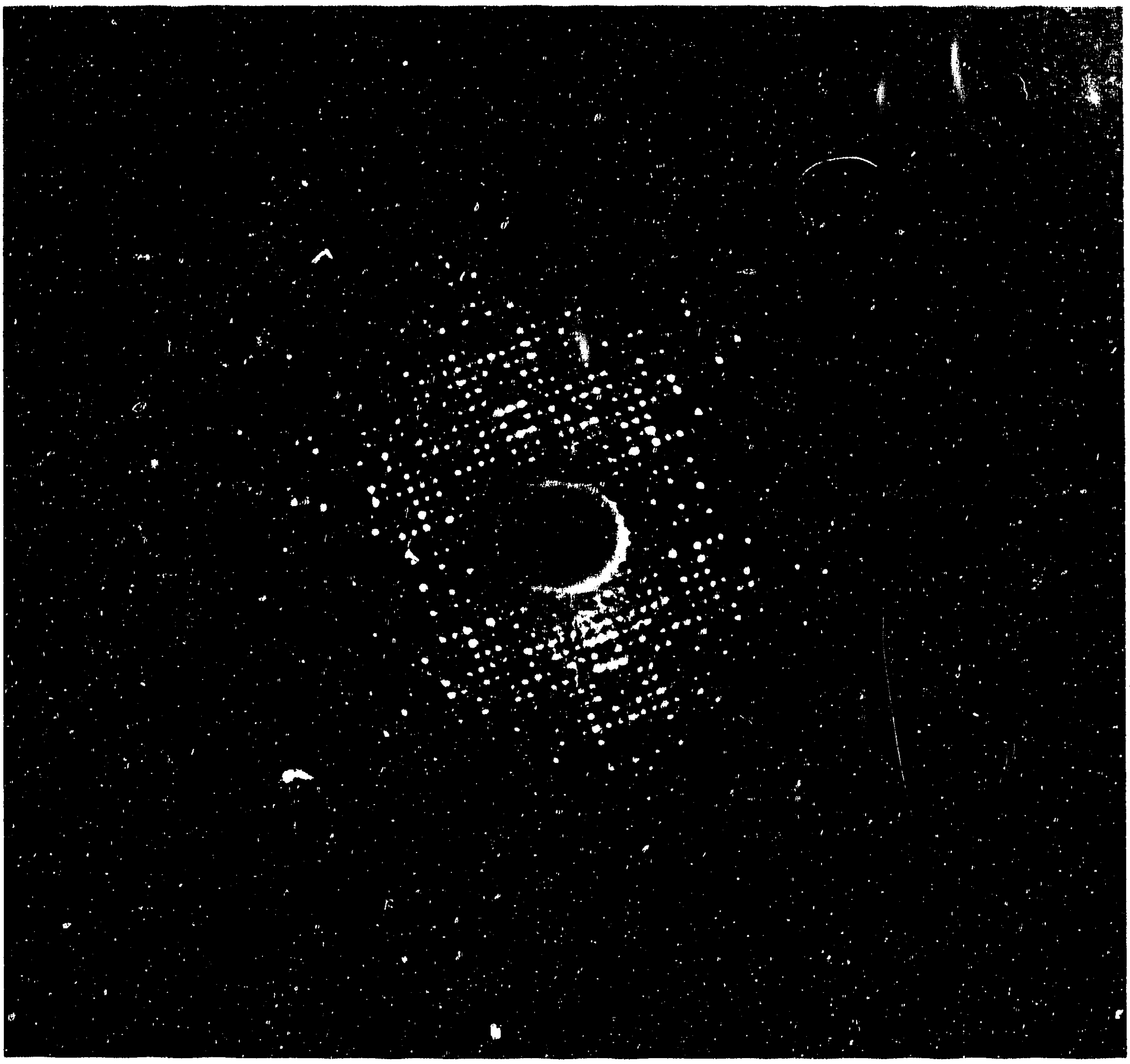

XBB 897-5715

Figure 15. Electron diffraction pattern from two-dimensional crystals of PhoE porin embedded in ATG recorded at a specimen tilt angle of 30 degrees.

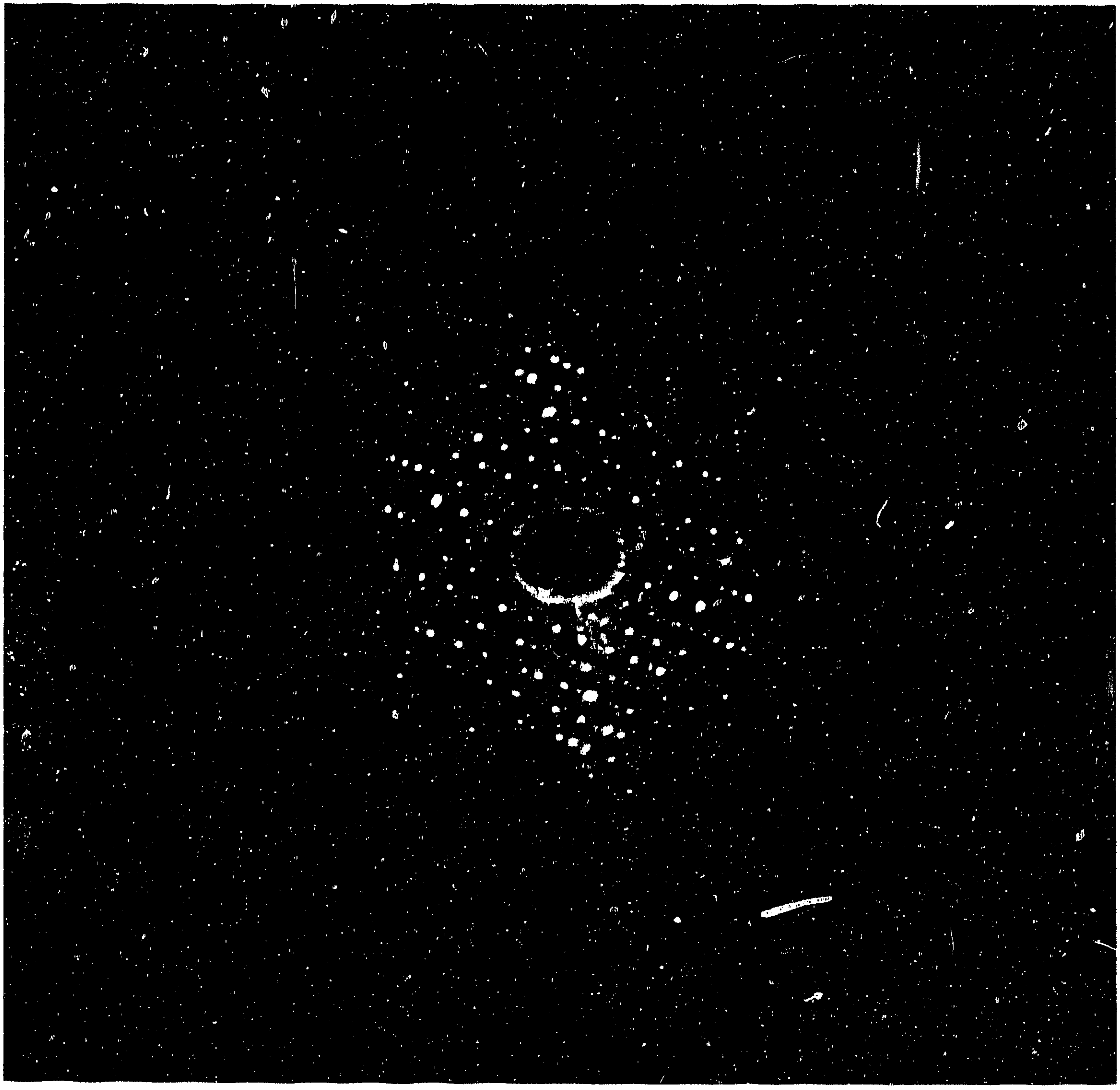

XBB 897-5720

Figure 16. Electron diffraction pattern from two-dimensional crystals of PhoE porin embedded in ATG recorded at a specimen tilt angle of 60 degrees.

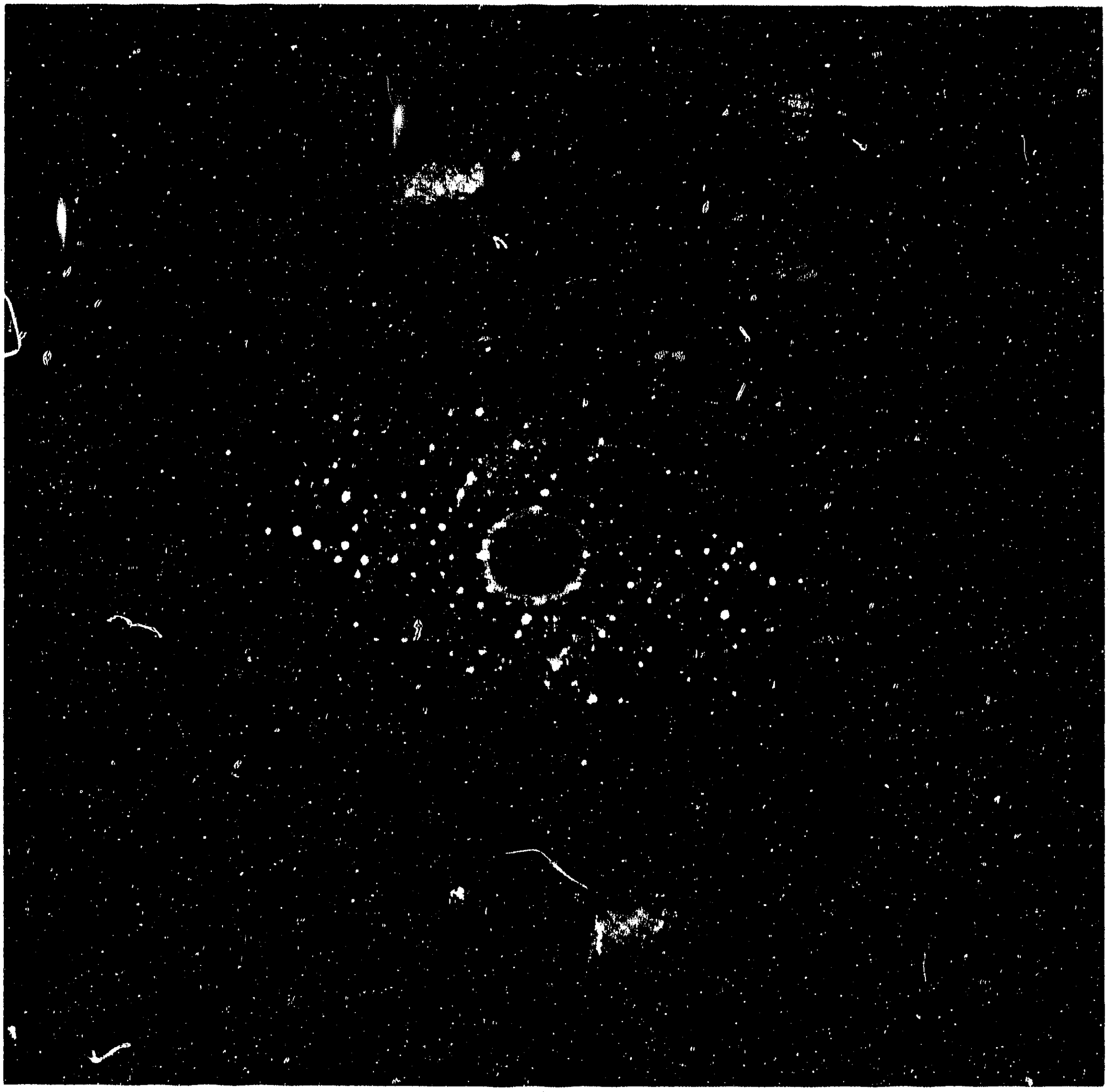

XBB 897-5717

significantly improve diffraction spot sharpness and the resolution of patterns obtained from specimens embedded in ATG.

Following our experience with ATG we studied PhoE porin embedded in glucose. It was readily apparent that PhoE specimen embedment in glucose yielded results superior to what we obtained in ATG. Diffraction patterns representative of our best results obtained from specimens in glucose and at tilts of 0, 30 and 60 degrees are shown in Figures 17 through 19 respectively. Although the resolution limit and sharpness of diffraction spots was improved, we desired greater sharpness of diffraction spots located perpendicular to the tilt axes in our patterns. This desire for even greater spot sharpness was driven by our goal to have off- axis spots as sharp as those along the tilt axis, an indication of exceptional specimen flatness. Successful imaging of tilted specimens able to yield high resolution phase information requires specimen flatness of this degree. One additional goal was to increase the yield of high-quality patterns obtained per microscope session.

We therefore continued to experiment with different embedment procedures and eventually settled upon trehalose as our embedment sugar of choice. Diffraction studies of PhoE in trehalose consistently yielded patterns with sharp

Figure 17. Electron diffraction pattern from two-dimensional crystals of PhoE porin embedded in glucose recorded at a specimen tilt angle of 0 degrees.

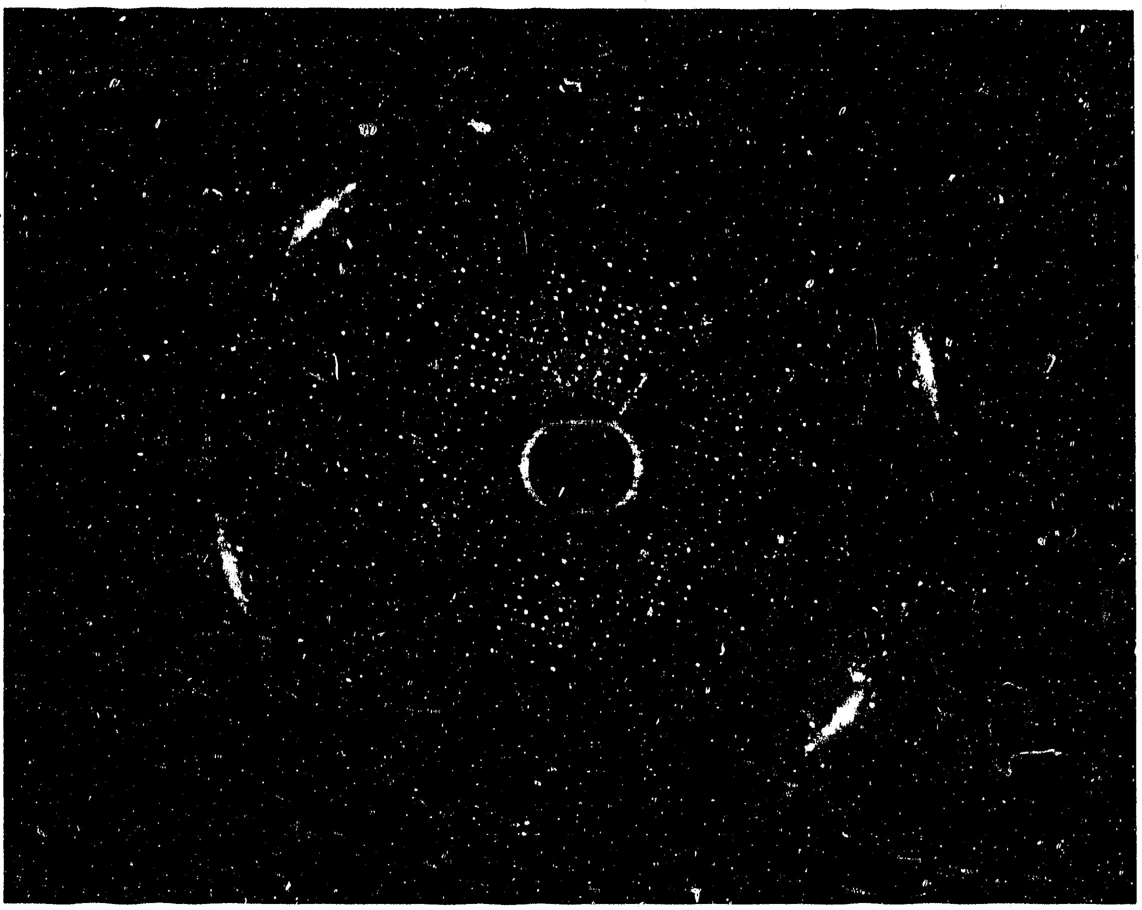

XBB 897-5716

Figure 18. Electron diffraction pattern from two-dimensional crystals of PhoE porin embedded in glucose recorded at a specimen tilt angle of 30 degrees.

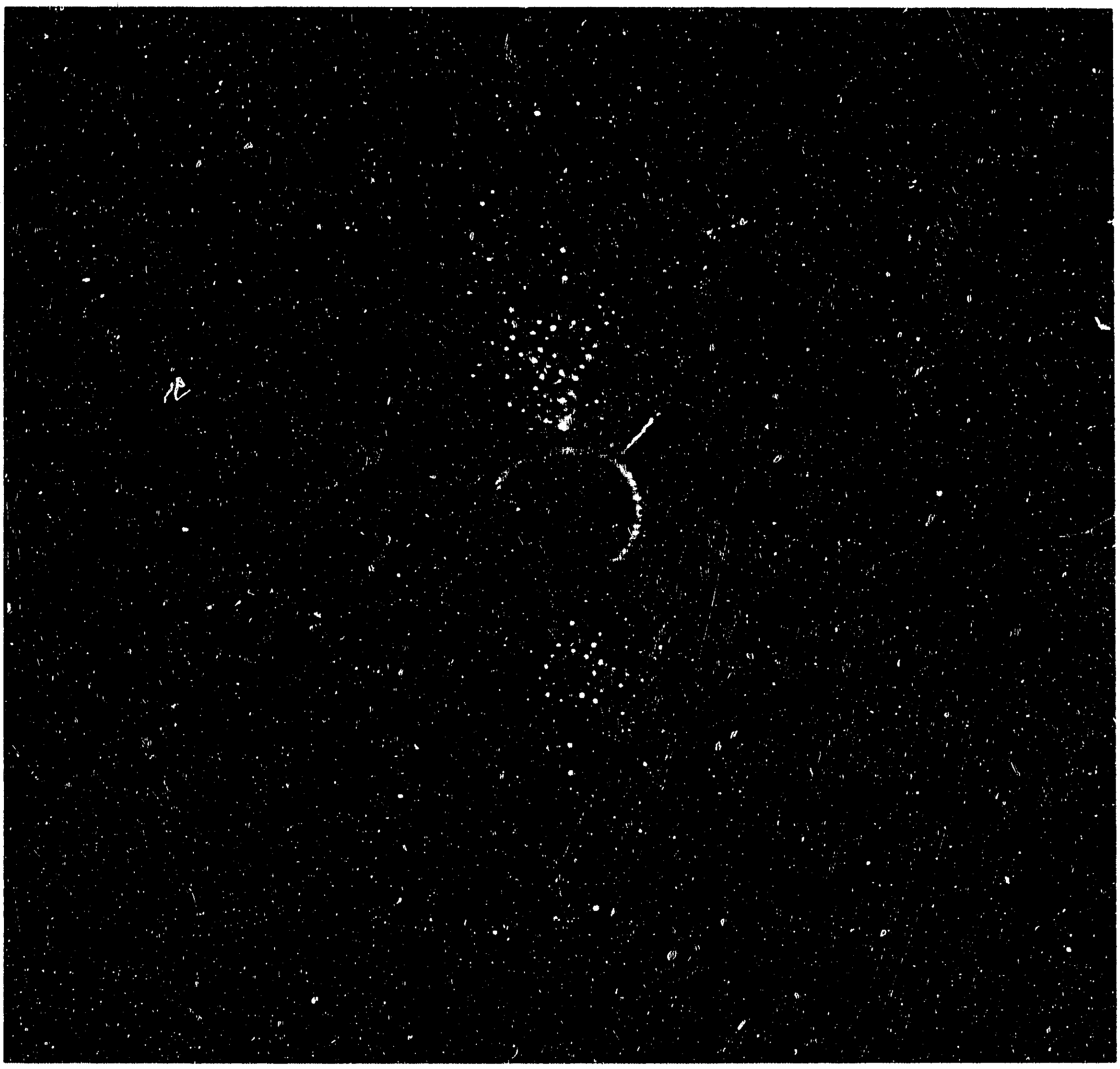

XBB 897-5718

Figure 19. Electron diffraction pattern from two-dimensional crystals of PhoE porin embedded in glucose recorded at a specimen tilt angle of 60 degrees.

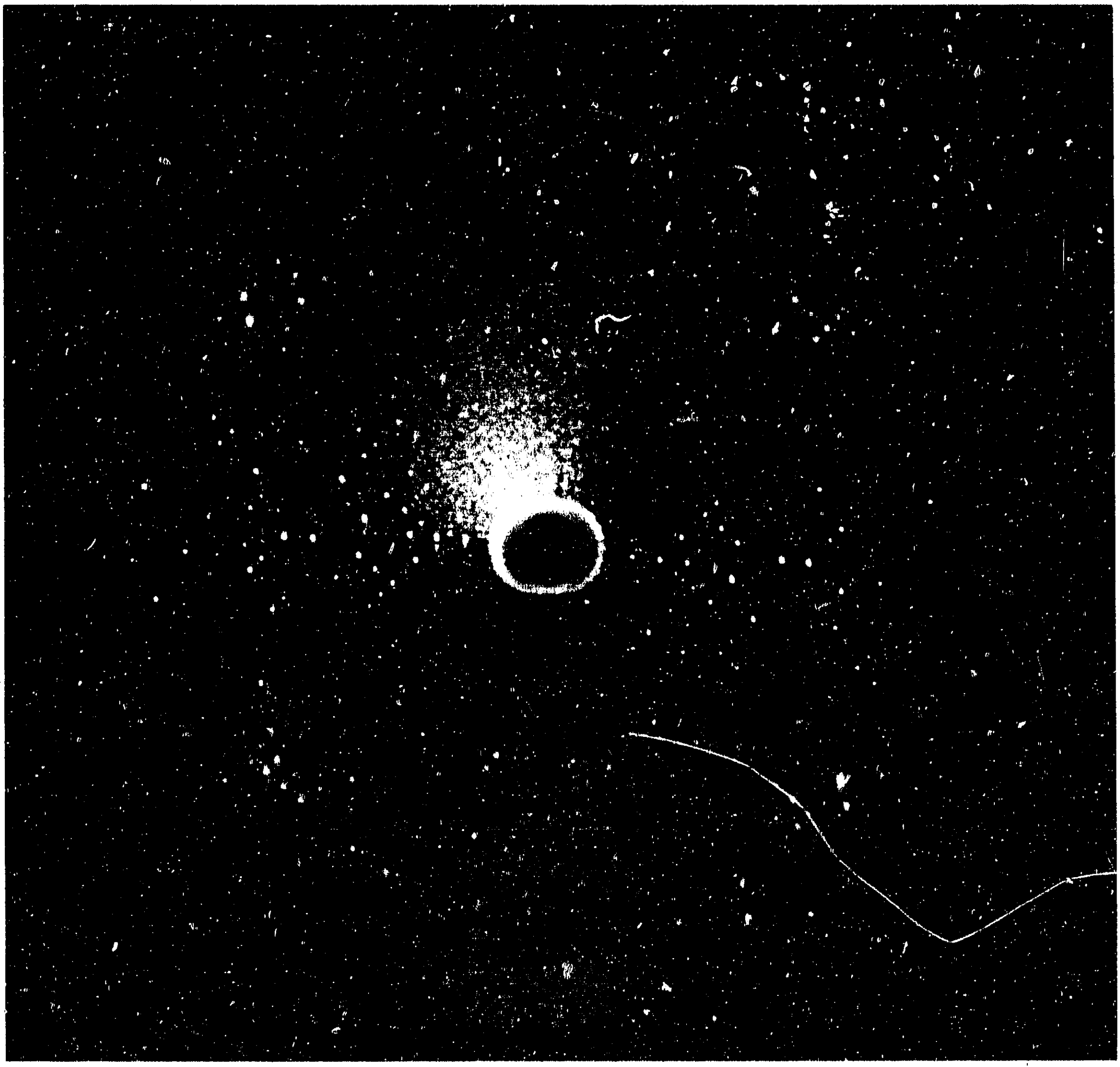

XBB 897-5719

diffraction spots extending to high resolution (greater than 3.5 A) even for specimens tilted to 60 degrees. We also realized a dramatic increase in our success rate for obtaining high-quality diffraction patterns. While providing diffraction data ideal for determining PhoE lattice rod intensities, the trehalose embedment protocol also provides specimens especially suited for high resolution phase determination from images. Examples of diffraction from samples in trehalose at 0, 30, 45 and 60 degrees tilt are shown in Figures 20 through 23 respectively. These patterns are representative of the best of the diffraction patterns collected, having essentially isotropically sharp spots. More than half of the plates in the data set are of this quality. The remaining patterns did not contain isotropically sharp spots but had off-axis spots with broadenings no greater than one fourth of the spots' center-to-center distances. For microscope sessions involving really good specimen preparations, one usable film was recorded for every two or three exposed.

Figure 20. Electron diffraction pattern from two-dimensional crystals of PhoE porin embedded in trehalose recorded at a specimen tilt angle of 0 degrees.

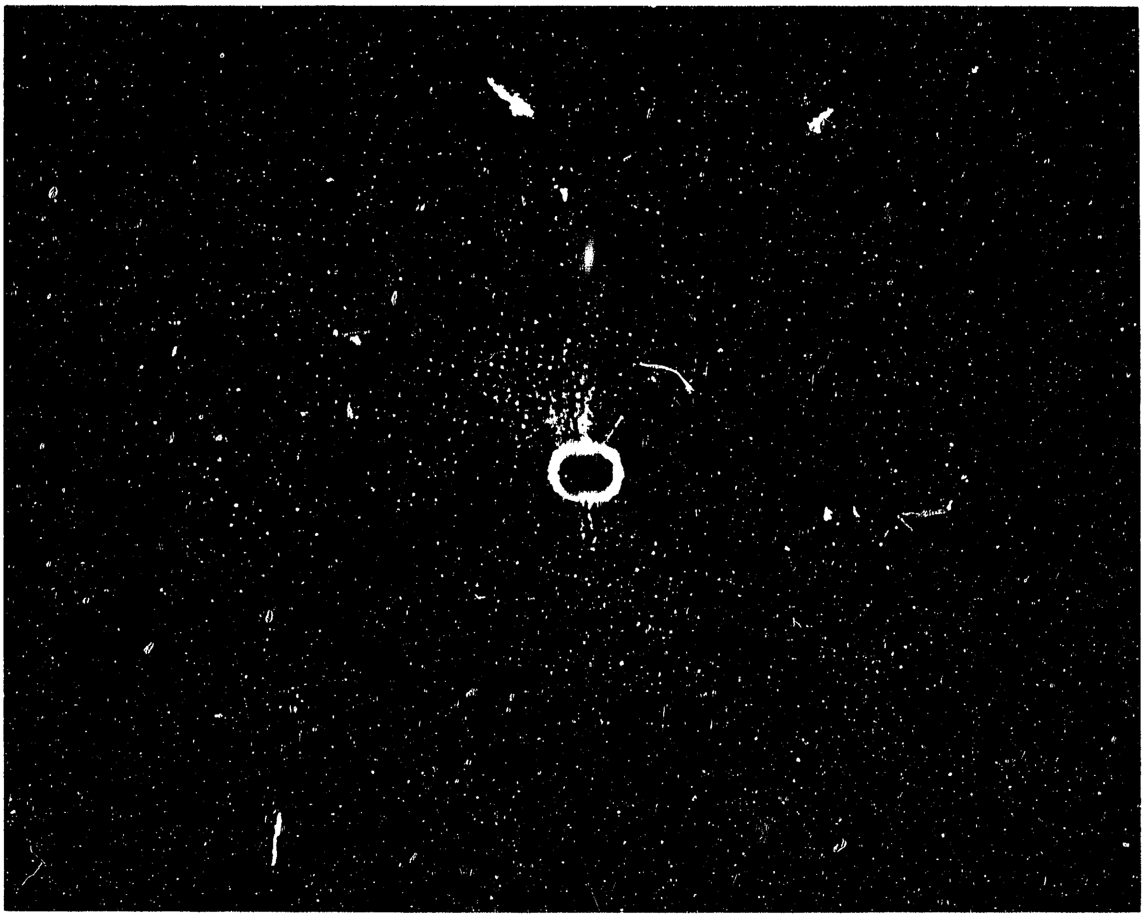

XBB 893-1465

Figure 21. Electron diffraction pattern from two-dimensional crystals of PhoE porin embedded in trehalose recorded at a specimen tilt angle of 30 degrees.

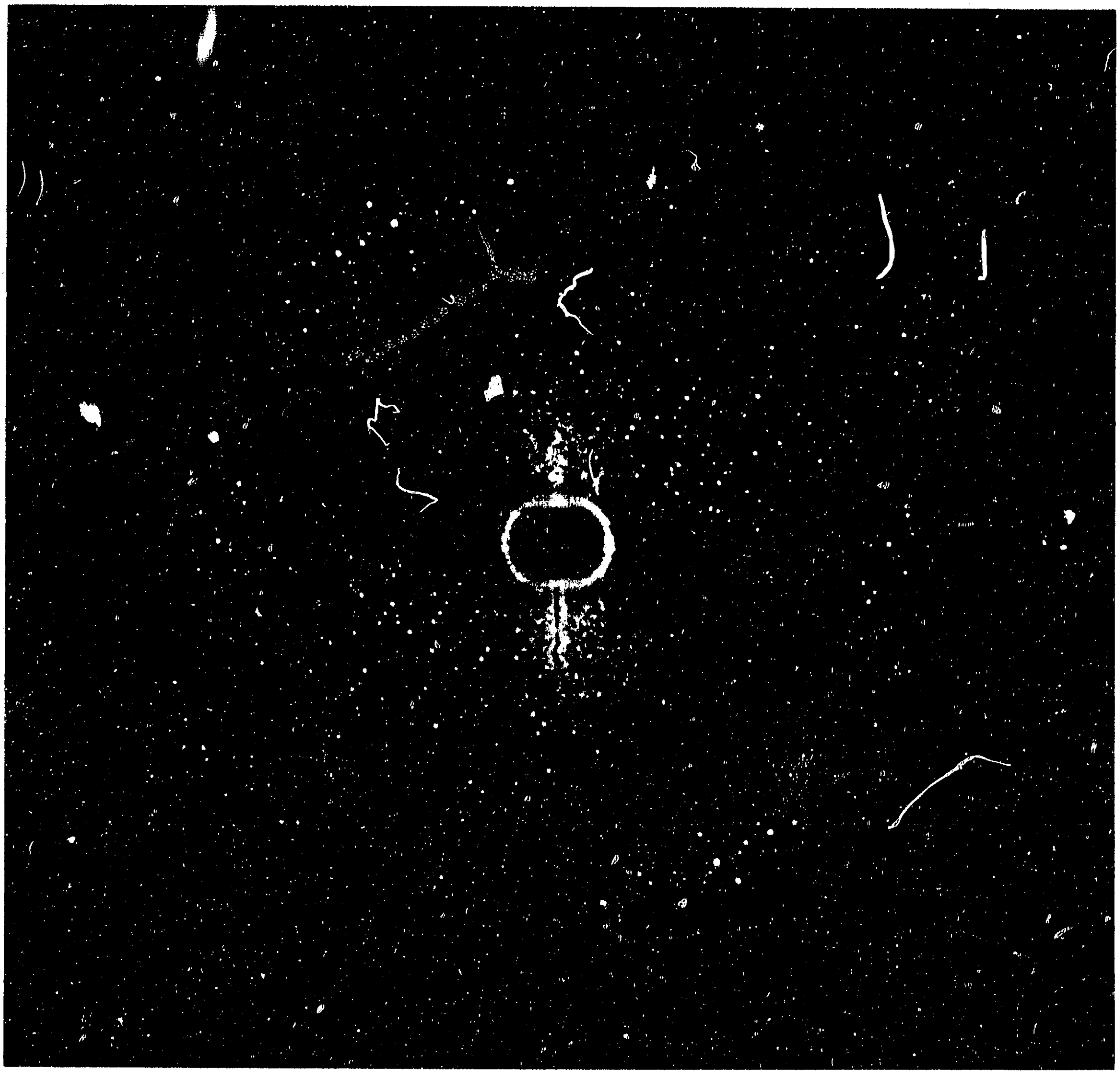

XBB 897-5710

Figure 22. Electron diffraction pattern from two-dimensional crystals of PhoE porin embedded in trehalose recorded at a specimen tilt angle of 45 degrees.

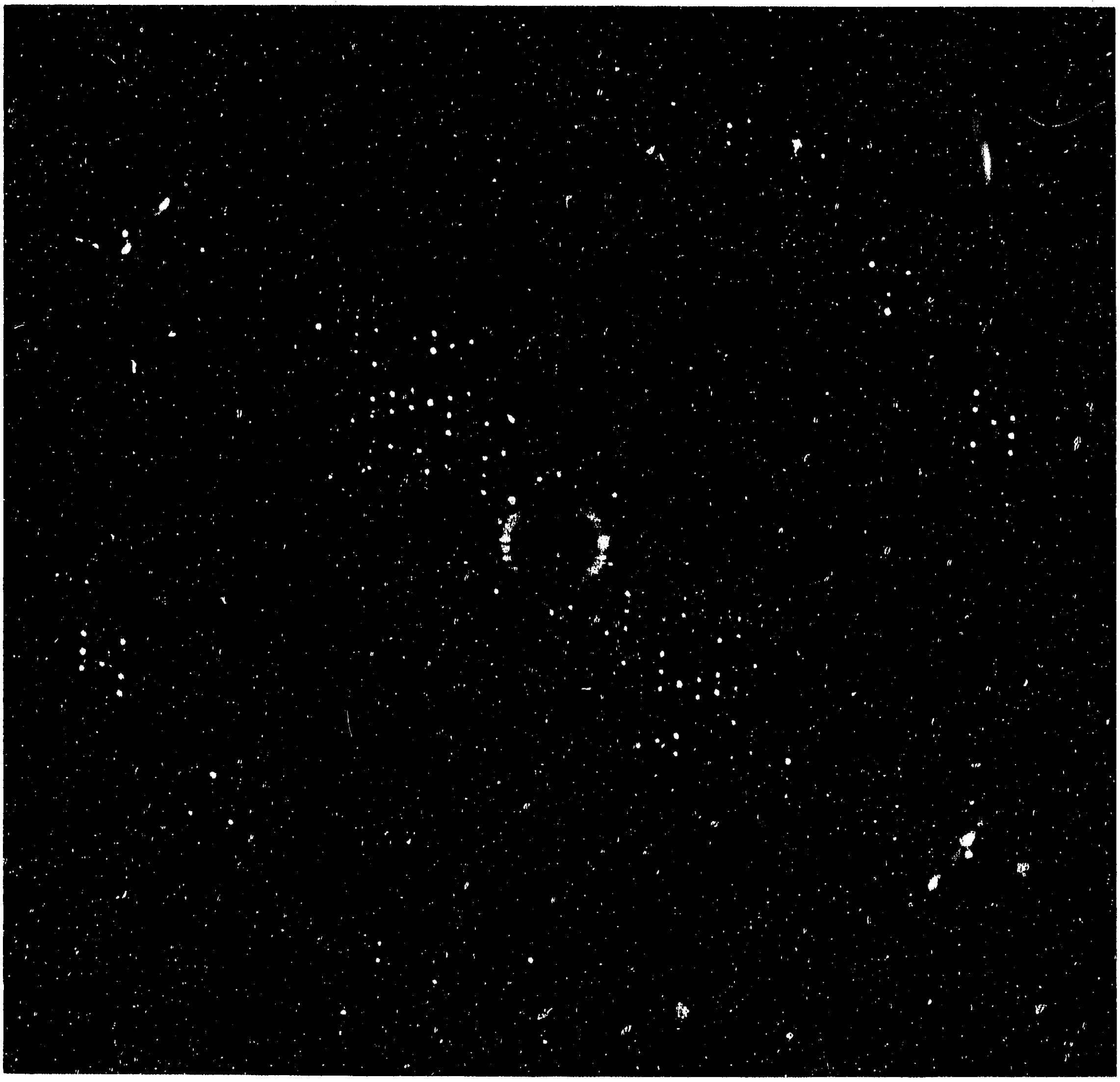

XBB 897-5711

Figure 23. Electron diffraction pattern from two-dimensional crystals of PhoE porin embedded in trehalose recorded at a specimen tilt angle of 60 degrees.

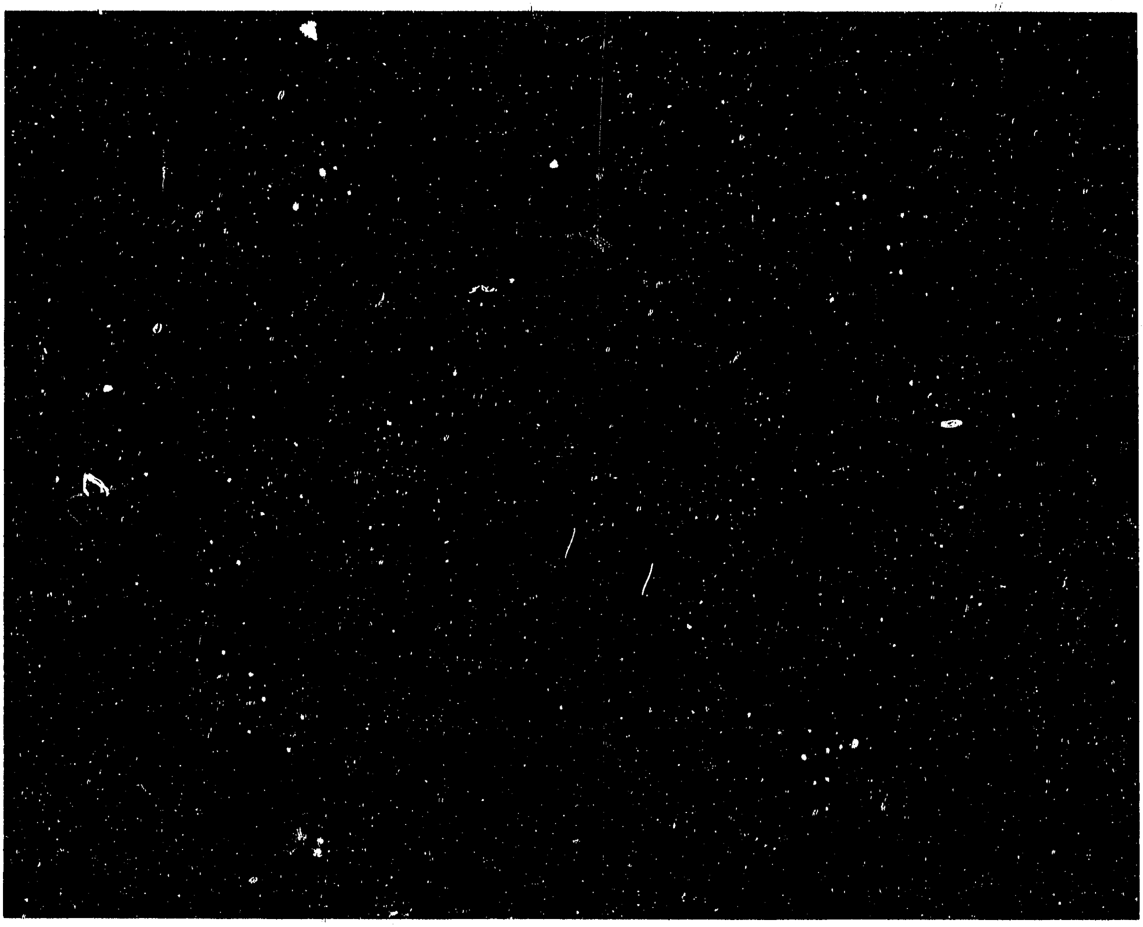

XBB 893-1464

3.3 Processing of Diffraction Patterns

Initial processing of diffraction patterns consisted of indexing the pattern's reciprocal lattice (using the computer program AEDDSP) and removing the radially distributed noise due to inelastically scattered electrons (using the computer program BACK). Following this, a computer program (PICKYCOR) enabling one to integrate pixelized diffraction spot intensities was applied to each plate. Part of this procedure included the removal of residual background noise remaining after the initial radial background subtraction. An intensity adjustment value for the removal of this residual background is determined for each spot individually and is based on the distribution of noise in the area immediately surrounding each diffraction spot. A typical example of a diffraction pattern's residual background and its standard deviation is given in Figures 24 and 25 respectively. A nominal value for the average local background in our plates is about 0 while a value of 300 is typical for its standard deviation.

After adjustments are made for the effect of local background noise, Friedel symmetry-related diffraction spot intensities are evaluated. For every symmetry-related pair an intensity average and difference is calculated. Only those pairs for which the intensity difference is not greater than their average nor greater than a user-defined

Figure 24. Average residual background intensities after subtraction of radial background. Intensities are in arbitrary units and are based on a linearized optical density scale.

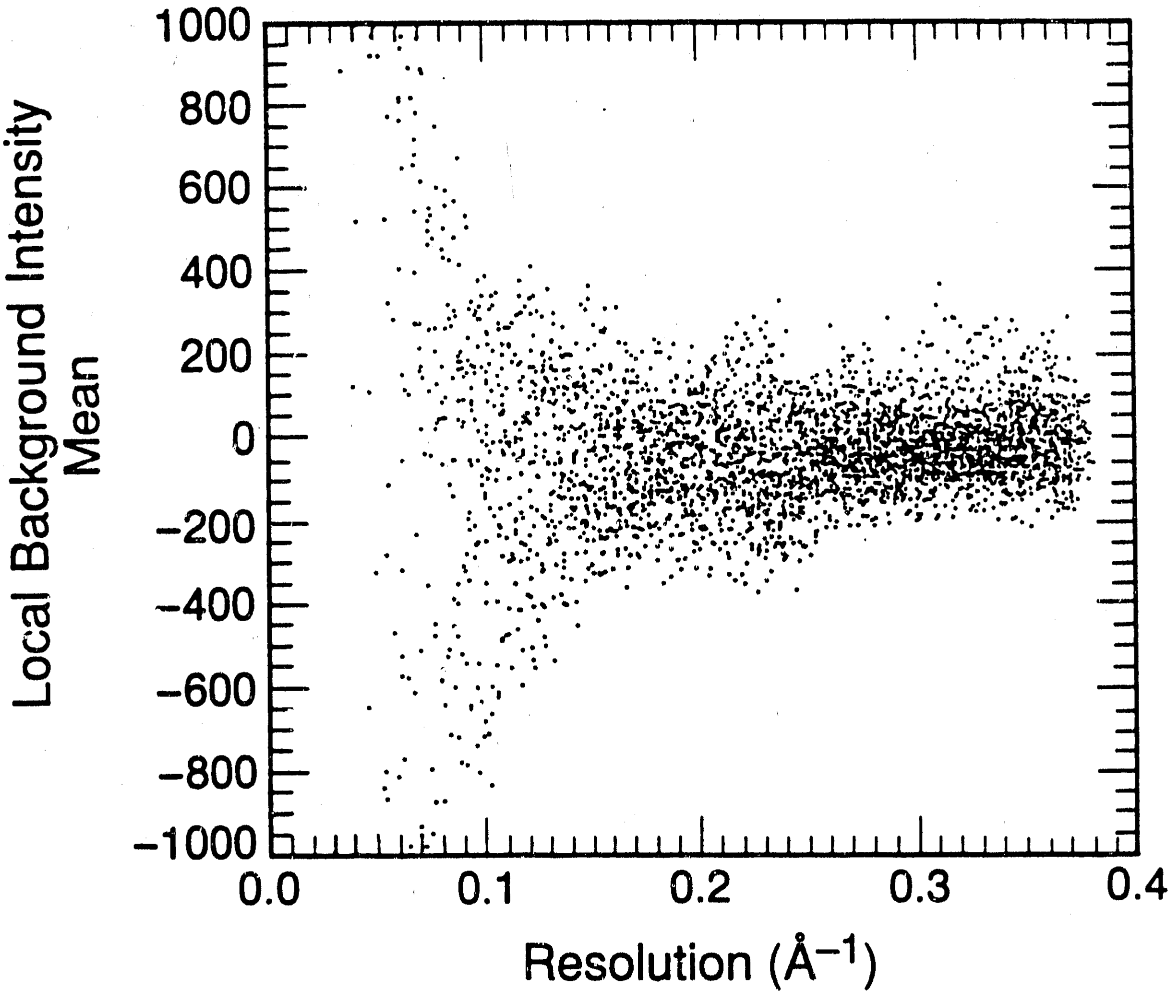
1000
800
600
400
200
0
−200
−400
−600
−800
−1000
Local Background Intensity
Mean
0.0
0.1
0.2
0.3
0.4
Resolution (Å^{-1})

XBL 899-5210

Figure 25. Standard deviation of residual background after subtraction of radial background. Intensities are in arbitrary units and are based on a linearized optical density scale.

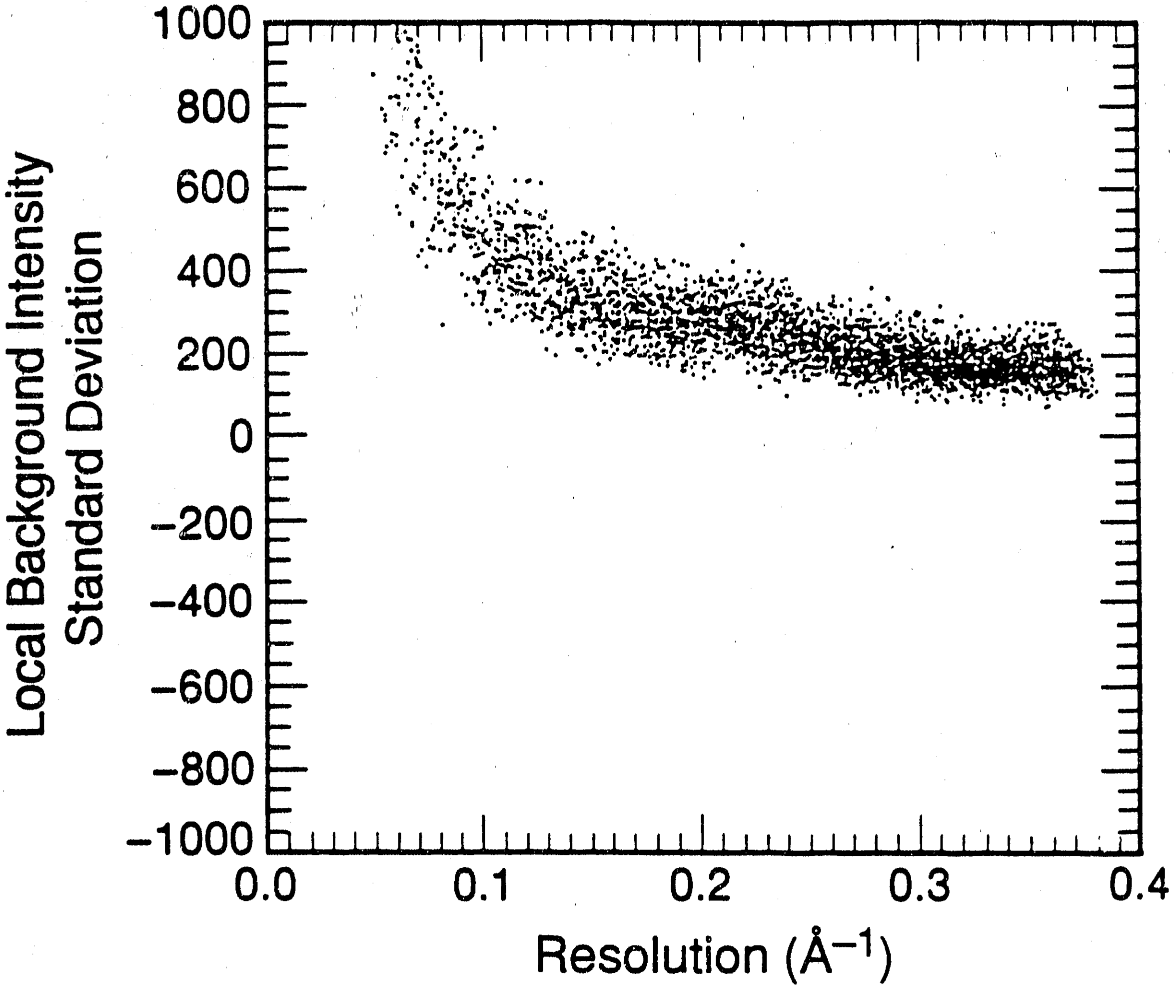
Local Background Intensity
Standard Deviation
1000
800
600
400
200
0
−200
−400
−600
−800
−1000
0.0
0.1
0.2
0.3
0.4
Resolution ($\AA^{-1}$)

XBL 899-5211

threshold are included in the final intensity output list. This test is used to reject those spots with questionable intensities due to scratches or foreign matter on the scanned film. The threshold used in our data processing was 1100 and was determined empirically from plots depicting the frequency of occurrence of Friedel pair intensity differences. Examples of these plots for an untilted sample is given in Figure 26 and for a sample tilted 30 degrees in Figure 27.

For a given diffraction pattern, sums of the intensity averages and differences of Friedel symmetry related spots passing the rejection criteria are used to calculate a Friedel symmetry R-factor (Rsym) (Equation 3).

$$R_{sym} = \frac{\sum_{H,K} \left| I_{H,K} - I_{-H,-K} \right|}{\sum_{H,K} 1/2 \left(I_{H,K} + I_{-H,-K} \right)}$$

equation 3

This Rsym factor is used as a quality checking parameter to assess the "goodness" of diffraction patterns and the performance of the processing software. In our PhoE data set a significant fraction of diffraction spots have relatively low intensity. Greater than 90 percent of the reflections in the PhoE data set have an intensity above the mean background that is less than or equal to one noise

Figure 26. Histogram of the differences in the intensities of Friedel symmetry related diffraction spots from the diffraction pattern of an untilted specimen. Bin widths of 100 intensity units have been used.

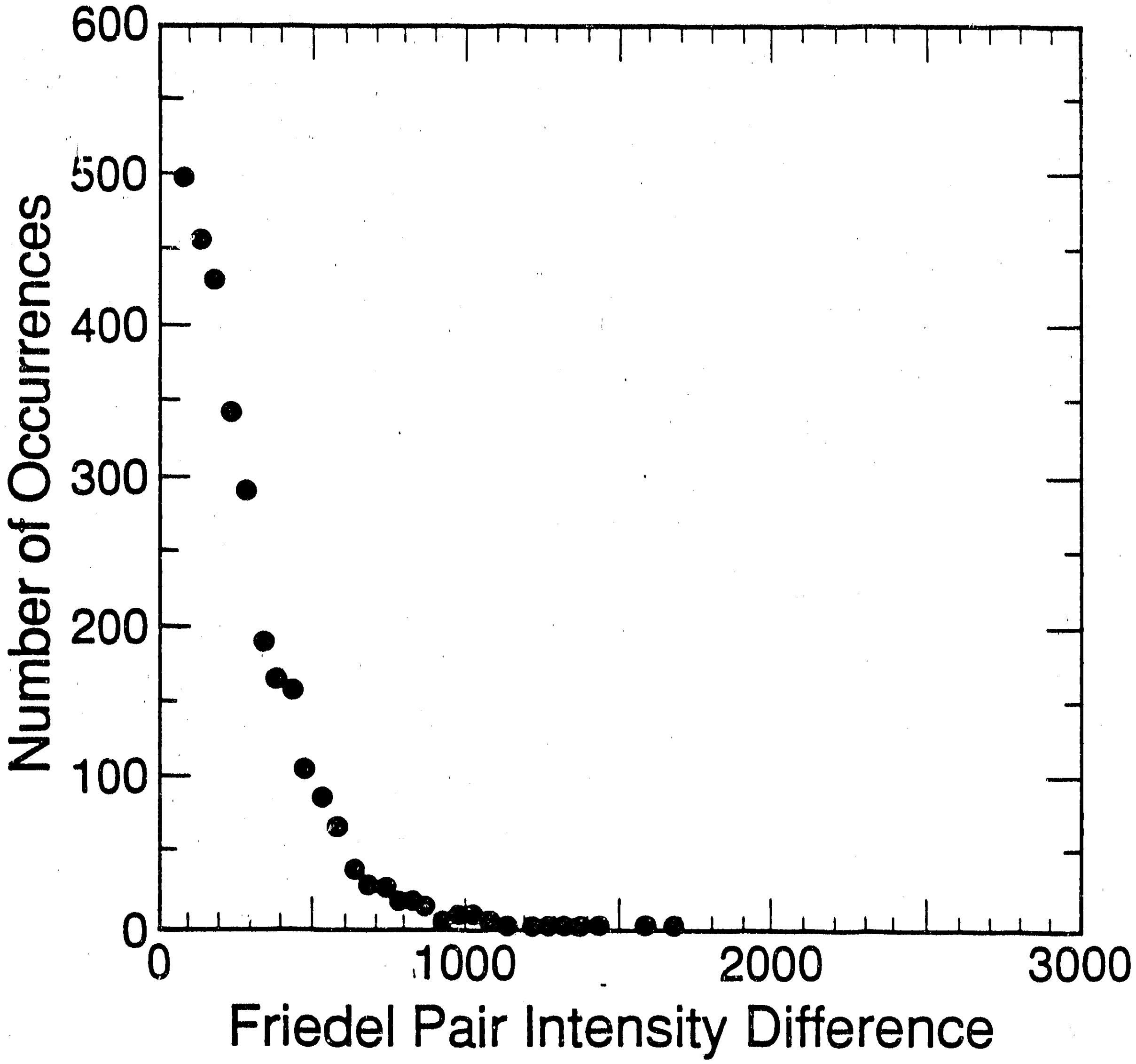
600
500
400
300
200
100
0
0
1000
2000
3000
Number of Occurrences
Friedel Pair Intensity Difference

XBL 897-5166

Figure 27. Histogram of the differences in the intensities of Friedel symmetry related diffraction spots from the diffraction pattern of a specimen tilted 30 degrees. Bin widths of 100 intensity units have been used.

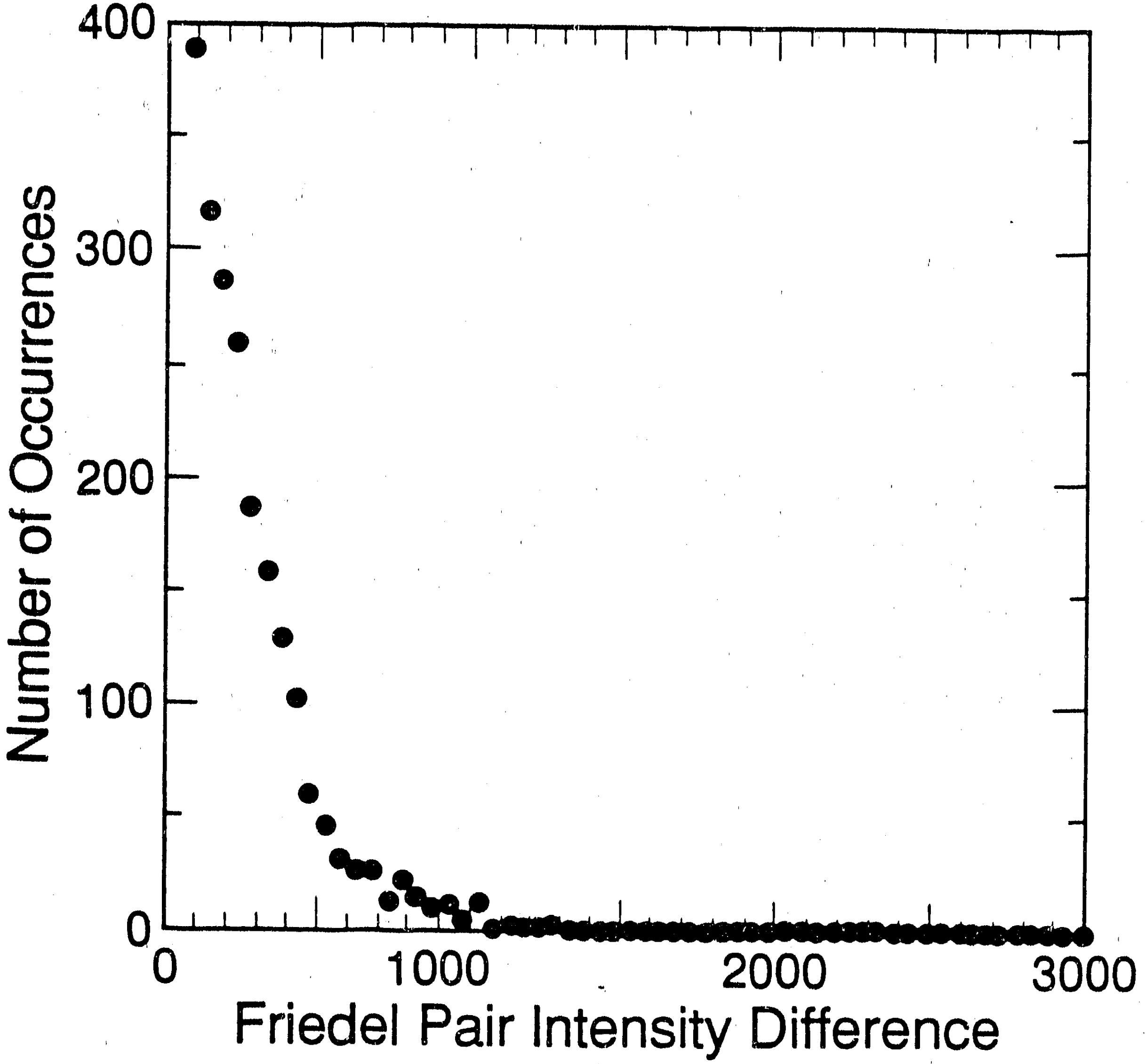
400
300
200
100
0
Number of Occurrences
0
1000
2000
3000
Friedel Pair Intensity Difference

XBL 897-5167

standard deviation. Due to the nature of equation 3, a high percentage of very low intensity spots can tend to increase the size of a pattern's global Rsym. If one calculates the Rsym for those spots with intensity averages greater than one noise standard deviation over background, one obtains Rsym values that are signifcantly smaller.

Examples of Rsym factors, determined by considering all reflections and only those above one noise standard deviation plus mean background, are listed for a few sample plates in Table 3.

TABLE 3

Examples of Diffraction Pattern Rsym Values

Plate	Specimen	Rsym	
Number	Tilt Angle	All Points	Spots > 1 Std.Dev.
9170	0	0.27	0.10
7584	30	0.49	0.15
7697	30	0.40	0.16
0223	45	0.40	0.15
0006	45	0.26	0.12
8854	60	0.41	0.19
8629	60	0.31	0.18

The plates from 30, 45 and 60 degree tilted specimens listed here are representative of the worst and best obtained for each of these tilt groups. The plate from the untilted specimen is the best within that group although all the plates from this group are of similar quality.

3.4 Pattern Merging and Intensity Curve Fitting

When ready for this last phase of data processing, each diffraction pattern will have been reduced to a list of integrated spot intensities. More specifically, the files to be merged will contain the Miller indices of the combined Friedel pairs as well as their corresponding average intensities and intensity differences. The intensity differences will be used to determine the length of the error bars appearing on graphs where curves are fitted to the measured intensities for each lattice rod. During the processing of diffraction patterns to generate these files a corresponding specimen tilt axis and angle were calculated. With the diffraction spot files and their corresponding tilt angles and axes to fix the patterns' positions in space, the intensities can be merged to form a 3-D set of intensity lattice rods.

The Fourier transform of a 2-D crystal will generate a continuum of intensities and phases along the length of the lattice rods. For transforms of such crystals which have been sampled via a finite number of tilted specimen diffraction patterns, the lattice rods obtained from data merging are not lines of continuous data but "chains" of discrete values. In order to obtain a continuum of intensities along each lattice rod, the data for each rod must be curve fit.

In the PhoE data base, to a resolution of about 2.8 A, there are greater than 2100 lattice rods. Examples of fitted lattice rod intensity curves are given in Figure 28. Along the fitted curves, measured data points are depicted with an "X". Each such point represents the average of a Friedel pair. The error bars about each data point represent the intensity differences between the Friedel symmetry related spots. Thus, the two extreme ends of the error bars actually represent the measured intensity values of each member of a Friedel pair.

Having created the lattice rod intensity curves allows one to assess how well the diffraction patterns merge. This assessment is aided by the use of the Rmerge factor. This factor is determined by a comparison of measured diffraction spot intensities with those interpolated from corresponding spatial locations along the fitted intensity curves. Equation 4 defines the Rmerge factor as:

$$R_{merge} = \frac{\sum_{H,K} \left| I_{OBS_{H,K}} - I_{curve_{H,K}} \right|}{\sum_{H,K} I_{curve_{H,K}}}$$

equation 4

Figure 28. Examples of merged diffraction intensities and their fitted curves for four lattice lines. The x's represent averaged Friedel related intensities while the vertical lines associated with these points represent the intensity differences between the respective members of the Friedel pair.

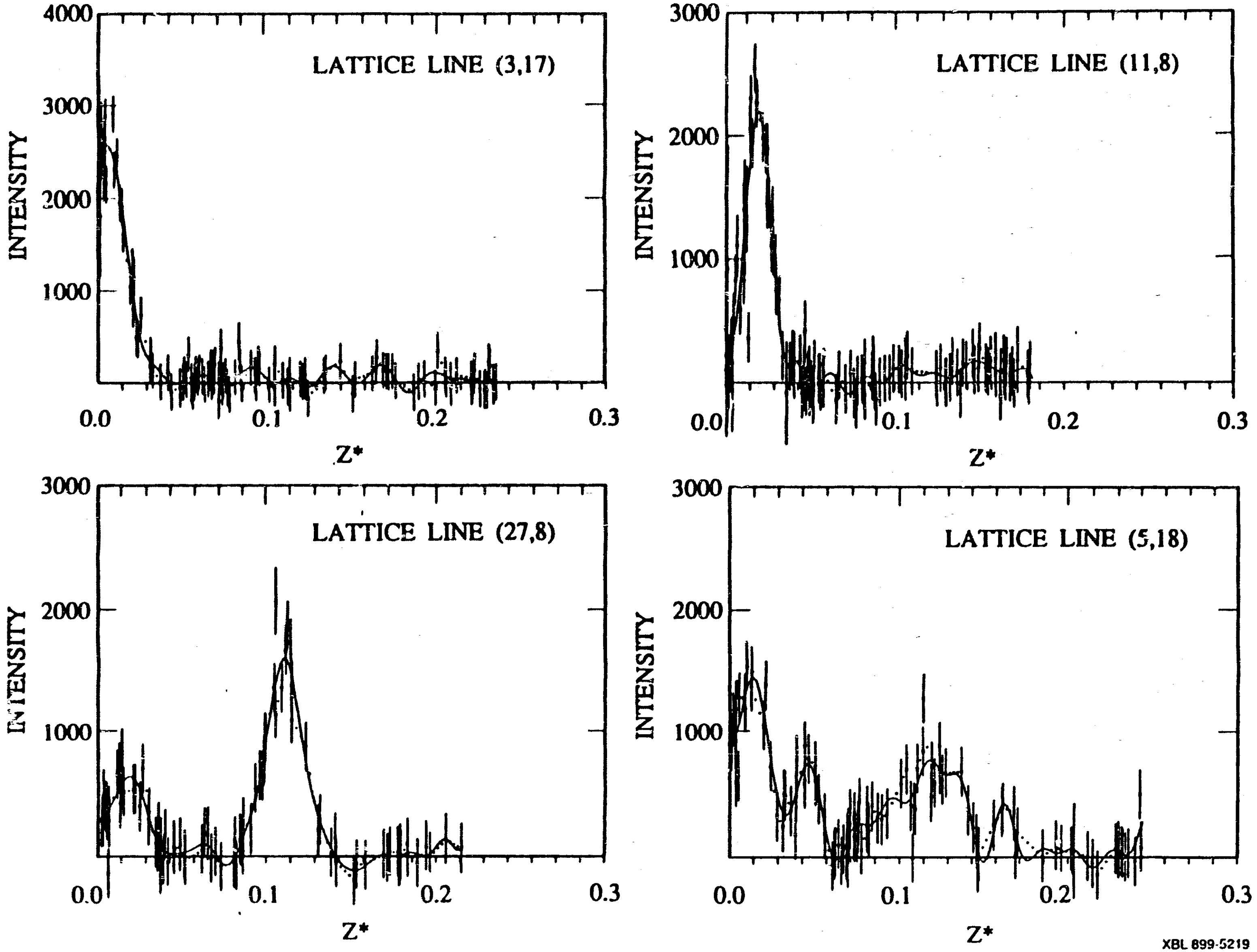
LATTICE LINE (3,17)
LATTICE LINE (11,8)
LATTICE LINE (27,8)
LATTICE LINE (5,18)
INTENSITY
4000
3000
2000
1000
0.0
0.1
0.2
0.3
Z*

XBL 899-5219

Iobs represents the average intensity of a Friedel pair while Icurve represents the corresponding curve estimated intensities. The summations are over all diffraction spots available. Considering all reflections in the 3-D data set a global Rmerge value of 0.39 was obtained. As is the case with calculations of Rsym factors, patterns with large numbers of very low intensities can yield relatively high Rmerge factors. Since only 10 percent of the intensities in the data base are greater than one background standard deviation above the mean background one would expect larger than nominal Rmerge factors. If one considers only those reflections with intensities greater than this lower limit an Rmerge value of 0.27 is obtained.

As a check to see how thoroughly reciprocal space has been sampled, one typically plots the lengths of the lattice rods constituting the intensity data collected. We have plotted the 3-D lattice rod data in a 2-D format by rotationally projecting the intensity data about z*. In the resulting graph the horizontal axis defines resolution within the a*,b* plane while the vertical axis continues to represent z*. In an effort to keep the plot simple we have chosen to plot only the maximum resolution sampled along each lattice rod. When merging the various diffraction patterns to generate the 3-D data set, a global resolution limit of 2.5 A was imposed. Due to the diffraction spot rejection criteria and radial range limits applied during individual diffraction pattern processing, a majority of intensity lattice rods in the data set will have points of maximum resolution significantly below the global resolution limit. Figure 29 shows such a plot where the sampling limits are depicted as dots.

Figure 29. Sampling of reciprocal space. This graph is a two-dimensional representation of the three-dimensional data set. It was generated by compressing data about the z* axis so that the horizontal axis represents resolution along the a*, b* plane. Each dot represents the maximum resolution sampled along a particular lattice line.

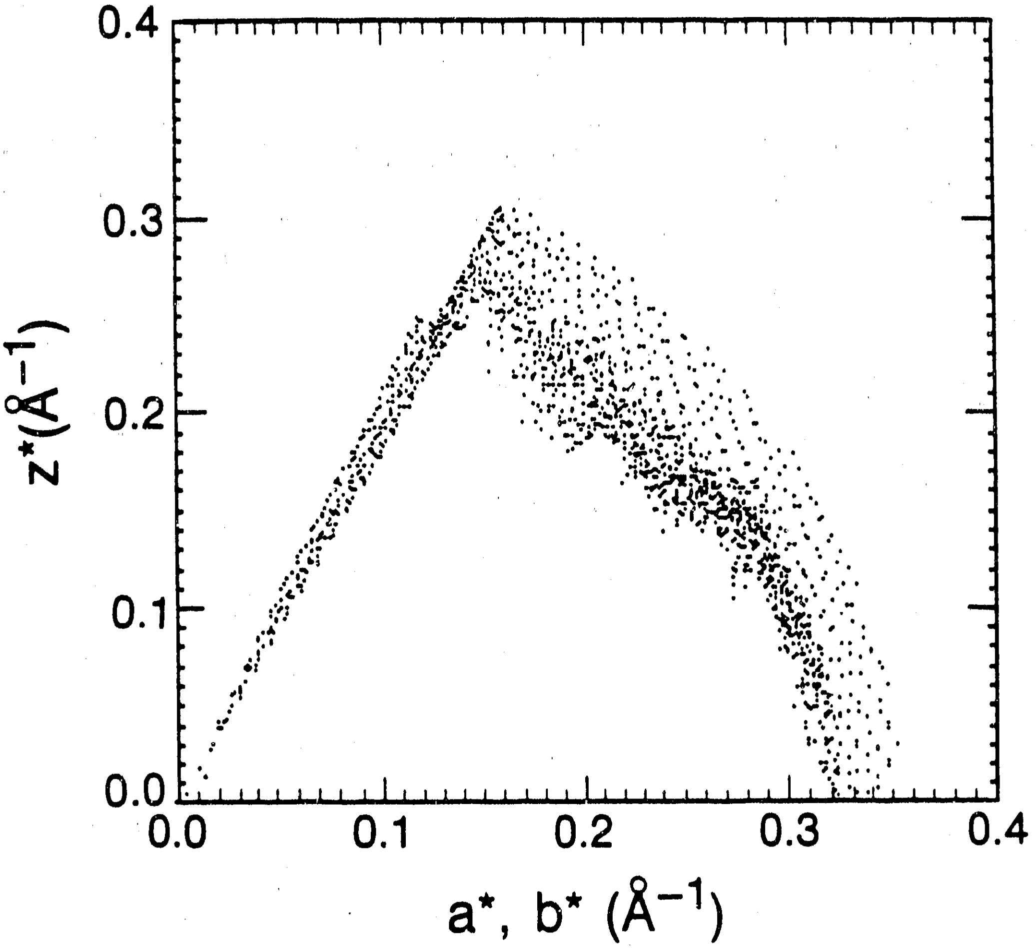

XBL 899-5215

3.5 Distribution of Intensity in the 3-D Data Set

Diffraction patterns of specimens tilted at 45 and 60 degrees display zones of intense off-axis reflections centered at about 4.8 A resolution. These strong intensity zones occur in the same respective region of each 45 and 60 degree tilted pattern regardless of the orientation of the crystal with respect to the specimen tilt axis. The 3-D intensity data set shows that the strong intensities in these off-axis zones are distributed as a figure of revolution about the z* axis. This toroidal distribution of intense reflections indicates a general cylindrical symmetry in the porin's structure.

The 3-D diffraction intensity set contains several interesting distibutions of bright reflections. Figure 30 is a contour plot of these intensities which have been compressed into a 2-D format in the same fashion described earlier for the reciprocal space sampling plot. The strongest reflections are clustered into limited domains of reciprocal space. Of particular note are the clusters of intense reflections occuring at low values of z* which are centered at resolutions of about 67A, 13A, 10A and 4.4A and the arc-like "finger" of strong intensities extending up from the a*,b* plane centered at about 4.8A resolution.

Figure 30. Contour plot of intensities in the diffraction data set. This graph is a two-dimensional representation of the three-dimensional data set. It was generated by projecting data about the z* axis so that the horizontal axis represents resolution along the a*, b* plane. To generate smooth contour plots of the intensity distribution within the data set, the original array of data was superpixelized into a 40x40 pixel matrix prior to contouring. Shown in this figure are five contour levels, with the first (lowest) level representing the minimum intensity value. Level two indicates the location of intensities greater than or equal to one and one-half times the standard deviation of the intensities in the superpixelized data set. Levels three and higher are incremented in steps of one intensity standard deviation.

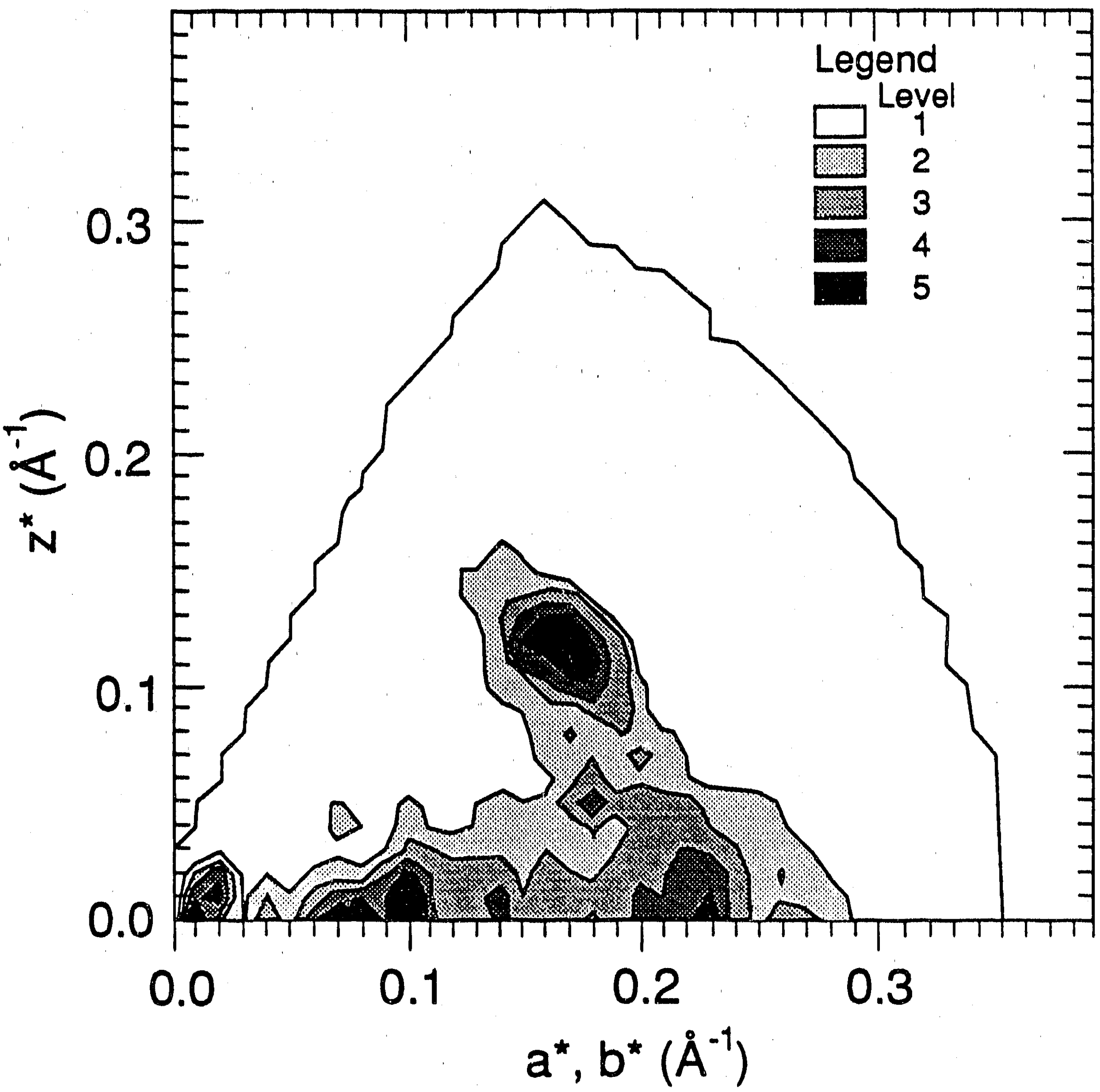

XBL 899-5216

Combining the observation that the dominant high resolution feature in the merged intensity data is the "arc" of bright reflections centered at about 4.8 A resolution with the finding that these reflections are toroidally distributed about z* suggests the existence of cylindrically shaped beta-sheet in the structure of PhoE porin.

SECTION IV

DISCUSSION

4.1 Porin Pore Diameter Estimates

We assessed the prediction of porin pore diameters from the results of black lipid membrane (BLM) and porin liposome experiments. It was found that by applying appropriate values for the single channel conductance and channel length, in the equation used to estimate pore radii from BLM conductance data, values significantly different from those predicted from the various liposome experiment data would be obtained (see Table 1 and 2). The BLM conductance based estimates derived in this manner are lower than the minimum diameter of solutes known to be able to pass through the porin channels (H.Nikaido, personal communication). Pore diameter estimates determined from permeability rate studies of OmpF, OmpC and PhoE fall into a range of 10 - 12 A. Current data pertaining to porin exclusion limits appear to be better suited for indicating an upper and lower bound for estimates of pore diameter rather than one specific value. Potential sources of error in the estimation of pore diameters from BLM and permeabilty rate data include deviations in the porin structure from that of the cylindical geometry imposed in the respective models, in the use of estimated pore lengths and in the assumption that properties of the bulk medium such as conductance reflect conditions existing in the porin pore's interior accurately enough.

4.2 Porin Channel Voltage Gating

We also reviewed the literature for results addressing the existence of voltage dependent closings of the individual channels of porin trimers. From the evidence we encountered we became convinced that the channel conductances of the porins, as measured with the BLM technique, can indeed be voltage modulated. In our opinion, the failure of some researchers to observe channel closings in their BLM configurations on a regular basis is due to various differences in experimental protocol and technique. Areas of experimental difference included when and where the porins were added, how the transmembrane potentials were applied and the time interval of data recordings. Although we wholeheartedly acknowledge the observation of voltage dependent closings of the major E.coli porins and PhoE in numerous in vitro systems, we remain to be convinced that similar types of channel closings occur in intact cells under physiological conditions.

4.3 Electron Crystallography of PhoE Porin

Preliminary analysis revealed that our 2-D crystals of PhoE porin were extremely well ordered. To ensure that we could obtain sufficient numbers of high quality electron diffraction patterns from these crystals, we embarked on a series of experiments in an effort to establish a protocol which would allow us to create flat, well- preserved specimens on a reliable basis. Achieving this capability would not only allow us to obtain high-resolution electron diffraction data but dramatically increase our chances for success in collecting images able to yield high-resolution phase information even at high specimen tilt angles. After surveying a variety of embedment conditions we settled upon a protocol which used trehalose as the embedment sugar. Specimens embedded in trehalose on top of hydrophilic carbon coated grids yielded crystals which were extremely flat and well ordered. This was evidenced by our ability to collect electron diffraction patterns having isotropically sharp spots, even from specimens tilted up to 60 degrees.

Processed electron diffraction patterns were found to yield structural information beyond 3 A resolution and were merged into a 3-D intensity data set. Analysis of the global distribution of reflections in this data set revealed a unique toroidal distribution of intense reflections centered about the z* axis at a resolution of about 4.8 A. Since the average inter-strand spacing of beta-sheet is about 4.8A (Richardson and Richardson, 1985), this observation provides strong evidence that a cylindrically shaped structure, made up of beta-sheet represents a major portion of the polypeptide chain of PhoE porin.

This interpretation of the diffraction data is in agreement with the general conclusions of earlier biophysical studies. Spectroscopic studies have established that the E. coli porins are predominantly anti-parallel beta-sheet with little or no detectable alpha-helix (Rosenbusch 1974; Nakamura and Mizushima 1976; Nakamura et.al. 1974; Vogel and Jaehnig 1986). The results of previous electron crystallography studies of PhoE porin in both negative stain and glucose embedment (Jap 1989) suggest that much of the porin's protein is beta-sheet, arranged to form a cylindrical structure. X-ray diffraction investigations of OmpF porin, a porin highly homologous to PhoE, yielded evidence for the existence of a significant segment of beta-sheet with strands oriented predominantly perpendicular to the membrane plane (Kleffel et.al. 1985).

In figure 30 it can be seen that there are a number of general features discernable in our data which are also apparent in the X-ray diffraction data of Kleffel et. al., including the "arc" of intense reflections located between 5.0 and 4.5 A. Unfortunately the paper of Kleffel et.

al. only contains one azimuthal view of the distribution of diffraction intensities. This is not sufficient to assess whether this diffraction data set contains a toroidal distribution of intense high resolution reflections similar to that seen in the PhoE data.

Although there is a continuum of relatively strong intensities along the high resolution "arc" in the PhoE merged data set, the strongest intensities are clustered into a few regions. Figures 31 through 33 are graphs of intensities present along reciprocal space "arcs" of varying widths which are centered between 4.75 and 4.8 A resolution. The horizontal axes of these graphs describes the angle of inclination up from the a*,b* plane. From the perspective of a protein oriented in a lipid bilayer, these angles can be considered to represent the angle formed between the observer's line-of-sight to the protein and a line normal to the membrane plane. What one readily notices in these figures is that the strongest intensities are clustered bimodally about inclination angles of 0 and 35 degrees. Additionally, it is apparent that the relative heights and widths of these clustering peaks are quite sensitive to the widths of the arc zones evaluated. Of the two major clusters at 0 and 35 degrees, the brightest reflections are associated with an average inclination angle of 35 degrees. Additional clusterings of substantially lower intensities are distributed

Figure 31. Distribution of intensities along a radial resolution arc of 4.8 A. The width of each intensity integrating bin is one degree. Reflections at a resolution within 0.001 1./A of 0.208 1./A were chosen. This case was arranged so as to show the distribution of intensities in a narrow region about 4.8 A, the average interstrand spacing in beta-sheet.

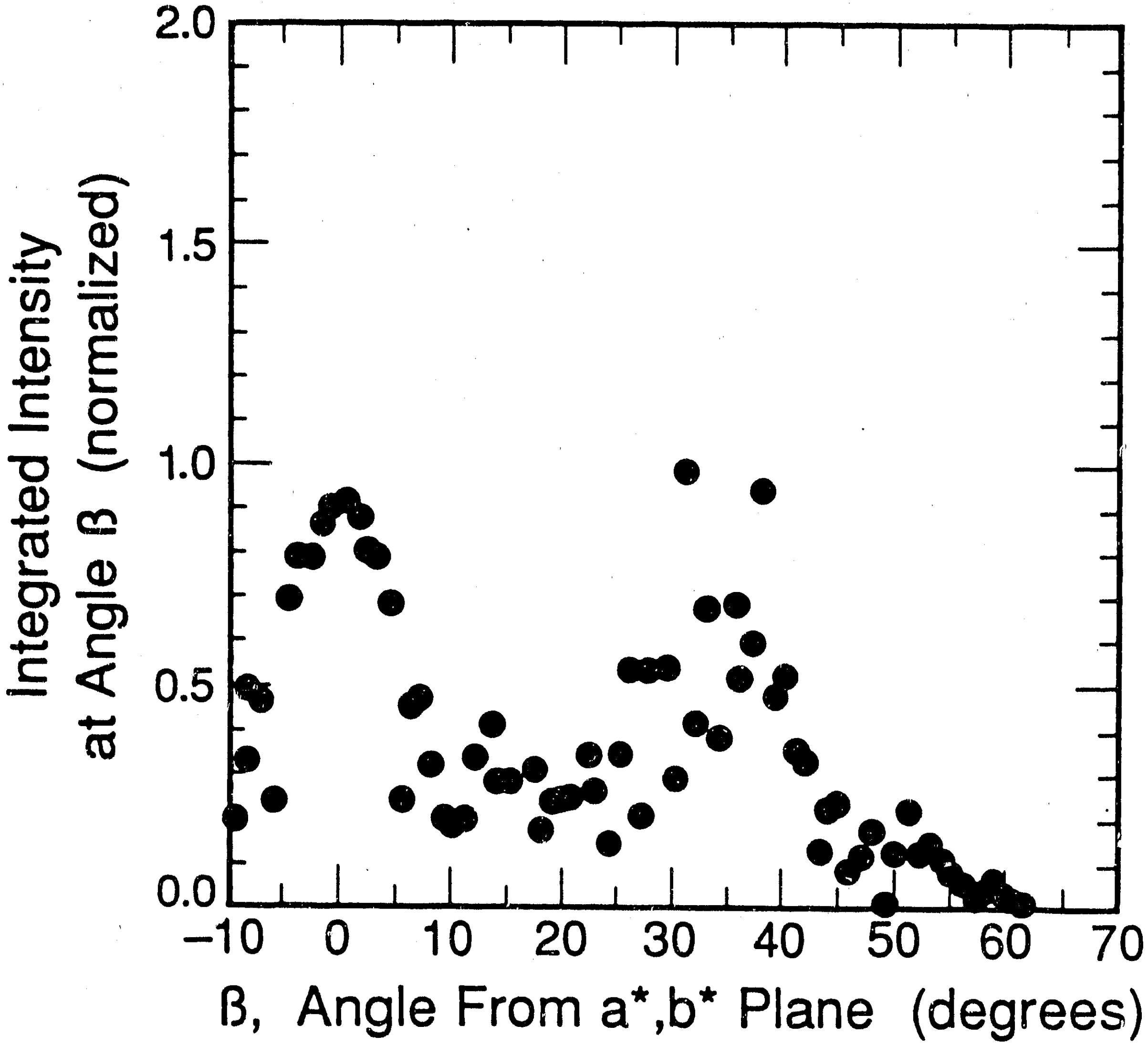
2.0
1.5
1.0
0.5
0.0
Integrated Intensity
at Angle ß (normalized)
−10
0
10
20
30
40
50
60
70
ß, Angle From a*,b* Plane (degrees)

XBL 899-5244

Figure 32. Distribution of intensities along a radial resolution arc of 4.78 A. The width of each intensity integrating bin is one degree. Reflections at a resolution within 0.0025 1./A of 0.2095 1./A were chosen. This case was arranged so as to show the distribution of intensities in a zone centered at the location of peak intensities occuring within a 5.0 to 4.5 A resolution window at an inclination angle of 0 degrees from the a*,b* plane. The width of the zone is equivalent to the standard deviation of the intensities about the peak at 0 degrees inclination.

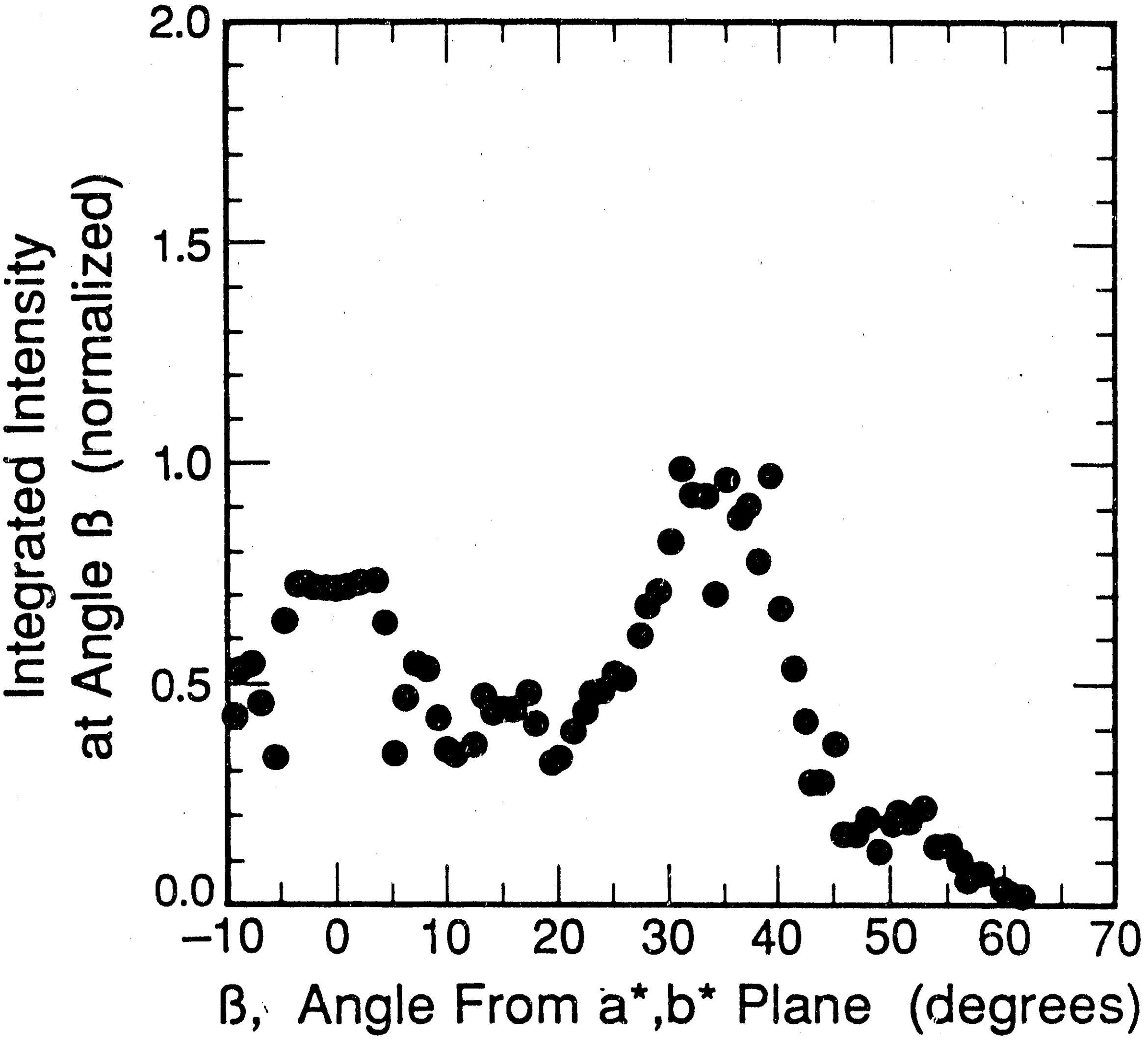
Integrated Intensity
at Angle ß (normalized)
2.0
1.5
1.0
0.5
0.0
−10
0
10
20
30
40
50
60
70
ß, Angle From a*,b* Plane (degrees)

XBL 899-5243

Figure 33. Distribution of intensities along a radial resolution arc of 4.75 A. The width of each intensity integrating bin is one degree. Reflections at a resolution within 0.01 1./A of 0.21 1./A were chosen. This case was arranged so as to show the distribution of intensities in a zone centered at the location of peak intensities occuring within a 5.0 to 4.5 A resolution window at an inclination angle of 35 degrees from the a*,b* plane. The width of the zone is equivalent to the standard deviation of the intensities about the peak at 35 degrees inclination.

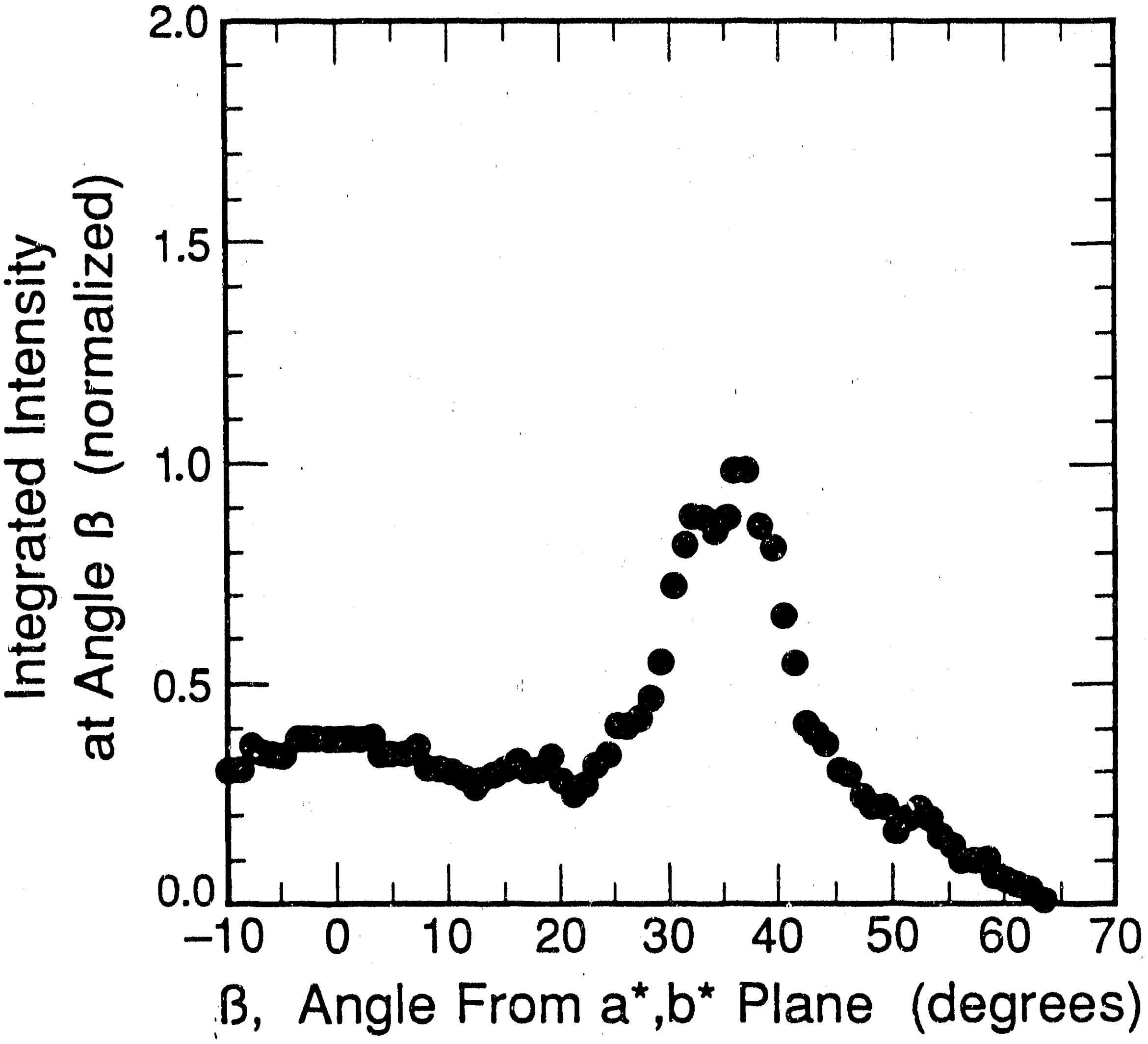
Integrated Intensity
at Angle β (normalized)
2.0
1.5
1.0
0.5
0.0
−10
0
10
20
30
40
50
60
70
β, Angle From a*,b* Plane (degrees)

XBL 899-5242

throughout the length of these "arcs". The interesting distribution of intense reflections seen in this data indicates that although some of the protein's beta-sheet strands are distributed over the range of tilt angles from 0 to 60 degrees, relatively large portions of the protein's beta-sheet are made up of strands tilted close to 0 or 35 degrees away from a line normal to the membrane plane.

To obtain a length estimate of PhoE porin structure extending perpendicularly through the membrane, an analysis of the lattice rod intensities was conducted using methods described by Henderson (1975). In such a treatment, one considers the modulation of low resolution intensites along a given lattice rod to be due in large part to the thickness of the protein within the membrane. This intensity modulation has the form of a sinc function and is modeled as the Fourier transform of the step-like extent of the membrane. One then can get an estimate of the protein thickness from the width of the first maxima at half-maximum intensity. From our analysis we determined a value for the mean structure length of 37 A having a standard deviation of 12 A. These values are based on data from 74 lattice rods.

Based on the results of an FTIR spectroscopic analysis of OmpF porin two general secondary structure models for that porin were proposed and assessed (Nabedryk et. al. 1988). One model required that all the porin's beta-sheet strands have an average tilt of about 45 degrees away from the membrane plane while a second model contained two major domains of beta-sheet, one in which the strands were parallel and another with strands perpendicular to the membrane plane. Since previous X-ray diffraction studies (Kleffel et.al. 1985) had been interpreted as indicating a significant presence of untilted beta-sheet strands, Nabedryk et. al. endorsed the latter model. We have not found evidence for the existence of a large population of beta-sheet strands with an average tilt of 45 degrees in the PhoE 3-D data set. While we have found evidence indicating a significant population of untilted beta-sheet strands in the structure of PhoE, we have not seen strong intensities at a resolution of 3.5 A in the a*,b* plane which would be predictive of a similarly sized domain of beta-sheet strands parallel to the membrane plane.

Recently, the projection map of untilted PhoE porin has been determined to 3.5 A resolution (Jap et al. 1990). In this map, the highest density feature is a "beaded" ring-like structure which demarks the perimeter of each monomer in a PhoE trimer. The average spacing between the "beads" of each monomer associated "ring" is between 5.0 and 4.5 A. The dimensions and distribution of these high density features is compatable with the idea that this projection map represents an end-on view of cylindrically arranged segments of beta-sheet in which a significant fraction of the full length of the beta-sheet strands are oriented essentially perpendicular to the membrane plane.

In summary we have presented evidence for the existence of major populations of beta-sheet strands with average tilt angles of 0 and 35 degrees. In addition to these primary beta-sheet strand populations there also appears to be lesser amounts of beta-sheet strands with orientations covering the range of tilt angles from 0 to 60 degrees. Finally, these beta-sheet strands are predicted to be arranged into a generally cylindrical structure.

Incorporating this interesting mix of beta-sheet strands into a stereochemically acceptable structure would appear to require a complex arrangement of the protein elements described. If the general structural motif of a PhoE porin monomer is a right cylinder, certain organizational constraints must be reckoned with. Such cylinders would have to be able to generate the unique spatial distribution of strong intensities in the data set, for example those seen at inclination angles of 0 and 35 degrees.

One interpretation would be that this unique intensity distribution is the result of a tilted arrangement of right beta-sheet cylinders comprised of a homogeneous population of beta-sheet strands with a tilt angle relative to the monomer axis that is not equal to 35 or 0 degrees. The effective tilt of the beta-sheet strands on each monomer within a trimer would be the combined result of monomer tilt with respect to the three-fold trimer axis, tilt of the trimer three-fold axis with respect to the membrane plane, and tilt of the beta-sheet strands with respect to the monomer axis. The likelihood that such a scheme is actually reflected in the PhoE structure seems low since the monomer tilt angles, as implied by the negative stain data, appear to be too small to introduce the variety of orientation needed to generate the bimodal intensity distribution from strands of a single tilt angle. Although a monomer pore tilt angle of about 20 degrees was determined from the negative stain data (Jap 1989), the general shape of the stain filled regions implies that the protein cylinder itself is tilted very little. Proper assessment of the feasability of this general model will require modeling analysis beyond the scope of this thesis.

The other alternative is that the monomer structure itself is made up of beta-sheet strands with tilt angles close to 35 and 0 degrees. The stereochemical design by which such a structure could be realized cannot be deduced in advance, and one must simply wait until a high resolution 3-D density map is available before trying to build a molecular model that can account for the observed distribution of diffraction intensities.

Although we cannot solve the structure with the information currently in hand, we can assess the design constraints imposed by structural parameters such as cylinder size and the predominant beta-sheet strand tilt angles. From projection maps of untilted PhoE embedded in glucose the circumference at the monomer's widest point has been estimated to be about 100 Å (Jap 1989). A monomer with a circumference of this size could contain a beta-sheet cylinder composed of 21 untilted strands, or 17 strands with a tilt of 35 degrees with respect to the monomer's axis. One organizational scheme feasable under the above conditions is that a monomer consists predominantly of a stacked arrangement of cylindrical segments/rings, each segment homogeneously composed of beta-sheet strands tilted either 35 or 0 degrees. Based on surveys of soluble protein structure (Richardson, 1981) a relatively large change in beta-sheet strand tilt angle can be brought about through a combination of appropriately placed beta-bulges and turns. Therefore, between cylindrical domains of 35 and 0 degree tilted beta-strands one would also expect to find intervening strand orientation transition zones. If the number of strands making up the monomer under such an arrangement is held constant along the monomer's length, the diameter of the cylinder can not be maintained over its length. This combination of structural elements would result in a monomer having a stepped funnel-like apperance.

A variant of the previous structural scheme is the case of a constant diameter monomer. If a monomer cylinder of constant diameter was to be made from stacked homogeneous segments of 35 and 0 degree tilted beta-sheet strands, then strands would have to be removed or added as one traversed the length of the monomer. As with the variable diameter cylinder scheme, changes in strand tilt from 0 to 35 degrees could be brought about through a combination of beta-bulges and turns.

An additional point to consider is whether a monomer with constant cylindrical dimensions, such as those noted in the projection map of PhoE, could form an effective pore diameter of the size expected from BLM, diffusion rate and exclusion limit experiments, about 10 A. Satisfying both dimensional constraints with this cylinder seems highly improbable, for even if the cylinder interior were thoroughly lined with the longest amino acids available (eg lysines) fully extended from the beta-sheet backbone, they would not be able to form a channel-like occlusion with a diameter as small as 10 A. One answer to this apparent problem would be the addition of other channel-forming segments of beta-sheet having a diameter significantly smaller than the maximum cylinder diameter seen in the projection map. In the PhoE projection map relatively high densities, comparable to those forming the "beaded rings" described earlier, are seen within the confines of the apparant beta-sheet cylinder, indicating that additional channel-forming structures of narrower dimensions may indeed be part of the monomer's structure.

The models considered above have made use of "stacked" arrangements of cylindrical regions of beta-sheet composed of homogeneously tilted strands. It is also possible that the porin structure's beta-sheet contains a mixture of strand tilt angles distributed about the monomer's cylindrical axis. Such an arrangement might be the end result of beta-sheet strand extraction and could leave gaps or other imperfections in the "lattice work" of the beta-sheet in regions where strand/strand hydrogen bonding could not occur. Concern about the functionality of a structurally imperfect cylinder would be lessened if this cylinder were enclosing a second smaller cylinder, possibly made from the same extracted strands that caused the outer cylinder imperfections.

Whatever the actual protein envelope it is evident that a beta-sheet structure architecture more complex than that described for a typical beta-barrel (Richardson 1981, Salemme 1981, Salemme and Weatherford 1981) is involved in the structure of PhoE porin. How such a task has actually been accomplished will have to await the determination of the high resolution structure to three dimensions.

4.4 Future Prospects

We have obtained a complete 3-D intensity data set of PhoE porin extending out to a resolution of 3.5 A. Data out to this resolution has been shown to be reliable according to the accepted criteria for evaluating electron diffraction data, Rsym and Rmerge. Although this represents a significant stride, the intensity data set remains only one half of the data needed to solve the atomic structure of PhoE porin. We are currently in the process of collecting images to obtain high resolution phase information which will become the remaining half of the data needed. As high-resolution images are obtained, the intensity data set will aid in the determination of contrast transfer functions and in the evaluation of image quality.

A team of researchers have made significant progress towards solving the structure of Rhodopseudomonas capsulata (R. capsulata) porin to atomic resolution via X-ray crystallography (Nestel et al. 1989). They have reported obtaining crystals of the native protein which diffract beyond 3.5 A. Functional porin is isolated from the bacteria in monomeric form. This is in contrast to the major porins of E. coli, as well as for PhoE, which are all isolated in a functional trimeric form and for which monomers can only be obtained under denaturing conditions.

Circular dichroism spectroscopy of the porin from R. sphaeroides has shown, just as for the porins of E. coli, that the protein is predominantly in a beta-sheet conformation with little or no discernable level of alpha helix (Weckesser et al. 1984).

The versatility of these proteins in serving as regulators of solute diffusion, as well as their resistance to denaturation over a range of extreme conditions is widely recognized. As the structures of the porins from E. coli and R. capsulata are determined it will be of great interest to know what common and possibly unique structural motifs exist between them. The architectures revealed in these "simple" transmembrane channels will provide models for understanding the mechanisms involved in membrane transport and may even serve as the blueprints for the design of novel proteins.

The results of this research and the preliminary findings of PhoE imaging studies (B.K. Jap ,unpublished results) indicate that obtaining high-resolution phase information from tilted specimens is a realistic expectation. More significantly, they indicate that solving the structure of PhoE porin to atomic resolution by electron crystallography is an achievement we can expect to accomplish in the not too distant future.

Bibliography

Allen,J.P., Feher,G., Yeates,T., Komiya,H. and Rees,D.C. 1987a Proc. Natl. Acad. Sci. USA 84:5730-5734

Allen,J.P., Feher,G., Yeates,T., Komiya,H. and Rees,D.C. 1987b Proc. Natl. Acad. Sci. USA 84:6162-6166

Baldwin,J. and Henderson,R. 1984 Ultramicroscopy 14:319-336

Baldwin,J., Henderson,R., Beckman,E. and Zemlin,F. 1988 J. Mol. Biol. 202:585-591

Benz,R. 1985 CRC Critical Reviews in Biochemistry, Vol.19, Issue 2, pp145-190

Benz,R., Janko,K., Boos,W. and Lauger,P. 1978 Biochem. Biophys. Acta 511:305

Benz,R., Schmid,A. and Hancock,R.E.W. 1985 J. Bacteriol. 162:722-727

Benz,R., Tokunaga,H. and Nakae,T. 1984 Biochem. Biophys. Acta 769:348-356

Braun,V., Rotering,H., Ohms,J.-P. and Hagenmeier,H.

1976 Eur. J. Biochem. 70:601-610

Cantor,C. and Schimmel,P. 1980 Biophysical Chemistry; Part 2, pp715-719 W.H. Freeman and Co. (San Francisco)

Chang,C., Mizushima,S. and Glaeser,R.M. 1985 Biophys. J. 47:629-639

Chen,R., Schmidmayr,W., Kramer,C., Chen-Schmeisser,U. and Henning,U. 1980 Proc. Natl. Acad. Sci. 77:4592-4596

Chou,P. and Fasman,G.D. 1978 Adv. Enzymol. 45:45-148

Cohen,F.S., Akabas,M.H. and Finkelstein,A. 1982 Science 217:458

Dargent,B., Hofmann,W., Pattus,F. and Rosenbusch,J.P. 1986 EMBO J. 5:773-778

Darveau,D.P., Hancock,R.E.W. and Benz,R. 1984 Biochem. Biophys. Acta 774:67-74

Datta,D.B., Arden,B. and Henning,U. 1977 J. Bacteriol. 131:821-829

Decad,G.M. and Nikaido,H. 1976 J. Bacteriol. 128:325-336

Deisenhofer,J., Epp,O., Miki,K., Huber,R. and Michel,H. 1984 J. Mol. Biol. 180:385-398

Deisenhofer,J., Epp,O., Miki,K., Huber,R. and Michel,H. 1985 Nature 318:618-624

Dorset,D.L., Engel,A., Haner,M., Massalski,A. and Rosenbusch,J.P. 1983 J. Mol. Biol. 165:701-710

Dorset,D.L., Engel,A., Massalski,A. and Rosenbusch,J.P. 1984 Biophys. J. 45:128-129

Engel,A., Massalski,A., Schindler,H., Dorset,D.L. and Rosenbusch,J.P. 1985 Nature 317:643-645

Garavito,R.M., Jenkins,J., Jansonius,J.N., Karlsson,R. and Rosenbusch,J.P. 1983 J. Mol. Biol. 164:313-327

Garavito,R.M., Jenkins,J.A., Neuhaus,J.M., Pugsley,A.P. and Rosenbusch,J.P. 1982 Ann. Microbiol. 133a:37-41

Gehring,K. and Nikaido,H. 1989 J. Biol. Chem. 264:2810-2815

Glaeser,R.M., Tong,L. and Kim,S.-H. 1988 Ultramicroscopy 27:307-318

Hancock,R.E.W. 1987 J. Bacteriol. 169:929-933

Hancock,R.E.W. and Benz,R. 1986 Biochem. Biophys. Acta 860:699-707

Hancock,R.E.W., Schmidt,A., Bauer,K. and Benz,R. 1986 Biochem. Biophys. Acta 860:263-267

Hayward,S. and Glaeser,R. 1980 Ultramicroscopy 5:3-8

Hazelbauer,G.L. 1975 J. Bacteriol. 124:119-126

Henderson,R. 1975 J. Mol. Biol. 93:123-138

Henderson,R., Baldwin,J.M., Downing,K.H., Lepault,J. and Zemlin,F. 1986 Ultramicroscopy 19:147-178

Henderson,R. and Unwin,P.N.T. 1975 Nature 257:28-32

Hille,B. 1984 In "Ionic Channels of Excitable Membranes" pp 185-186, Massachusetts: Sinauer Associates Inc.

Inokuchi,M., Mutoh,N., Matsuyama,S. and Mizushima,S. 1982 Nuc. Acids Res. 10:6957-6968

Inouye,M., Show,J. and Shen,C. 1972 J. Biol. Chem. 247:8154-8159

Jap,B.K. 1986 Proc. EMSA 44th Ann. Mtg., Bailey,G.W.,ed. pp164-165

Jap,B.K. 1988 J. Mol. Biol. 199:229-231

Jap,B.K. 1989 J. Mol. Biol. 205:407-419

Jap,B.K., Downing,K.H. and Walian,P.J. 1990 J. Struct. Biol., in press

Kleffel,B., Garavito,R.M., Baumeister,W. and Rosenbusch,J.P. 1985 EMBO J. 4:1589-1592

Korteland,J., Overbeeke,N., DeGraff,P., Overduin,P. and Lugtenberg,B. 1985 Eur. J. Biochem. 152:691-697

Kuhlbrandt,W. and Downing,K.H. 1989 J. Mol. Biol. 207:823-828

Kyte,J. and Doolittle,R.F. 1982 J. Mol. Biol. 157:105-132

Leifer,D and Henderson,R. 1983 J. Mol. Biol. 163:451-466

Luckey,M. and Nikaido,H. 1980 Proc. Natl. Acad. Sci. USA 77:167-171

Manning,P.A. and Achtman,M. 1979 Bacterial Outermembranes M.Inouye ed., John Wiley and Sons, Inc. (New York) p407-447

Manning,P.A., Pugsley,A.P. and Reeves,P. 1977 J. Mol. Biol. 116:285-300

Mauro,A., Blake,M. and Labarca,P. 1988 Proc. Natl. Acad. Sci. USA 85:1071-1075

Mizuno,T., Chou,M.-Y. and Inouye,M. 1983 J. Biol. Chem. 258:6932-6940

Nabedryk,E., Garavito,R.M. and Breton,J. 1988 Biophys. J. 53:671-676

Nakae,T. 1976a Biophys. Res. Commun. 71:877-884

Nakae,T. 1976b J. Biol. Chem. 251:2176-2178

Nakamura,K. and Mizushima,S. 1976 J. Biochem. 80:1411-1422

Nakamura,K., Ostrovsky,D.N., Miyazawa,T. and Mizushima,S. 1974 Biochem. Biophys. Acta 332:329-335

Nestel,U., Wacker,T., Woitzik,D., Weckesser,J., Kreutz,W. and Welte,W. 1989 FEBS letters 242:405-408

Nikaido,H. and Rosenberg,E.Y. 1981 J. Gen. Physiol. 77:121-135

Nikaido,H. and Rosenberg,E.Y. 1983 J. Bacteriol. 153:241-252

Nikaido,H., Rosenberg,E.Y. and Foulds,J. 1983 J. Bacteriol. 153:232-240

Nikaido,H., Song,S.A., Shaltiel,L. and Nurminen,M. 1977 Biochem. Biophys. Res. Commun. 76:324-330

Nikaido,H. and Vaara,M. 1985 Microbiol Review 49:1-32

Overbeeke,N., Bergmans,H., van Mansfeld,F. and Lugtenberg,B. 1983 J. Mol. Biol. 163:513-532

Palva,E.T. 1979 Eur. J. Biochem. 93:495-503

Renkin,E. 1954 J. Gen. Physiol. 38:225-253

Richardson,J.S. 1981 Adv. Prot. Chem. vol 34, pp190-223

Richardson,J.S. and Richardson,D.C. 1985 Methods Enzymol. 115:189-206

Rosenbusch,J.P. 1974 J. Biol. Chem. 249:8019-8029

Salemme,F.R. 1981 J. Mol. Biol. 146:143-146

Salemme,F.R. and Weatherford,D.W. 1981 146:119-141

Sass,H.J., Buldt,G., Beckmann,E., Zemlin,F., van Heel,M., Zeitler,E., Rosenbusch,J.P., Dorset,D.L. and Massalski,A. 1989 J. Mol. Biol. 209:171-175

Sawai,T., Matusba,K. and Yamagashi,S. 1977 J. Antibiot. 30:1134-1136

Schindler,H. and Rosenbusch,J.P. 1978 Proc. Natl. Acad. Sci. USA 75:3751

Schindler,H. and Rosenbusch,J.P. 1981 Proc. Natl. Acad. Sci. USA 78:2302-2306

Sen,K., Hellman,J. and Nikaido,H. 1988 J. Biol. Chem. 263:1182-1187

Shaw,P. and Hills,G. 1981 Micron 12:279-282

Steven,A.C., ten Heggler,B., Muller,R., Kistler,J. and Rosenbusch,J.P. 1977 J. Cell Biol. 72:292-301

Szmelcman,S. and Hofnung,M. 1975 J. Bacteriol. 124:112-118

Tommassen,J. 1988 in Membrane Biogenesis, NATO ASI Ser. Vol. H16, ed. Op den Kamp,J.A.F., pp351-373, Springer-Verlag (New York)

Tommassen,J., Van der Ley,P., Van Zeijl,M. and Agterberg,M. 1985 EMBO J. 4:1583-1587

Tsygannik,I.N. and Baldwin,J.M. 1987 Eur. Biophys. J. 14:263-272

Ueki,T., Mitsui,T. and Nikaido,H. 1970 J. Biochem. (Tokyo) 85:173-182

Unwin,P.N.T. and Henderson,R. 1975 J. Mol. Biol. 94:425-440

Van der Ley,P., Amesz,H., Tommassen,J. and Lugtenberg,B. 1985 Eur. J. Biochem. 147:401-407

Van der Ley,P., Buim,P., Agterberg,M., Van Meersbergen,J. and Tommassen,J. 1987 Mol. Gen. Genet. 209:585-591

Van der Ley,P., Struyve,M. and Tommassen,J. 1986 J. Biol. Chem. 261:12222-12225

Vogel,H. and Jahnig,F. 1986 J. Mol. Biol. 190:191-199

Weckesser,J., Zalman,L.S. and Nikaido,H. 1984 J. Bacteriol. 159:199-205

Xu,G., Shi,B., McGroarty,E.J. and Tien,H.T. 1986 Biochem. Biophys. Acta 862:57-64

Yoshimura,F., Zalman,L. and Nikaido,H. 1983 J. Biol. Chem. 258:2308-2314

Zimmerman,W. and Rosselet,A. 1977 Antimicrob. Agents Chemother. 30:1134-1136

END

DATE FILMED

01 / 03 / 91